Theoretical study of the Kondo effect in the quantum dots

Pavel Vitushinsky

THÈSE

présentée par

Pavel Vitushinsky

pour obtenir le grade de

Docteur de
l'Université Joseph Fourier - Grenoble 1
Spécialité : Physique

Etude théorique de l'effet Kondo dans les boîtes quantiques

Soutenue le 3 Novembre 2005 devant la Commission d'Examen :

M.	Gilles Montambaux	Rapporteur
M.	Peter Wölfle	Rapporteur
M.	Frank Hekking	Examinateur
M.	Philippe Nozières	Président
Mme.	Mireille Lavagna	Directrice de thèse
M.	Andrés Jerez	Codirecteur de thèse

Mémoire Préparé au sein du Service de Physique Statistique,
Magnétisme et Supraconductivité, DRFMC, CEA Grenoble

Contents

Remerciements **7**

1 General introduction **9**
1.1 Kondo effect . . . 11
1.1.1 Metals with impurities . . . 11
1.1.2 Scattering by impurities . . . 12
1.1.3 Kondo effect at low temperatures . . . 15
1.1.3.a Perturbation expansion . . . 15
1.1.3.b Scaling . . . 15
1.1.3.c Numerical renormalization group approaches . . . 16
1.1.3.d Local Fermi liquid . . . 17
1.1.3.e Bethe-Ansatz . . . 17
1.1.3.f Large-N approach . . . 17
1.1.4 Universality and crossover . . . 18
1.1.5 Phase shift . . . 18
1.2 Measuring the electron transmission phase . . . 19
1.2.1 Quantum dots . . . 19
1.2.2 Transport properties of the quantum dots . . . 21
1.2.2.a Coulomb Blockade . . . 21
1.2.2.b Kondo effect in quantum dots . . . 22
1.2.3 Two-terminal Interferometers. Experiment of Yacoby et al. Phase locking. . . . 23
1.2.4 Open interferometers . . . 28
1.2.4.a Experiment of Schuster. Coulomb blockade regime. . . . 28
1.2.4.b Experiment of Heiblum. Kondo correlation and unitary limit regimes. . . . 30
1.2.5 Theoretical works . . . 34
1.2.5.a Phase shift . . . 34
1.2.5.b Phase lapses . . . 35

2 Theoretical analysis of the transmission phase shift of a quantum dot at zero temperature in the presence of Kondo correlations **37**
2.1 Introduction . . . 39
2.2 Scattering Phase Shift . . . 39
2.2.1 Two-reservoir Anderson model . . . 39

2.2.2 Scattering theory for the Anderson model . . . 41
2.2.2.a S-matrix . . . 41
2.2.2.b The Friedel sum rule . . . 42
2.2.2.c The partial Friedel sum rule . . . 44
2.2.2.d Levinson's theorem . . . 45
2.2.3 Landauer conductance and Aharonov-Bohm effect . . . 48
2.2.3.a Landauer approach . . . 48
2.2.3.b Aharonov-Bohm effect in an open interferometer . . . 49
2.2.3.c Experimental check of the dependence of the conductance with the phase shift . . . 50
2.2.4 Scattering phase shift . . . 52
2.2.4.a Diagonalization of the hamiltonian of the Anderson model with two reservoirs . . . 52
2.2.4.b Solution of the Anderson model . . . 53
2.3 Conclusion . . . 58

3 Phase Lapses **63**
3.1 Introduction . . . 65
3.2 Phase lapse at $T = 0$ in the unitary limit and Kondo correlation regimes 65
3.2.1 Magnetic and non-magnetic regimes. Phase diagram at $T = 0$ . . 65
3.2.2 Net current through an Aharonov-Bohm ring . . . 66
3.2.2.a Unitary limit regime . . . 67
3.2.2.b Kondo correlation regime . . . 68
3.2.3 Dependence of the source-drain current with the transmission amplitude of the reference arm t_{ref} . . . 70
3.3 Conductance evolution in the low-temperature ($T \ll T_K$) and high-temperature ($T \gg T_K$) regimes . . . 71
3.3.1 Phase diagram at finite T . . . 71
3.3.1.a $T \ll T_K$ . . . 71
3.3.1.b $T \geq T_K$ . . . 73
3.3.1.c $T \gg \Gamma$ . . . 75
3.3.1.d Experimental situation . . . 75
3.4 Ring current in the Coulomb blockade regime . . . 77
3.5 Conclusions . . . 77

4 Transmission phase shift at finite temperature in the out of equilibrium situation **79**
4.1 Introduction . . . 81
4.1.0.e Quantum dots vs impurity atoms . . . 81
4.1.0.f Nonequilibrium . . . 81
4.1.0.g Anderson model . . . 82
4.1.0.h Calculation of the current . . . 83
4.1.0.i Calculation of the phase . . . 83
4.2 Noncrossing approximation (NCA) . . . 86

4.2.1 Large-N expansion . . . 86
4.2.2 NCA . . . 88
4.3 Slave bosons . . . 90
4.4 Keldysh formalism . . . 92
4.5 NCA for the Anderson model in the slave-boson representation . . . 100
4.5.1 Application to the out-of-equilibrium regime . . . 100
4.6 Numerical solution of the NCA equations . . . 109
4.7 Transmission phase shift of a quantum dot out of equilibrium . . . 113
4.7.1 Phase shift . . . 113
4.7.2 Modelling . . . 118
4.7.3 Results . . . 118
4.7.4 Results for the occupation number . . . 119
4.7.5 Results for the transmission phase shift . . . 120
4.7.5.a Effect of the temperature at equilibrium . . . 120
4.7.5.b Asymptotic behavior . . . 123
4.7.5.c Intermediate regime . . . 125
4.7.5.d Large bias voltage regime . . . 125
4.7.6 Comparison with experiments . . . 127
4.7.7 Conclusions . . . 128
4.7.7.a What is good? . . . 128
4.7.7.b What is bad? . . . 129

General conclusion **130**

List of figures **132**

Bibliography **141**

Remerciements

J’adresse en premier lieu mes profonds remerciements à **Mireille Lavagna** pour m’avoir accueilli dans le cadre d’un stage pré-doctoral et pour m’avoir proposé ensuite un projet de thèse sous son encadrement. Je la remercie pour sa participation active au déroulement de la thèse, pour ses conseils, ses encouragements, sa disponibilité permanente, sa patience, pour m’avoir donné la possibilité de bénéficier de ses compétences et de m’avoir éclairé sur les subtilités relatives à la théorie de la matière condensée.

Je remercie **Andrés Jerez**, le co-directeur de ma thèse, pour les nombreuses discussions, ses conseils, son aide, sa contribution au projet de thèse, pour m’avoir fait bénéficier de sa compréhension des phénomènes complexes et des méthodes adoptées à la théorie de la matière condensée.

Je remercie **Peter Woelfle** et **Gilles Montambaux** pour avoir accepté une lourde charge en étant rapporteurs du manuscrit, ainsi que pour les commentaires et suggestions qu’ils ont apportés.

J’exprime ma profonde reconnaissance au professeur **Philippe Nozières**, qui a accepté de lire mon manuscrit et je le remercie pour l’honneur qu’il m’a fait en présidant le jury chargé d’examiner cette thèse.

Je remercie **Frank Hekking** pour avoir accepté d’examiner ma thèse, pour son soutien et pour sa contribution à ma formation, spécialement dans le domaine de la physique mésoscopique.

J’exprime ma reconnaissance à **Louis Jansen**, chef de SPSMS, pour son soutien tout au long de mon projet de thèse, pour sa disponibilité permanente qui a permis que mon séjour dans son laboratoire se passe dans les meilleures conditions.

Je remercie **Vladimir Mineev**, chef du Groupe Théorie au SPSMS, pour l’intérêt qu’il a exprimé à mon travail, ainsi que pour les nombreuses discussions et suggestions.

Je suis très sincèrement reconnaissant à **Stephan Roche**, **Jacques Villain**, **Jacques Schwiezer**, **Michel Bonnet**, membres du SPSMS, qui ont toujours manifesté une grande curiosité à mon travail, pour leurs conseils sur le fond ainsi que sur la forme de mes exposés scientifiques. Je les remercie pour la chaleur de leur accueil qui m’a permis de m’adapter à la société française, ce qui a rendu mon travail durant la thèse plus efficace.

Je tiens à exprimer ma gratitude à **Ramon Aguado** pour les discussions que nous avons eues et ses conseils qui m'ont aidé à bien avancer la partie de la thèse reliée au déphasage hors équilibre à température finie.

Je remercie **Denis Feinberg**, **Pascal Simon**, **Laurent Saminadayar**, **Christopher Bauerle**, **Karyn Le Hur** pour leur intérêt à mon travail, les nombreuses discussions et suggestions.

J'ai aussi profité de nombreuses discussions avec **Thierry Champel**, **Damien Bensimon**, **Vu Hung Dao**, **François Triozon**, étudiants et post-docs dans le Groupe Théorie du SPSMS. Qu'ils en soient remerciés.

Chapter 1

General introduction

1.1 Kondo effect

1.1.1 Metals with impurities

Conduction electrons in normal metals behave as weakly coupled (interacting) quasi-particles. A good description is provided by the theory of Fermi liquid developed by L. Landau. Considering normal metals containing impurities it was shown that in the framework of the Fermi liquid description the electric resistivity of the metal sample drops when temperature decreases. The resistance starts saturating as temperature is lowered below about 10 K due to static defects in the material. Generally the temperature dependence of the resistance is given by

$$\rho(T) = \rho_0 \left(1 + aT^2\right) \tag{1.1}$$

where ρ_0 is the zero-temperature conductance. ρ_0 comes essentially from the scattering of conduction electrons by static impurities while the quadratic term is due to other types of scattering processes, like the scattering of electrons by electrons or by lattice vibrations, which becomes weaker and weaker as temperature is lowered. The value of the low-temperature resistance depends on the number of defects in the metallic sample but the character of the temperature dependence remains the same. Some metals, however, can have their electric resistance dropped at low temperature and become superconducting. In our work we will not consider the case of superconducting metals and focus instead on normal metals.

However the low-temperature behavior changes drastically when magnetic atoms are added. The electronic shells of these atoms correspond to only partially filled outer d or f shells and may have nonzero net magnetic moment, such as for example cobalt, ^{27}Co, iron, ^{26}Fe, or manganese ^{25}Mn. The resistance of this alloys first decreases and then increases as temperature is lowered. The origin of this increase of the resistance has been the subject of many theoretical studies. It was established experimentally that the minimum appears when and only when the alloy contains magnetic impurities, the resistance minimum is thus a universal phenomenon of dilute magnetic alloys. Another important point was clarified later on through the measurements of the resistance of diluted alloys with an impurity concentration less than 0.1 at.%. This result showed that the residual resistance is proportional to the impurity concentration and increases as temperature is lowered. Thus it was established that the phenomenon is a single impurity effect rather than due to the interaction between impurities.

To summarize, any theoretical analysis is confronted with three main obstacles. The first one is the resistance increase when temperature is lowered. Any source of electron scattering should vanish as temperature is lowered and the scattering probability should decrease in metals except in very special cases. The second one is the fact that residual resistance is not a constant but varies at very low temperatures. The origin of the corresponding energy scale was not clear. The third difficulty is the universality of the phenomenon. A large number of alloys were tested experimentally and all lead to the similar results. From the latter reason one expect the model to be relatively simple and very general, universal for all magnetic alloys. In fact, the standard model introduced

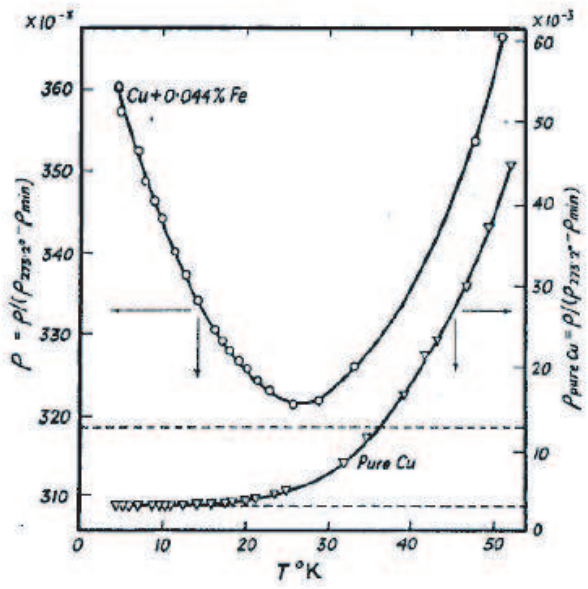

Figure 1.1: Temperature dependence of the resistivity of pure metal (Cu) and dilute magnetic alloy [1].

to describe localized moments in a metal is the so-called s–d model, which was treated extensively and found to give a monotonic decrease of the resistance below the Neel temperature [2, 3].

1.1.2 Scattering by impurities

In the case of the scattering by impurities which do not own any internal degree of freedom, as for example for the scattering by a potential

$$\sum_i v(\mathbf{r} - \mathbf{R_i}) \tag{1.2}$$

the scattering can be analyzed in terms of a one-particle problem since each electron sees the same scattering potential. The situation is very different when the scatterer owns internal degrees of freedom as, for example, spin or orbital degeneracy. After each scattering event the ground state of the scatterer and therefore the potential seen by the electrons may change. Correlations between electrons are introduced and the problem, thus, is no longer a one-particle but rather a many-body problem. In addition to the potential expressed in Eq.1.2 the interaction energy of an electron with a magnetic atom contains a coupling term between the spins $\boldsymbol{\sigma}$ and $\mathbf{S}$ of the conduction electron and the impurity. It can be written in the framework of the s-d model

$$V_s = -(J/n) \sum_i \boldsymbol{\sigma} \cdot \mathbf{S_i}\, \delta(\mathbf{r} - \mathbf{R_i}) \tag{1.3}$$

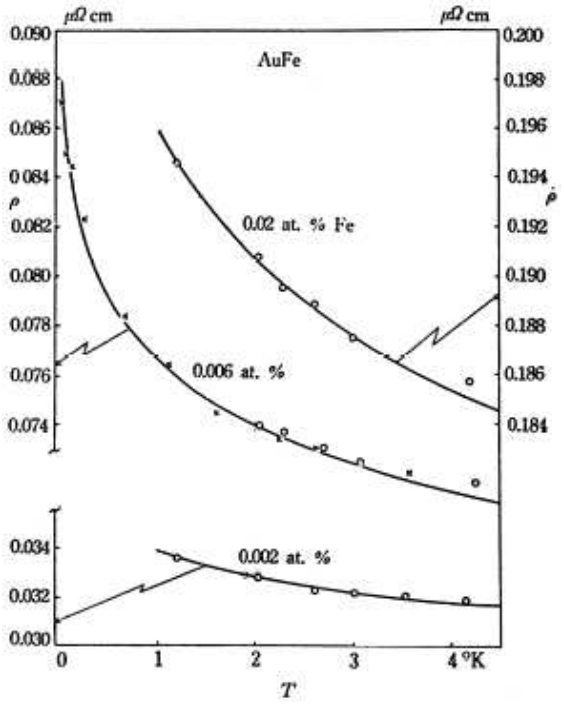

Figure 1.2: Temperature dependence of the resistivity for different concentrations of impurity atoms - comparison between experiment (circles) and theory (curves) [4].

The coefficient J has the dimension of energy. J is several times lower than the electron energies, which are of the order of μ, whereas the usual spin-independent interaction of an electron with an impurity atom is of the order of μ. The latter interactions do not interfere in the scattering probability and one may consider them separately.

The spin part of the interaction gives a contribution of the order of J^2S^2/μ^2 to the scattering probability with respect to the usual interaction. It seems that this is a small effect which can be neglected. It is known that usually the interaction is not weak and one has to take into account higher order terms in the calculation of the scattering probability. However, more detailed calculations in this case show that the result remains similar.

The situation is rather different for the spin-dependent part of the interaction. Although it is smaller than the spinless part there is nevertheless a significant difference. The importance of the higher order corrections was first shown by Jun Kondo [4]. The point is that the interaction described in Eq.1.3 corresponds to the physical process in which the electron spin can flip together with a simultaneous spin-flip of the impurity. When an electron is scattered off an usual atom its spin keeps its orientation. The correction appears to be dependent on the energy of electron leading to a temperature dependence of the resistance. Jun Kondo showed that the minimum of the resistance is due to the process of spin exchange between free electrons and the localized impurity.

The scattering probability calculated at the third order in J is proportional to $\log T$ as a result of the non-commutativity of the spin operators. The sign of this $\log T$ term depends on the sign of J. The scattering amplitude decreases for positive values of J and increases if $J < 0$. This effect has a physical explanation. If $J > 0$, then the interaction is of ferromagnetic type and favors the parallel alignment of spins $\boldsymbol{\sigma}$ and $\mathbf{S}$. In this case the spin-flip scattering is suppressed and the scattering amplitude (and thus the resistance) decreases with temperature. Conversely, for negative J the interaction is antiferromagnetic and the processes with a flip of electron spins are now possible. This leads to an increase of the resistance when the temperature is lowered.

At high temperatures the main contribution to the resistance is due to electron-phonon scattering. The thermal dependence of the resistance is given by

$$\rho = \rho_v + c_m\, a\, \ln \frac{\mu}{T} + bT^5 \tag{1.4}$$

where c_m is the atomic concentration of magnetic impurities, a and b are constants and ρ_v is the contribution to the resistivity brought by the potential scattering. The latter term, resulting from the electron-phonon interaction, increases with temperature. The interplay between the two last contributions gives rise to a minimum in the resistance as a function of temperature at T_{min} given by

$$T_{\mathsf{min}} = \left[\frac{c_m\, a}{5b}\right]^{1/5} \tag{1.5}$$

As can be seen T_{min} is proportional to $c_m^{1/5}$ and hence weakly depends on c_m. J. Kondo have also shown that the scattering cross-section obtained by perturbation expansion diverges as a given temperature. The temperature at which the logarithmic term in the perturbation expansion becomes large is given by

$$T_K \sim (J\mu)^{1/2} \exp\left[-\frac{n}{|J|\,\nu(\mu)}\right] \tag{1.6}$$

where $\nu(\mu)$ is the electron density of states at the Fermi level. This temperature is called the Kondo temperature.

The physical phenomena related to this process are known as the *Kondo effect* whereas the class of theoretical models proposed to describe this effect are called - the *Kondo models*. Since then the properties of Kondo systems have intensively been studied. A complete and detailed overview of this question can be found in the book of A.Hewson [5].

Earlier, in the late 50s the concept of "virtual bound state" was introduced by J.Friedel. These are states which are almost localized due to the resonant scattering by the impurity. This idea was developed later on by P.W. Anderson (1963) in a paper in which he proposed the "Anderson model" [6]. This model has then played a very important role. The model contains, in addition to the resonance at the impurity site, a strong on-site interaction arising from the Coulomb repulsion between impurity electrons. This interaction is responsible for the formation of a localized magnetic moment at the impurity site. For the calculation of the resistance, Kondo assumed

(it was the intrinsic property of the model considered) a local magnetic moment to be associated with the spin **S**. The Anderson model is more general than the s-d model – the latter can be deduced from the former in a given limit. The transformation mapping the Anderson Hamiltonian to the s–d (or Kondo) hamiltonian can be performed using unitary operators. It is known as the Schrieffer-Wolff (canonical) transformation (1966).

1.1.3 Kondo effect at low temperatures

1.1.3.a Perturbation expansion

Perturbation theory expansion in J leads to unphysical predictions such as a divergence of the resistivity at $T = 0$. The summation of the infinite series of leading order logarithmically divergent terms was performed by A.A.Abrikosov [7]. His result extends the calculation of J. Kondo. The expression that he gets for the resistivity leads to reliable results for the ferromagnetic case $J > 0$. For the antiferromagnetic case, $J < 0$, the resistance becomes infinite at the Kondo temperature T_K. The divergence of the resistance results from the formation of a singlet state (Kondo singlet) between the spins of the conduction electrons and the spin of the impurity [8]. In other words, it corresponds to a complete screening of the impurity by the conduction electrons surrounding it, forming what is called the "Kondo cloud".

Perturbation theory provides a good description of the magnetic impurity systems for $T \gg T_K$ but the expansion breaks down at $T \ll T_K$. The perturbation expansion predicts a $\log T$-form for the resistance at low temperatures while experimental studies show that both thermodynamic and transport quantities give power laws in T. The resistivity, for example, deviates from its $T = 0$ value by T^2 terms. Non-perturbative techniques are required to investigate the low-T regime.

1.1.3.b Scaling

In the late 60s Anderson and coworkers introduced a new theoretical framework based on the ideas of scaling [9, 10]. They proposed to perturbatively eliminate higher-order excitations allowing then to derive an effective model valid at low energy scales. The width of the conduction band in this method is gradually reduced so that finally only low-energy excitations are allowed. This procedure generates a set of effective models, each one characterized by its own coupling J. Additional couplings are also generated in this procedure but most of them are "small" and can be neglected. Thus the coupling J varies with the width of the conduction band: $J = J(D)$. The scaling approach leads to the concept of the existence of fixed point when $J(D)$ becomes scaling-invariant. The system is then described by the fixed point corresponding to the value of $J^* = J(D')$ where D' is defined from

$$\left[\frac{d\,J(D)}{dD}\right]_{D=D'} = 0. \tag{1.7}$$

The scaling approach leads to an increase of the effective coupling strength between the spins of conduction electron and of the impurity when D decreases, allowing one

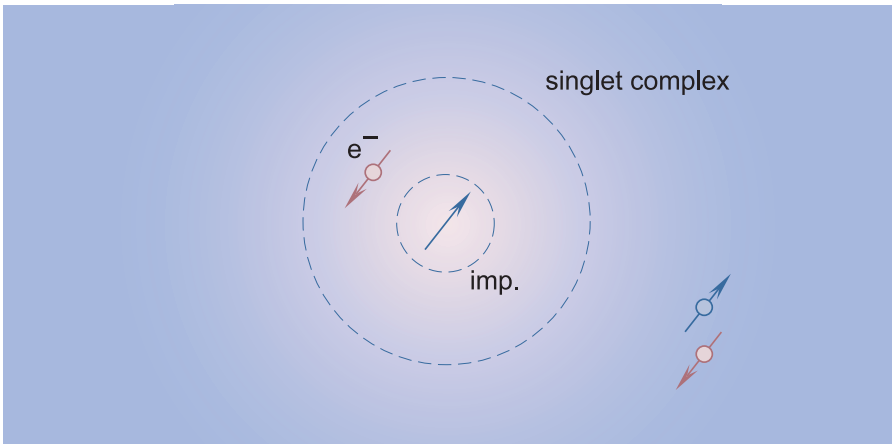

Figure 1.3: Formation of the spin singlet complex at low temperatures. Magnetic impurity virtually traps one conduction electron in order to compensate its magnetic moment.

to describe the low temperature behavior of the system. The perturbation approach breaks down when J becomes too large but Anderson assumed that the approach is still valid at very low temperatures, $T \to 0$. If the scaling is pursued further, the coupling J increases to infinity as D is reduced. Such a scaling behavior implies the formation of a ground state with an infinite coupling in which the impurity is bound to the conduction electrons in a spin singlet state. The behavior at low temperatures is similar to that of a non-magnetic impurity, Fig.1.3.

An outstanding result of the scaling approach is that each set of effective models is characterized by a single energy scale, T_K, which is a scaling invariant. Systems with different values of the parameters J and D but with the same $T_K = T_K(J, D)$ exhibit the same low energy behavior. Hence, for example, the low-temperature dependence of the resistance is given by

$$\rho(T) = F\left(\frac{T}{T_K}\right) \tag{1.8}$$

where $F(x)$ is a universal function.

1.1.3.c Numerical renormalization group approaches

An important contribution was made by K.G.Wilson. He developed a non-perturbative method - the numerical renormalization group approach (NRG). Wilson combined the renormalization group ideas coming from field theory with scaling arguments derived from condensed matter physics. He was then able to confirm Anderson's hypotheses [11, 12]. Wilson, after solving numerous technical problems, obtained the solution for the ground state and the low-energy excitations of the s-d (Kondo) model with impurity spin $S = \frac{1}{2}$. One of the more spectacular results concerns the value of the ratio χ/γ (where χ is the magnetic susceptibility and γ is the low temperature specific heat coefficient) named since then as the Wilson ratio. The value of this ratio was found to be twice the value of non-interacting electrons.

1.1.3.d Local Fermi liquid

P. Nozières gave an interpretation of Wilson's low temperature results in terms of a Landau Fermi liquid theory [13]. At low temperatures $T \ll T_K$ the impurity spin is completely screened, i.e. the total spin of the composite formed by the impurity and the screening conduction electrons is zero. This composite induces polarizability effects. One electron polarizes the composite and then this polarized composite acts on another electron. This mechanism provides an indirect interaction between conduction electrons located in the vicinity of the composite. Therefore, an interaction is induced between conduction electrons leading to the formation of a local Fermi liquid. The problem of the magnetic impurity coupled to a gas of non-interacting electrons is then replaced by that of quasiparticles interacting through the non-magnetic composite. The latter interaction is local, acting at the site of the impurity hence the name of "local Fermi liquid".

Within this description Nozières gave a simple derivation of the χ/γ result as well as an exact calculation of the T^2 coefficient for the resistivity. In a phenomenological way Nozières incorporated in his Fermi liquid description the values of the parameters extracted from Wilson's calculations in the Fermi liquid description.

1.1.3.e Bethe-Ansatz

In the early 80s N. Andrei [14, 15] and independently P.B. Wiegmann [16, 17] showed that the Kondo model is an integrable model and found the exact solution using the Bethe-Ansatz. They derived a set of integral equations the resolution of which allows them to derive the temperature behavior of thermodynamic quantities over the whole range of temperatures. This result confirmed Wilson's calculations. More importantly the method proved to be generalizable to other models like, for example, Anderson model. Most of the models proposed for the description of dilute magnetic alloys were proved to be integrable. Let us remind that the Bethe ansatz method, originally proposed to solve the 1D Heisenberg model, was used to solve other one-dimensional models. The condition behind is that only the electronic waves of s-wave symmetry contribute to the scattering off the Kondo impurity (s-wave scattering). Then the problem can be reduced to an effective 1D problem.

1.1.3.f Large-N approach

In order to discuss the results obtained by various experimental techniques is physical systems, such as photoemission and neutron scattering experiments, the dynamic response functions are required. These functions can not be calculated in the framework of the Bethe anzats. Many approximate techniques then were developed based on large-N approaches where N is the degeneracy of the localized states. In some physical systems the degeneracy of the localized state can be as large as $N = 6$ for Ce or $N = 8$ for Yb. Asymptotically this description gives the exact result in the limit $N \to \infty$. At finite N, one needs to introduce $1/N$ (or $(1/N)^2$) corrections. This is done by accounting for the gaussian fluctuations around the mean field solution, or using other

variational or diagrammatic techniques. These methods were used to calculate the one electron density of states and the dynamic susceptibility. What was clearly shown was the formation of a very narrow many-body resonance in the density of states at the Fermi level in the Kondo regime (known as the Kondo resonance). This resonance is responsible for the anomalous low-temperature behavior of many physical quantities.

1.1.4 Universality and crossover

One of the most essential property of the Kondo effect is the universality. It was found that all physical quantities are universal functions of energy (T or H for example) renormalized by the Kondo temperature T_K: T/T_K, H/T_K ... when the conduction bandwidth D is the largest energy scale of the problem. This property implies that in a set of experimental systems corresponding to different values of parameters, the measured physical quantities exhibit the same (universal) behavior as a functions of renormalized variables T/T_K or H/T_K.

Therefore, the Kondo temperature is the only energy scale of the problem at low temperatures. This energy scale defines the range of applicability of the perturbation expansion. T_K, is neither a property of the host metal nor of the impurity atoms but is generated dynamically by the interaction between them. In the intermediate temperature regime, $T \sim T_K$, which separates the low-energy Kondo regime from the high-temperature (perturbative) regime, the properties of the system change gradually around T_K defining the crossover as a contrast to a phase transition.

1.1.5 Phase shift

Since the impurity is local each quasiparticle state in the electron system is characterized by a given phase shift, δ. All the physical properties of the model at zero temperature can be expressed in terms of this quantity. Thus the phase shift is one of the most fundamental quantity of the model allowing to describe the zero temperature behavior. In dilute magnetic alloys, i.e. for magnetic impurities imbedded in a bulk metal, the direct observation of the phase shift is out of scope.

As we will see later on the scattering phase can not be obtained from simple transport experiments where only conductance (or resistivity) is measured. Only indirect observation is possible. At very low temperatures the effective coupling between the spin of an impurity and the spin of conduction electrons becomes infinite. As a result the scattering crossection reaches its maximum value at $T = 0$ (this regime is often named as the unitary limit). The phase shift then is supposed to be equal to $\frac{\pi}{2}$ in order to ensure the maximum of the resistivity. A direct measurement of the phase shift has become possible in quantum dots thanks to combined progress realized in nanofabrication and quantum interferometry. The results obtained in a series of recent experiments do not confirm the expected value. These results gave us the motivation for the study undertaken in this thesis.

We will present in the next section the different experiments carried out to measure the phase shift.

1.2 Measuring the electron transmission phase

Landauer showed [18, 19, 20] that a tunnelling event can be considered as a scattering experiment. In the case of a single plane wave scattered by a center, the conductance is shown to be proportional to the square of the magnitude of the transmission amplitude of the scatterer. It is therefore obvious that the difference of phase between the incoming and outgoing electron waves can not be measured in a transport experiment. In coherent processes, the phase of the transmission amplitude plays a role and brings additional information which is not contained in conductance measurements. The phase can be determined by using Aharonov-Bohm effect which directly probes both the transmission amplitude and probability provided that transport is coherent. In general, the Aharonov-Bohm ring conductance shows oscillations as a function of a magnetic field penetrating its inner core, with a periodicity equal to one flux quantum h/e. One thus expects these oscillations to persist when a quantum dot is embedded to one of the arms of Aharonov-Bohm ring as soon as transmission through the quantum dot is coherent.

The idea and the practical implementation of devices for measuring the electron transmission phase through a quantum dot was developed in a series of ingenious experiments [21],[22] at the Weizmann Institute. The experiments utilized an Aharonov–Bohm (AB) ring with a quantum dot embedded in one of its arms. The measurements of the electron phase revealed a number of unexpected results. The technique for measuring the electron phase and the main experimental results are described in this section.

1.2.1 Quantum dots

The interest in measuring the transmission phase resulting from the scattering off a quantum dot is due to certain similarities existing between real atoms and quantum dots in their electronic properties. A quantum dot can be viewed as a large atom [23, 24, 25, 26, 27, 28] the radius of which is of the order of a few hundreds of nm, containing up to a few hundreds of electrons. As it is dictated by quantum mechanics, particles confined in a finite-size box have a discrete energy spectrum with spacing proportional to $(1/L)^D$ where L is the characteristic size of the system and D its dimensionality. The energy spectrum of the dot is constituted by single particle levels, each one being broadened due to tunnelling into and out of the quantum dot. Because of its small electric capacitance the addition of an extra electron into the quantum dot requires a relatively large energy, named as the charging energy $e^2/2C$ where C is the capacitance of the dot. As a result the states corresponding to different values of occupation of the quantum dot, appear to be separated by a large energy gap (with the exception for the case of resonances - when the quantum dot is in a mixed state between $|N\rangle$ and $|N+1\rangle$). Thus the total charge located in the dot is a well defined integer number. It may happen that the quantum dot is occupied by an odd number of electrons. This implies a non-zero total magnetic moment in the quantum dot. A quantum dot in this case behaves as a (atomic-type) magnetic impurity embedded in a host metal.

The quantum dots turn out to be tunable devices. The corresponding parameters, which are out of control in the case of magnetic impurities in bulk metals can now be

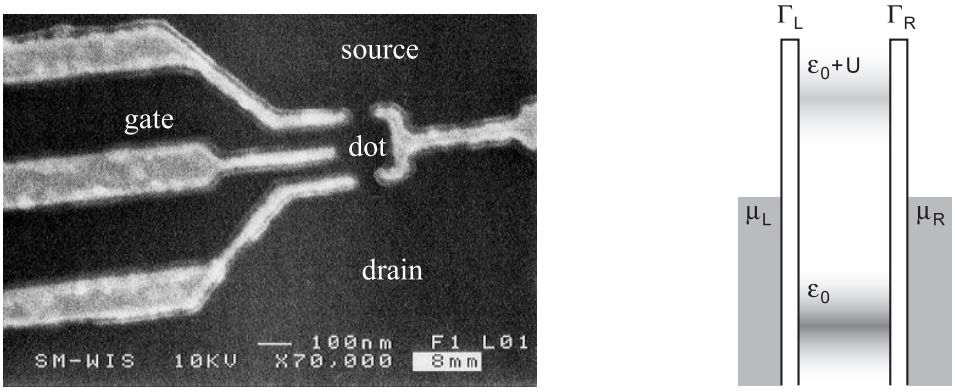

Figure 1.4: Left: Scanning electron microscope image of a typical quantum dot (top view). The black regions indicate the 2DEG, gray regions indicate the metal gates [29]. Right: Schematic representation of quantum a dot structure.

tuned experimentally, opening the way to systematic study of the underlying physics.

A typical quantum dot is represented in Fig.1.4 (left). The experimental setup was realized on the top of a GaAs–AlGaAs heterostructure supporting a two-dimensional electron gas (2DEG). The quantum dot was designed by depositing metal gates on the surface of the heterostructure and subsequently biasing them negatively in order to deplete the electron gas underneath. The dot is connected to the source and the drain via quantum point contacts. A bias voltage, the difference in potential between the source and the drain, can be applied resulting in a current flow through the dot. The conductance of the dot can be adjusted by tuning the lateral gate voltage (upper and lower gates on the left side of Fig.1.4(Left)) which control the transparency of these quantum point contacts via the lateral gate voltages V_{gS} and V_{gD}. This set-up enables a continuous variation of the dot's resistance. A third gate (the central gate on the left side of Fig.1.4(Left)) controls the area and the electrostatic potential in the dot. The dot is about 100×100 nm in size. The quantum dot has usually a very small capacitance C corresponding to a large charging energy $e^2/2C$ - the energy which is necessary to add (or remove) one electron in (from) the dot.

Quantum dots can be modelled as schematized in Fig.1.4 (right). The central region, which corresponds to the dot (see Fif.1.4 (left)), displays a discrete energy spectrum. It is coupled via tunnel barriers to the source and the drain which are modelled by Fermi seas. It is possible to make a one-to-one correspondence between the parameters of this model and the experimental parameters. The energy of the localized level in the dot, ε_0, is equivalent to the gate voltage, V_G. Further, the relation between them is assumed to be linear. By tuning the gate voltage one adjusts the level position in the dot relatively to the chemical potentials in the leads. Once the dot contains N electrons it costs U to add another electron to the dot, where $U = e^2/2C$ is the charging energy. The rates at which electrons enter and leave the dot, Γ_L and Γ_R, are controlled experimentally by tuning the lateral gate voltages, V_{gS} and V_{gD}. The bias voltage, V_{SD}, controls the difference between the chemical potentials in the left and right reservoirs, i.e. $V_{SD} = e(\mu_L - \mu_R)$.

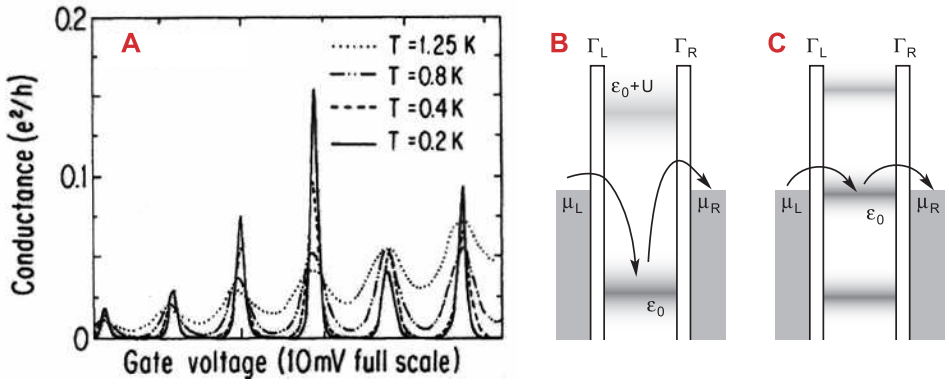

Figure 1.5: (A) Conductance through the quantum dot as a function of gate voltage V_G, [30]. The quantum dot is either in a "locked" (B) or an "open" (C) regime.

1.2.2 Transport properties of the quantum dots

1.2.2.a Coulomb Blockade

When the Fermi energy in the leads, μ, lies within the gap between the topmost occupied, ε_0, and the first empty, $\varepsilon_0 + U$, energy levels the number of electrons in the dot is almost fixed, Fig.1.5(B). Putting an additional electron into the dot costs an extra energy equal to the charging energy $e^2/2C$ where C is the capacitance of the device. When temperature is low enough and the charging energy is large the probability of such an event becomes small and the electron transfer from one to another reservoir is strongly reduced. As a result the conductance through the quantum dot is almost zero [31]. The transport through the dot is said to be locked.

By tuning the gate voltage one can align the energy of the localized level, ε_0, with the Fermi energy in the leads, μ, Fig.1.5(C). In this case the electrostatic energies of the quantum dot with N or $N+1$ electrons are equal. Such a degeneracy between different charge states of a quantum dot allows the electron of one reservoir to tunnel through the dot into the other reservoir. The charge transport is made possible leading to a finite conductance through the dot. The calculations show that the conductance through the quantum dot remaines finite in a narrow region of width $\Gamma = \Gamma_L + \Gamma_R$ around μ or or a thermal window of width T, depending whether Γ or T is the large energy scale.

Experimentally, when tuning continuously the gate voltage V_G and measuring the conductance of a quantum dot, one observes a series of high and narrow peaks separated by valleys of almost zero conductance, Fig.1.5(A). The resulting oscillatory dependence of the conductance $G(V_G)$ is the signature of the Coulomb Blockade effect. The dot is then said to be in the Coulomb Blockade regime. The contrast between the conductance in the Coulomb blockade valleys and resonances becomes larger and larger as temperature is lowered. Conductance peaks correspond to values of the gate voltage V_G for which the energy of one of the localized levels in the dot is close to the Fermi energy in the leads. For all the other values of V_G the conductance is very low. When V_G continuously increases and the conductance passes a resonance, it means that one electron is added to the dot. The neighboring valleys thus can be characterized by the

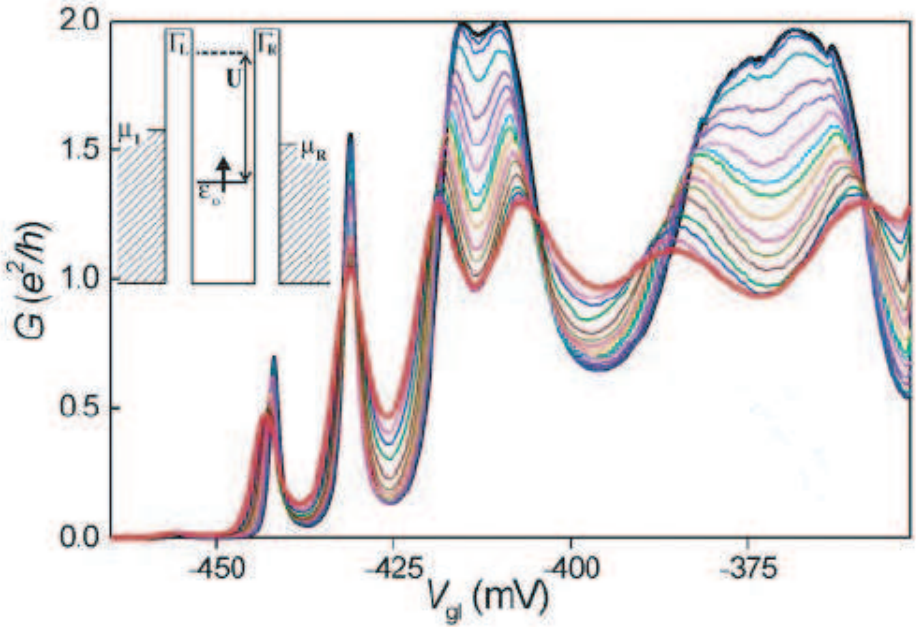

Figure 1.6: Conductance as a function of V_G for different temperatures. T ranges from 15 mK (black trace) up to 800 mK (red trace) [32].

number of electrons in the dot. The gate voltage V_G effectively controls the occupation of the dot. Depending on the parity of the occupation in the dot, one can distinguish "even" or "odd" conductance valleys.

As temperature increases the probability for one electron to tunnel through the blockaded dot increases. The conductance in the valleys then increases with temperature in both the "even" and "odd" conductance valleys. The peaks becomes larger and of smaller height when temperature increases.

1.2.2.b Kondo effect in quantum dots

If an odd number of electrons occupies the dot, the total spin of the dot is necessarily non-zero. It has a minimum value of $S = \frac{1}{2}$. This localized spin S, coupled to the source and the drain, mimics the behavior of a localized magnetic impurity in the host metal. As we will show later, these two systems are equivalent and many of Kondo phenomena can be expected to occur in quantum dots.

One of the most distinct features between quantum dot and magnetic impurity in metal is related to their different geometries. In real metals the magnetic impurities scatter the conduction electrons which strongly contributes to the resistance. In a quantum dot all the electrons have to travel through the scatterer, as there is no electrical path around it. In this case the onset of a new scattering mechanism due to the Kondo resonance contributes to the conductance. As the resistance in bulk metals in the Kondo regime, the conductance of the quantum dot at low temperatures depends only on the ratio T/T_K, where T_K is Kondo temperature.

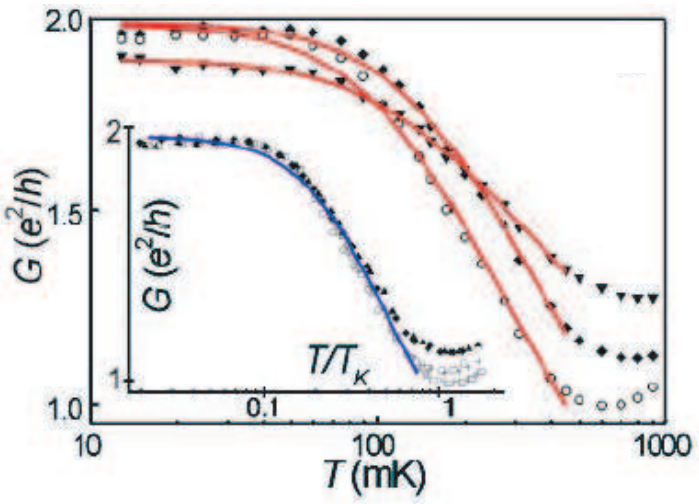

Figure 1.7: Conductance as a function of temperature for different values of gate voltage V_G. Plotted as functions of T/T_K all the curves show a universal behavior [32].

The conductance of a quantum dot as a function of the gate voltage was measured in the experiments of D.Goldhaber-Gordon et al. [32], Fig.1.6. For an even number of electrons, the conductance decreases as the temperature is lowered from 0.8 K to 15 mK. This behavior indicates that there is no Kondo effect when the number of electrons in the dot is even. In contrast, when the number of electrons is odd the conductance of the dot increases when the temperature is lowered. Moreover, at lowest temperatures the conductance approaches the quantum limit of conductance $2e^2/h$. In terms of the scattering description of electronic transport, the quantum dot in the limit $T = 0$ becomes completely transparent, the probability of an electron to be transmitted from the source to the drain equals unity. The dot is said to be in the unitary limit (UL) regime. In the low temperature limit the conductance measured at different values of the gate voltage V_G, i.e. different values of ε_0, shows clearly different temperature behavior. But plotted as a function of T/T_K, all the curves lie on top of each other, i.e. the experimental data exhibit universal behavior below T_K. The three following features — the asymmetry in the low-temperature behavior of the conductance between the Coulomb blockade valleys of different parity; the increase of the conductance in the "odd" valleys reaching the unitary limit $2e^2/h$ under some condition its universal low-temperature behavior — constitute clear manifestations of the Kondo effect.

1.2.3 Two-terminal Interferometers. Experiment of Yacoby et al. Phase locking.

The first experiment addressing the electron phase through a quantum dot was realized by Yacoby et al. [21]. The experiment utilized a novel device (see Fig.1.8) to measure the phase evolution through the dot against a reference phase which is supposed to be fixed. The Aharonov-Bohm interferometer was composed of two arms forming the ring. The quantum dot was inserted in one arm of an Aharonov–Bohm ring. The basic idea

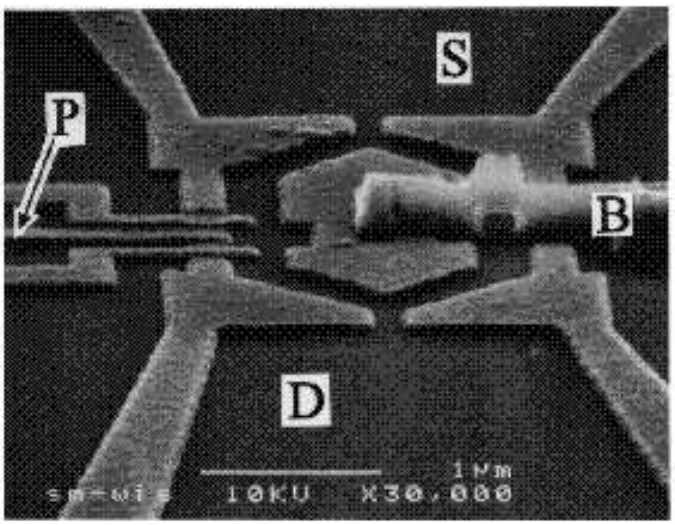

Figure 1.8: Electron micrograph of the Aharonov-Bohm interferometer used in the [21]. The black regions indicate the 2DEG, gray regions indicate the metal gates. Electrons flow between source and drain through the left or the right arm of the Aharonov–Bohm ring. The quantum dot is inserted in the left arm. The central metallic island is biased via an air bridge (B) [21].

is to extract the transmission phase through the quantum dot from the phase of the Aharonov–Bohm current collected at the drain. The dot was about $0.4\mu m \times 0.5\mu m$ in size. A special lithographic process, invoking a metallic air bridge (B), enabled to contact the center metal gate that depleted the electrons underneath the ring's center. Each of the arms of the Aharonov-Bohm ring supported a few conducting modes. The ring was connected to two external contacts, source (S) and drain (D), between which a small voltage was applied.

The elastic mean free path in the two–dimensional electron gas was estimated to be about 10 μm while the diameter of the Aharonov–Bohm ring was $L \approx 1 - 1.5\ \mu m$. The phase coherence length L_ϕ was larger than the ring's circumference. The quantum dot had a resistance of $1M\Omega$ and a very small capacitance $C \approx 160\ aF$ corresponding to the charging energy $e^2/2C \approx 0.5\ meV$. The dot contained around 200 electrons. The bare average single–particle level spacing was $\Delta \approx 40\ \mu eV$. The experiment was performed at a temperature around 100 mK corresponding to the thermal energy $kT \approx 9\ \mu eV$. The intrinsic width Γ of the Coulomb peaks was estimated from the conductance peak height to $\Gamma \approx 0.2\ \mu eV$. These scales imply that the quantum dot was in the Coulomb blockade regime, and that the transmission at each Coulomb peak resulted from resonant tunnelling through a single resonant level of the quantum dot.

The experiment [21] demonstrated for the first time that part of the tunnelling current through a quantum dot is coherent. The experimental evidence is presented in Fig.1.9. The figure shows the ring current as a function of the plunger voltage V_P (also often referred as the gate voltage, V_G) for a fixed small source–drain voltage. The ring current was obtained by subtracting from the total current across the ring – a large

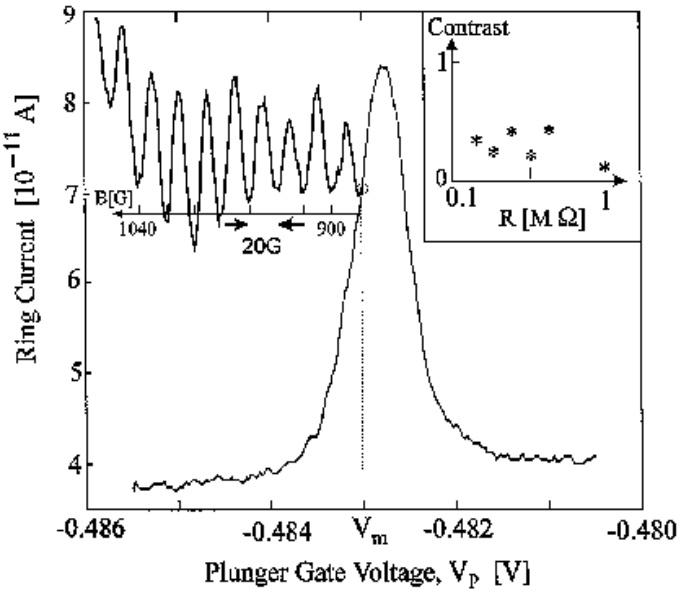

Figure 1.9: The ring current as a function of the plunger gate voltage. The large current of the reference (right) arm has been subtracted. The top left part shows the Aharonov–Bohm oscillations of the current as a function of magnetic field at fixed $V_P = V_m$. In the inset: oscillation contrast defined as the amplitude of the ring current oscillations vs. the average current through the dot [21].

V_P–independent background current due to the right arm. The Coulomb blockade in the dot manifest itself in a series of sharp conductance peaks in the ring current at fixed magnetic field. Fixing the voltage V_P on the side of a current peak and sweeping the magnetic field, one observes periodic current oscillations. The period of the oscillations corresponds to one flux quantum threading the area of the ring, in very good agreement with the expected period of Aharonov–Bohm oscillations, providing a direct indication that transport through the quantum dot has a coherent component. The oscillation contrast, defined as the peak–to–peak current over the average current, does not varies much and is in the range 0.2 to 0.4.

In a next step, the current oscillations were investigated at different values of the plunger voltage V_P. A change in V_P was expected to modify both the magnitude and the phase of the transmission amplitude through the dot. The experiment was motivated by the idea that the change in the transmission phase would be directly reflected in a shift of the Aharonov–Bohm oscillations which, in turn, could be seen experimentally. This one–to–one correspondence is suggested by the following argument: suppose the ring and the leads support only one conducting channel. According to the Landauer formula, the zero–temperature current between the leads is proportional to the ring transmission coefficient $|t(E_F)|^2$ at the Fermi energy E_F. For fully coherent transport, $t = t_R \exp(2\pi i \Phi/\Phi_0) + t_L$, where t_R and t_L are the transmission amplitudes through the right and the left arm, respectively, Φ is the flux through the ring and Φ_0 the flux

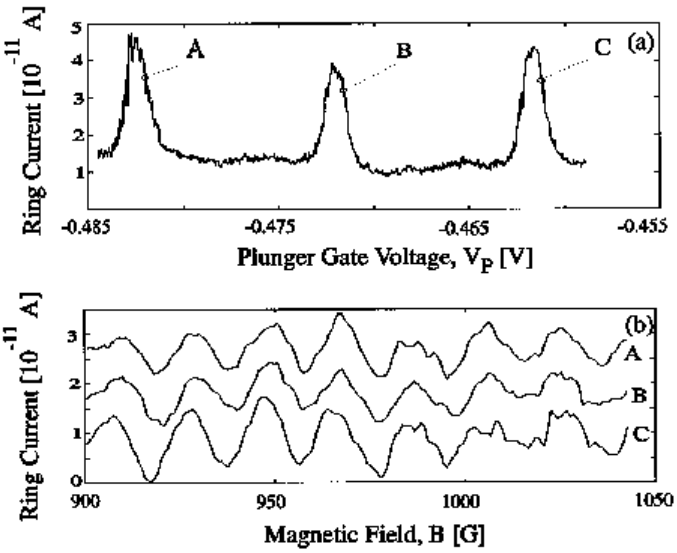

Figure 1.10: (a) A series of three Coulomb peaks and (b) the current oscillations measured at the marked points A, B, and C. All oscillations are seen to be in phase. The large current of the reference (right) arm has been subtracted [21].

quantum. This leads to the interference term

$$2\mathrm{Re}\{t_L t_R^* \exp(-2\pi i\Phi/\Phi_0)\} = 2|t_R||t_L|\cos(\xi_L - \xi_R - 2\pi\Phi/\Phi_0), \tag{1.9}$$

where $\xi_R = \arg(t_R)$, $\xi_L = \arg(t_L)$. Any shift in the phase $\xi_L - \xi_R$ should thus be directly reflected in a shift of the Aharonov–Bohm oscillations.

The above argument turned out to be incorrect. It neglects multiple reflections through the ring. The argument fails in particular for a two–terminal geometry, i.e. a ring connected to two external leads. It was realized just after the experiments were performed that Onsager relations valid for a two–terminal device restrict the phase of the Aharonov–Bohm oscillations to either 0 or π, spoiling the correspondence between the Aharonov–Bohm phase and the transmission phase through the quantum dot. This property is general for systems where current is conserved and time-reversal symmetry is satisfied [33]. Only abrupt jumps between the two allowed phase values are possible. Physically, this is a direct result of the interference between the different paths that traverse the ring. Nevertheless the idea of measuring the electron phase was later realized in the multiple–terminal device of Schuster et al. [22].

Figure 1.10 shows the ring current and the Aharonov–Bohm oscillations measured at three successive peaks. The oscillations at similar points (A, B, and C in the figure) have the same Aharonov–Bohm phase. This repetition of the phase was found within the whole sequence of Coulomb peaks (comprising 12 peaks) investigated in the experiment. The evolution of the Aharonov–Bohm phase along a single Coulomb peak is displayed in Fig. 1.11. Four different interference patterns taken at the points 1, 2, 3, and 4 specified in Fig. 1.11(a) are shown in Fig. 1.11(b). The Aharonov–Bohm phase of the patterns jumps by π as one sweeps through the peak. The jump happens abruptly between the points 2 and 3. This can be seen in Fig. 1.11(c) which summarizes the phase

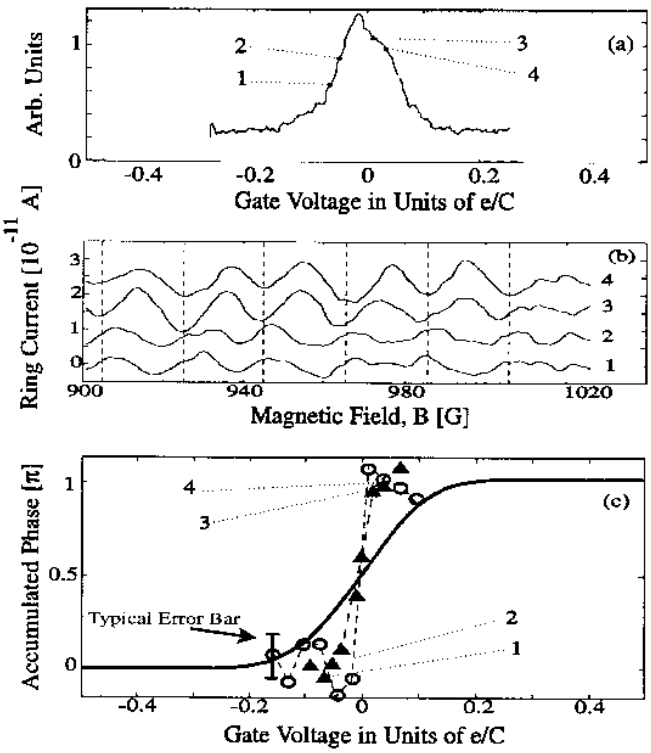

Figure 1.11: Evolution of the Aharonov–Bohm phase through a current peak. (a) Current as a function of gate voltage (or plunger voltage $V_P \equiv V_G$) at a current peak. (b) A series of interference patterns taken at the points specified in (a). Note the phase jump between patterns 2 and 3. (c) Phase measured at two peaks (circles and triangles). The broken line is guide to the eye. The expected behavior of the quantum dot transmission phase in a 1D resonant tunneling model is shown by the solid line [21].

measurements along a Coulomb peak. The sharp jump in the measured Aharonov–Bohm phase is in contradiction with the expected phase evolution of the transmission amplitude assuming resonant tunnelling through a single level of the quantum dot. The latter phase increases smoothly on the scale of the peak width (which is of order kT). This disagreement arises from the fact that closed two-terminal Aharonov-Bohm ring can not be described by the "two-slit" result expressed in Eq.1.9 and one needs to take multiple reflections through the ring into account in order to recover the correct result.

1.2.4 Open interferometers

1.2.4.a Experiment of Schuster. Coulomb blockade regime.

The Aharonov–Bohm phase in a two–terminal device is restricted to 0 or π. This phase rigidity which is a general property of closed interferometers does not exist in a double-slit-like interference set-up as realized by a many-terminal device. Schuster et al. [22] used such a device, Fig.1.12, to measure directly the magnitude and the phase of the transmission amplitude through a quantum dot in the Coulomb Blockade regime. The electron micrograph of the device and a schematic description of the experiment are shown in Figs. 1.12, 1.13. The central element of the device is an Aharonov–Bohm ring with a quantum dot embedded in its right arm. Several contacts are connected to the ring, namely the emitter (E), the collector (C) and a base region (B). The base contacts were held at zero chemical potential in order to collect all back-scattered electrons and to ensure that only two forward propagating electron waves reach the collector. The special type of gates, reflectors, were also introduced into the structure of the interferometer. They reflect diverging electrons into the two–slit device and towards the collector. The reflectors were necessary to enhance the collector signal that could otherwise not be measured. All contacts were designed by negatively biased gates on top of the heterostructure.

The quantum dot contained roughly 200 electrons with a mean single–particle level spacing around 55 μeV. The temperature of the two–dimensional electron gas was $T_{el} \approx 80$ mK. The intrinsic (zero–temperature) width Γ of the Coulomb peaks was estimated to be of the order or even larger than kT. Collector and emitter support only one transverse mode. The quantum dot in this experiment was in the Coulomb Blockade regime.

At low temperatures both the phase coherent length and the elastic mean free path exceed the size of the sample. Then collector current was measured. They observed oscillations of the current as a function of magnetic field with period Φ_0. The absence of higher harmonics (with periods Φ_0/n) strongly suggests that the two direct paths predominantly contribute to the interference.

It the experiment the measured quantity was the voltage drop V_{CB} between collector and base for a fixed excitation voltage V_{EB} applied between the emitter and the base. The Aharonov–Bohm interference in the transmission coefficient T_{EC} leads to an oscillatory contribution to V_{CB} from which the Aharonov–Bohm phase is extracted. Fig. 1.14(a) shows V_{CB} measured as a function of the gate voltage V_P for a fixed magnetic field. One observes pronounced resonance peaks as expected for a quantum dot in

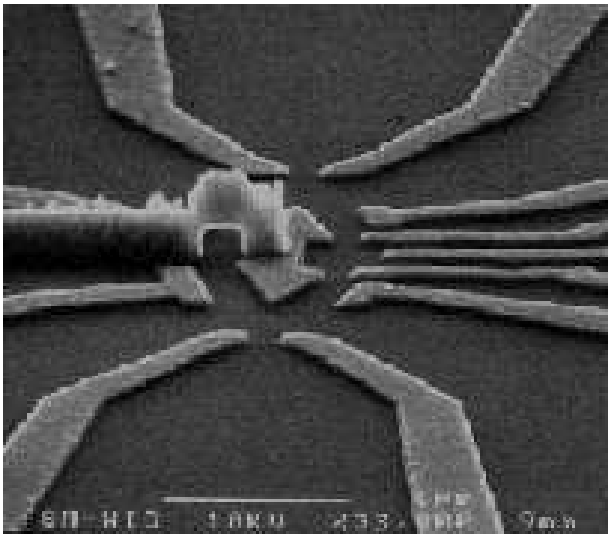

Figure 1.12: A top-view scanning electron micrograph of the double–slit device used in the Schuster–experiment [22]. The grey areas are metallic gates on the top of the heterostructure. The quantum dot is inserted in the right slit [22].

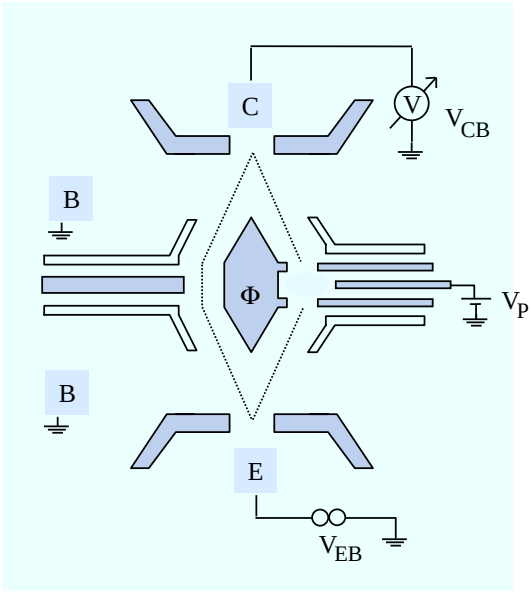

Figure 1.13: Schematic description of the device structure of the double-slit-like experiment. An Aharonov–Bohm ring is coupled to an emitter (E), a collector (C) and a base region (B). Reflector gates reflect diverging electrons towards the collector. The quantum dot is designed by the central electrode and the three electrodes on the right hand side of the structure [22].

the Coulomb Blockade regime. When the magnetic field is changed, the collector signal shows AB oscillations with the expected period $\Delta B = \Phi_0/A$ where A is the area of the AB ring. The observed oscillation patterns measured at the four points 1, 2, 3, and 4 close to a resonance are shown in Fig. 1.14(b). The oscillation pattern shifts smoothly as one moves through the resonance. Fig. 1.14(c) displays the phase and the squared magnitude of the AB signal at a resonance peak. The data points are represented by full circles. The phase shows the expected monotonic rise by π over the width of the resonance.

Schuster et al. compared their data with a theoretical model for resonant scattering. They described the coherent part t_{QD} of the transmission amplitude through the dot by the Breit–Wigner formula [34]

$$t_{\mathrm{QD}} = iC_N \frac{\Gamma_N/2}{E_F - E_N + i\Gamma_N/2}, \tag{1.10}$$

where C_N is a complex amplitude, E_F the energy of the electrons transmitted through the device, and E_N and Γ_N the energy and the width of the resonance in the quantum dot. Both the squared magnitude $|t_{\mathrm{QD}}|^2$ and the phase $\arg t_{\mathrm{QD}}$ are compared with experimental data in Fig. 1.14(c) and are found to be in very good agreement with Eq.1.10. These results clearly show that the transmission through the dot in the Coulomb Blockade regime is correctly described by a Breit-Wigner formula.

The collector voltage V_{CB}, the magnitude, and the phase of the AB oscillations measured over a sequence of five peaks are shown in Fig. 1.15. The striking observation is that the phase is very similar at all peaks. The phase increases roughly by π at each peak. Note that the peaks widen and start to overlap as the plunger voltage increases. At the same time, the overall variation of the phase is reduced. The likely origin of these effects is the electrostatic influence of the plunger on the point contacts at the quantum dot. They open slightly with increasing plunger voltage. A striking feature of the data is the sharp phase lapse by π between the resonances. The phase lapse occurs when the magnitude of the AB oscillations vanishes. Using the simple arguments brought by the scattering off a series of distant quasi-localized states the phase of the transmission amplitude should increase by π each time a localized state crosses the Fermi level in the leads. Thus the phase should exhibit a staircase-like behavior and the phase in the neighboring valleys (or peaks) should differ by π. The experimental observations are in contradiction with this result. Numerous works have been devoted to this subject but it seems that a more fundamental explanation is still lacking.

1.2.4.b Experiment of Heiblum. Kondo correlation and unitary limit regimes.

Similar experiments were performed using smaller quantum dots [36, 35] compared to the previous ones [21, 22]. In the left arm of the AB interferometer a tiny quantum dot (180 nm × 200 nm) is embedded, Fig.1.16. This quantum dot has a charging energy $U_C \sim 1.5$ meV and a relatively large single-particle mean level spacing $\Delta \sim 0.5$ meV, allowing strong coupling to the leads without overlapping of the energy levels in the quantum dot. The Kondo temperature for such a quantum dot can be as high as 1.5

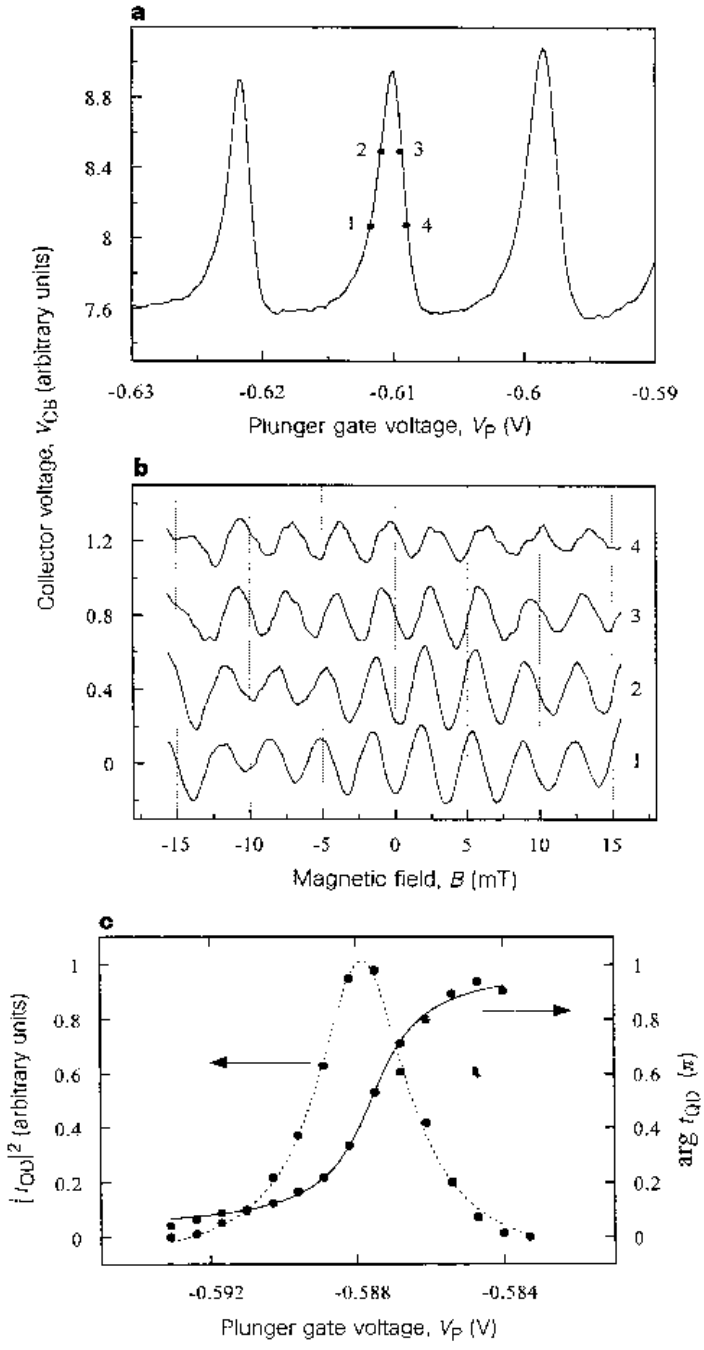

Figure 1.14: Conductance and phase evolution along a Coulomb peak. (a) Resonance peaks as a function of the plunger gate voltage. (b) A series of interference patterns taken at the points specified in (a). (c) Squared magnitude and phase of the Aharonov–Bohm oscillations (dots). The solid and dashed line are fits for the phase and the squared magnitude obtained with a Breit–Wigner model [22].

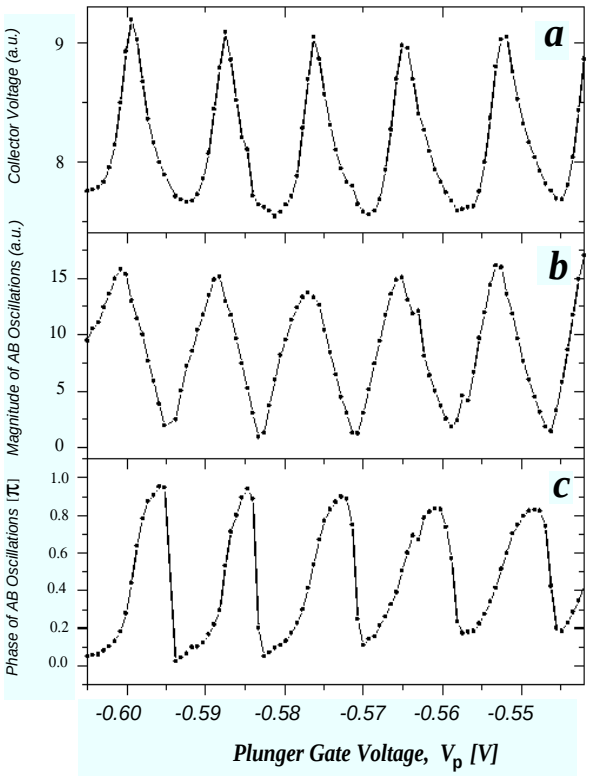

Figure 1.15: (a) A series of Coulomb peaks; (b) Magnitude of the Aharonov–Bohm oscillations; (c) Phase of the Aharonov–Bohm oscillations as a function of plunger gate voltage. The solid lines are guides to the eye [22].

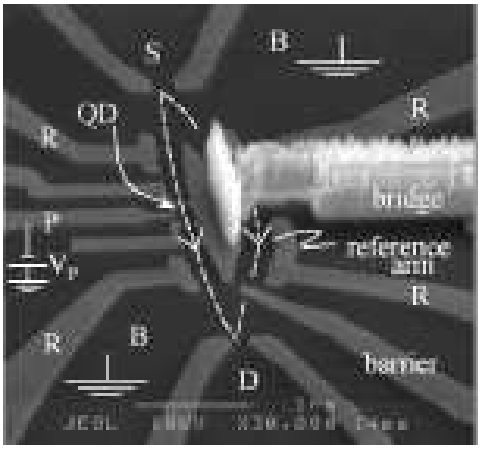

Figure 1.16: A top-view scanning electron micrograph of the double–slit device used in the Yang–experiment [35]. The black zones represent 2DEG and the grey areas are metallic gates on the top of the heterostructure. The quantum dot is inserted in the left slit. The barrier gate is added in order to shut off the reference arm and test the bare quantum dot [35].

K. Thus the low-temperature behavior, $T \ll T_K$, is made accessible for experimental investigations. The Aharonov-Bohm ring is supplied with a new gate - the barrier gate, which allows to shut off the reference (right) arm and test the bare quantum dot.

First, measuring the conductance through the bare quantum dot (with the pinched off reference arm) Kondo correlations were identified. A peak conductance of $\sim 1.9e^2/h$ was measured, suggesting that the quantum dot is in the unitary limit regime. The conductance in two neighboring valleys with (presumably) zero net spin in the quantum dot is found to be suppressed as temperature lowered, as it is expected for the Coulomb blockade regime. As the temperature or the dc bias voltage across the quantum dot is increased, a valley is formed and the single broad peak dissolves into two CB peaks, however the conductance of the outer CB valleys increases. This is the typical behavior of a conductance of the quantum dot with Kondo correlations.

The phase and magnitude of the complex transmission amplitude through the quantum dot are obtained as previously - from the measurements of the drain current as a function of the magnetic field and plunger gate voltage.

The main results are reported in Fig.1.17. The complex transmission amplitude (phase and magnitude) are plotted vs plunger gate voltage for different couplings between the leads and the quantum dot. Reducing the coupling strength is equivalent to reducing the Kondo temperature T_K. The coupling strength gets weaker from (a) to (d) in Fig.1.17 and the quantum dot moves from the Kondo regime to the Coulomb blockade regime. In the unitary limit the phase exhibits an almost linear growth of 1.5π (a). In the regime (b) it develops a plateau and later, as the coupling weakens further, the quantum dot enters into the Coulomb blockade regime observed in previous experiments [22]. In the case of low coupling to the leads and higher temperature, $T_{el} \sim 100$ mK, [36] the phase span through the Kondo valley is $\sim 2\pi$ with a clear plateau at π.

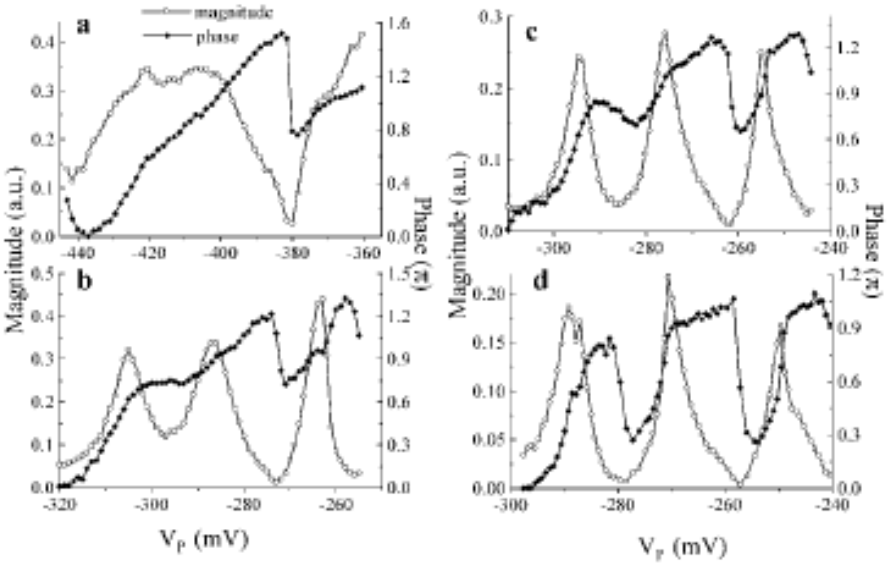

Figure 1.17: The complex transmission amplitude (phase and amplitude) of the quantum dot as a function of energy (plunger gate voltage) for different coupling strengths of the quantum dot to the leads. The coupling gets weaker from (a), the unitary limit, to (d), Coulomb blockade regime [35].

The phase exhibits a striking behavior in the CB valley. While the phase lapse for the quantum dots in the Coulomb blockade regime is always of order of π, the phase in each CB valley returns to zero, the phase lapse in the CB valley following the Kondo valley does not returns to its initial value.

The evolution of the phase and magnitude of the transmission amplitude with increasing temperature or bias voltage is also measured. In both cases the Kondo correlations are found to be suppressed.

To summarize, two main (troubling) features stand out. The first one is the behavior of the phase as a function of the gate voltage and its large span, twice larger than the theoretically predicted value [37, 38] when the system is in the Kondo regime. The second striking feature is the phase behavior in the CB regime adjacent to the Kondo correlated regime with the existence of the phase lapse or abrupt phase evolutions. The origin of the phase lapses has not been well understood so far.

1.2.5 Theoretical works

In this section we will briefly review the main results obtained for the transmission phase shift.

1.2.5.a Phase shift

One of the first theoretical predictions for the phase shift was made by D. Langreth in 1966. He analyzed the scattering states and calculated the S-matrix in the framework of

the 3D Anderson model. He showed that the Friedel sum rule is an exact consequence of the Anderson Hamiltonian for the case where there is no local moment. His main conclusion can be outlined in the following way: at zero temperature the sum of all the phase shifts at the Fermi level is equal to π times the charge displaced by the impurity. For the single-level Anderson model in the absence of magnetic field the phase shifts per each spin are equal and each of them takes the value of $\pi n_0/2$, where n_0 is total occupation of the impurity site.

In the context of quantum dots the important contribution was made by D. Gerland and collaborators in 2000. They analyze the dependence of the transmission phase shift as the function of the energy of the localized level (or applied gate voltage) for a quantum dot in presence of Kondo correlations. The authors assume that the phase shift measured in the Aharonov-Bohm interferometry experiment at zero temperature and magnetic field, coincide with the phase of the retarded Green function of the localized electrons evaluated at the Fermi level. The phase is then calculated using the numerical renormalization group approach (NRG) and Bethe anzats. In this work authors predict that the transmission phase shift of a quantum dot in the presence of Kondo correlations is equal to $\pi/2$ in the unitary limit regime. The dependence of the phase shift with bias voltage and temperature is also analyzed and we will come back to this question in Chapter 4.

1.2.5.b Phase lapses

Simple arguments show that the phase in the neighbouring conductance valleys should differ by pi, exhibiting the so called "off-phase" behaviour that clearly contradicts the experimental observation. The phase slips in each conductance valley by an amount of π, resulting in the so called "in-phase" behaviour. This phenomenon is largely discussed in the literature. The analysis, however, is restricted only to the case of a quantum dot in the Coulomb blockade regime.

The origin of the phase lapses was first studied by Levy Yeyati and Buttiker [39]. They discussed the subject in terms of the Friedel sum rule. The authors emphasized that one has to take into account the additional charge induced in a conduction region which includes not only the quantum dot but also the Aharonov-Bohm ring. In a model calculation for a two terminal device using proper values of the extra charge, sequences of two or three consecutive in-phase resonances are found.

The connection between the Friedel sum rule and the phase lapses was reconsidered by Lee [40] and Taniguchi and Buttiker [41]. They conclude that the transmission phase shift can deviate from the Friedel sum rule at some special points where the transmission through the quantum dot vanishes. A transmission zero corresponds to a singular point of the transmission phase. The phase jumps abruptly by pi when the system is swept through the transmission zero. The authors also show that the spatial dimension of the scattering region is important: while the neighbouring resonances are always off-phase in strictly 1D systems, both off-phase and in-phase resonances can be found in higher dimensional systems.

The sharp phase lapse between the resonances was investigated by Hackenbroich and

Weidenmuller [42] for the weak coupling regime $\Gamma < T < \Delta$ where Γ is the width of the resonance, T is the temperature and Δ is the mean level spacing. In this regime the transmission amplitude can be reduced to a sum of Breit-Wigner resonances. The obtained phase shows an increase by π on the scale T at each resonance. Between each resonance, the phase slips by π on the scale of the resonance width Γ.

In 1998, a number of authors [43, 44, 45, 46] studied models for the transmission through a quantum dot and found abrupt jumps of the transmission phase. The jumps occurred at singular points where the magnitude of the transmission amplitude vanishes. Transmission zeros were found in numerical studies exploring Fano resonances [43, 44, 45] and the interplay with multiple resonances [46]. In Refs. [43, 44, 45] a quantum dot is modelled as a quasi-$1D$ or $2D$ region. A more general approach to the connection between transmission zeros and in-phase resonances was presented by Lee [40]. He showed that the transmission always vanishes between neighbouring in-phase resonances, provided that the scattering region is connected to two single-channel leads and the system is time-reversal invariant.

In spite of all these efforts a more fundamental explanation is lacking. Each of the proposed mechanisms can be criticized since they rely on some given assumption.

Chapter 2

Theoretical analysis of the transmission phase shift of a quantum dot at zero temperature in the presence of Kondo correlations

2.1 Introduction

We study the effects of Kondo correlations on the transmission phase shift of a quantum dot coupled to two leads in comparison with the experimental measurements made by Aharonov-Bohm (AB) quantum interferometry. We propose here a theoretical interpretation of these results based on scattering theory combined with Bethe ansatz calculations. We show that there is a factor of 2 difference between the phase of the S-matrix responsible for the shift in the AB oscillations, and the one controlling the conductance. Quantitative agreement is obtained with experimental results for two different values of the coupling to the leads.

Quantum dots (QD), small puddles of electrons connected to leads, can be obtained in a controlled fashion thanks to recent progress in nanolithography. Under certain conditions a dot can be modeled as a localized spin coupled to Fermi baths (the leads). A Kondo effect takes place [29, 47, 32] when the temperature is lowered . A key ingredient of the Kondo effect is the phase shift δ an electron undergoes when it crosses the dot. While its direct measurement was out of scope in bulk systems, it became feasible recently in quantum dots via Aharonov-Bohm (AB) interferometery [36]. We mention here the experimental results obtained in two cases corresponding to a strong coupling to the leads [36, 35]. In the unitary limit, the phase shift climbs almost linearly with V_G with a value at the middle of the Kondo enhanced valley which is almost π. At a smaller value of the coupling strength, the phase shift develops a wide plateau at almost π. We will call the latter case the "Kondo correlation regime". Early theoretical work on the phase shift for the bulk Kondo effect [37, 48] predicts $\delta = \pi/2$. In the context of QD, Gerland et al [38] had obtained, on the basis of NRG and Bethe ansatz calculations, a variation of δ with the energy of the localized state leading to a value of $\pi/2$ in the symmetric limit, in disagreement with the recent experimental results quoted above [36, 35]. In this chapter, we propose a new theoretical interpretation of the experimental results based on scattering theory and Bethe ansatz calculations. Our main prediction concerns a factor of 2 difference found between the phase of the S-matrix observed by the phase shift measurements and the phase governing the conductance.

2.2 Scattering Phase Shift

2.2.1 Two-reservoir Anderson model

Let us consider a quantum dot coupled via tunnel barriers to two leads L and R, and capacitively to a gate maintained at the voltage V_G. Following Glazman and Raikh [49] and Ng and Lee [50], one can describe the system by a generalized one-dimensional Anderson model in which the localized state of energy ε_0 lies at the $i = 0$ site, and the sites $i \leq -1$ ($i \geq 1$) simulate the left and right reservoirs. The corresponding hamiltonian is written as follows

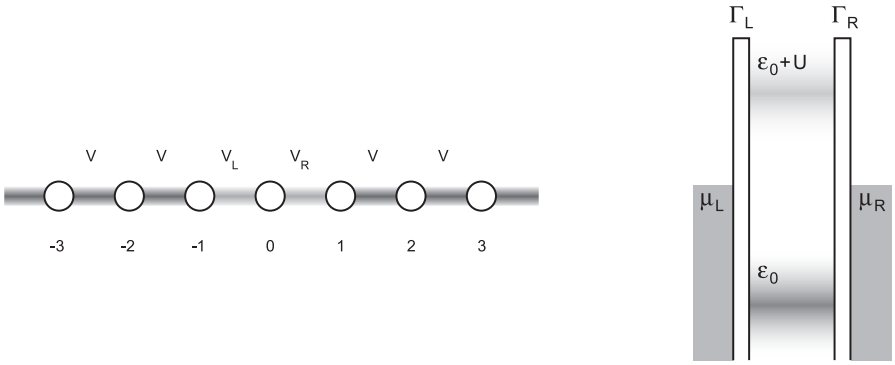

Figure 2.1: A schematic representation of the one-dimentional Anderson model (left). The $i = 0$ site represents the localized state of energy ε_0. The model can be sketched in another way (right) which indicates the inner structure of the impurity.

$$H = -V\sum_{\sigma}\sum_{i\geq 1}(c^{\dagger}_{i,\sigma}c_{i+1,\sigma} + h.c.)$$
$$-V\sum_{\sigma}\sum_{i\leq -2}(c^{\dagger}_{i,\sigma}c_{i+1,\sigma} + h.c.) - V_R\sum_{\sigma}(c^{\dagger}_{0,\sigma}c_{1,\sigma} + h.c.) - V_L\sum_{\sigma}(c^{\dagger}_{-1,\sigma}c_{0,\sigma} + h.c.) \quad (2.1)$$
$$+\varepsilon_0\sum_{\sigma} n_{0\sigma} + Un_{0\uparrow}n_{0\downarrow},$$

where the operator $c^{\dagger}_{i,\sigma}$ creates a conduction electron on site i with spin $\sigma = \pm 1/2$ and $c^{\dagger}_{0,\sigma}$ creates an electron on the localized state at the site 0 while $n_{0\sigma} = c^{\dagger}_{0,\sigma}c_{0,\sigma}$ is the occupation number of the localized state with spin σ. U is the Coulomb interaction between two electrons of different spins on the localized state and V, V_R and V_L are the hopping integrals between neighboring sites. The parameters V_R and V_L simulate the potential barriers between the impurity site and the left and right reservoirs respectively. In realistic systems, the $i = 0$ site represents a localized state of energy ε_0; the parameters V_R and V_L generally are small as they decrease exponentially with the distance between the localized site and the left or right electrode. This model is very similar to the one-impurity Anderson model with the impurity d orbital replaced by a localized state and the conduction band replaced by left and right Fermi seas. The distinct feature of the model described by the Hamiltonian Eq.2.1 from the one-impurity Anderson model is that the left and right Fermi seas in general may have different chemical potentials so that the out of equilibrium properties of the system can be investigated. Here we will focus on the equilibrium situation. In this case both models are equivalent. We will come back to this question later when we will discuss the value of the occupation number, n_0.

2.2.2 Scattering theory for the Anderson model

2.2.2.a S-matrix

When the size of the conductor is much smaller than the phase-coherence length the transport is coherent and one can calculate the transport properties by solving the Schrödinger equation. Assuming that out of a region of finite size around the impurity, the potential is zero (or negligible), the solutions of the Schrödinger equation are given by plane waves and the transport properties of the conductor can be related to the S-matrix relating the incoming (incident) and outgoing (scattered) plane waves. Thus tunnelling can be viewed as a scattering process, and the problem can be analyzed in terms of elastic scattering of electrons off an impurity. If we denote the spin-σ electron wave functions on the left(and right) side by $u_{k\sigma}^{L(R)}e^{ikx} + v_{k\sigma}^{L(R)}e^{-ikx}$ respectively (see Fig.2.2), one can derive the S-matrix from the expressions of the incoming and outgoing scattering states

$$\begin{pmatrix} u_{k\sigma}^{L} \\ v_{k\sigma}^{R} \end{pmatrix} = \hat{S}_{k\sigma} \begin{pmatrix} v_{k\sigma}^{L} \\ u_{k\sigma}^{R} \end{pmatrix}. \tag{2.2}$$

The S-matrix can be expressed as

$$\hat{S}_{k\sigma} = \mathrm{C}_{\sigma}(\hat{I} - i\hat{T}_{k\sigma}^{res}) \tag{2.3}$$

where C_{σ} is a multiplicative phase factor that will be determined later on, and $\hat{T}_{k\sigma}^{res}$ is the T-matrix in the process of resonant tunnelling the elements of which are given by

$$T_{k\sigma}^{res,\alpha\beta} = 2\pi V_{\alpha}V_{\beta}\rho_{\sigma}(\varepsilon_k)\mathcal{G}_{\sigma}(\varepsilon_k + i\eta), \tag{2.4}$$

$\alpha, \beta = L$ or R, η is a positive infinitesimal, $\rho_{\sigma}(\varepsilon_k)$ is the density of states of conduction electrons with spin σ at energy ε_k, and $\mathcal{G}_{\sigma}(\varepsilon_k + i\eta))$ is the exact retarded Green's function of an electron on the localized state with spin σ and energy ε_k. As defined in Eqs.2.2-2.4 the S-matrix is equivalent to the S-matrix derived by Langreth for the $3D$ Anderson model.

In general the S-matrix which satisfies time-reversal symmetry can be parametrized as

$$\hat{S} = \begin{pmatrix} ie^{i(\theta+\varphi)}\sin\phi & e^{i\theta}\cos\phi \\ e^{i\theta}\cos\phi & ie^{i(\theta-\varphi)}\sin\phi \end{pmatrix} \tag{2.5}$$

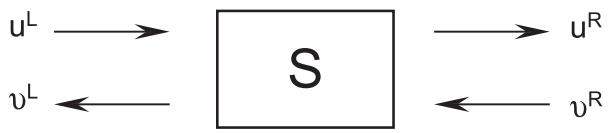

Figure 2.2: Scattering of plane waves. A right-moving arrow corresponds to the plane wave e^{ikx}, a left-moving arrow corresponds to the plane wave e^{-ikx}.

with real phases θ, φ and ϕ. The diagonal matrix elements, $S_{1,1} \equiv S_{LL}$ and $S_{2,2} \equiv S_{RR}$, correspond to the reflection amplitudes for the left and right Fermi seas. In the case of a symmetric (with respect to the reflection $x \to -x$) scattering potential we have $\varphi = 0$. The most important for us is the property shown by the off-diagonal elements, $S_{1,2} \equiv S_{LR}$ and $S_{2,1} \equiv S_{RL}$, which are equal due to time-reversal symmetry, i.e. $S_{LR} = S_{RL}$. As it was shown by Landauer, the linear response conductance is related to the probability of the electron to be transmitted through the scattering region which, in turn, can be expressed in terms of S_{LR}. Moreover, the phase of S_{LR} gives the phase of the outgoing scattered wave as can be seen from the definition of S-matrix in Eq.2.2.

2.2.2.b The Friedel sum rule

Let us consider a system composed of a charged impurity surrounded by a static gas of free (conduction) electrons. Some general properties hold for the stationary states of the electron subsystem. In the present case of a charged impurity, the free electron gas is perturbed by the Coulomb potential created by the impurity. However, it is known that no macroscopic electric field can exist within a metal. So the charge must be screened by the conduction electrons on the atomic scale. Depending on the sign of the charge, Z, the electron gas is either depleted (if $Z < 0$) or accumulated (if $Z > 0$) in the vicinity of the impurity. Generally the effect is more complicated - the charge density shows an oscillating behavior with a decreasing magnitude with distance (schematically represented in Fig.2.3).

The density of states of free electrons is affected by the presence of the impurity. The change in the number of states needed to compensate the charge of the impurity, ΔN, must be equal to the impurity charge Z in order to preserve the charge neutrality of the entire system: $|e|\delta N = Z$. This statement provides the basic idea underlying the Friedel Sum Rule.

We will start with the usual derivation of the Friedel sum rule for the case of the scattering by a potential (for example, by the Coulomb potential created by a charged ion) in the $3D$ case. This type of description corresponds to the case of a free electron gas in a metal containing impurities.

The radial part of the scattering wave functions in the absence of the impurity exhibits the asymptotic behavior of the form

$$R_{lk}(r) \sim \sin(kr - l\pi/2) \text{ for } r \to \infty \tag{2.6}$$

If, for example, we consider a spherical sample of large radius L and impose the boundary condition $\Psi(r = L) = 0$, where $\Psi(r)$ is the total scattering wave function, this leads to a quantization of the wave vector according to

$$k_{nl} = \frac{\pi n}{L} + \frac{l\pi}{2L} \tag{2.7}$$

The electronic density of states per unit of k, is $\rho_l(k) = 1/(k_{n+1} - k_n)$, can then be found

$$\rho_l(k) = \frac{L}{\pi} \tag{2.8}$$

Now let the impurity be located at the center of a sphere. Since the boundary condition is not changed, it follows that the values of k must change. Eq.2.6 in this case takes the following form

$$R_{lk}(r) \sim \sin(kr - l\pi/2 + \delta_l) \text{ for } r \to \infty \tag{2.9}$$

with the new condition of the quantization of the wave vector

$$k'_{nl} = \frac{\pi n}{L} + \frac{l\pi}{2L} - \frac{\delta_l}{L} \tag{2.10}$$

Here we have to take the k-dependence of the phase shift $\delta_l = \delta_l(k)$ into account. We can write

$$\begin{aligned} k'_{n+1}L - \frac{l\pi}{2} + \delta_l(k'_{n+1}) &= (n+1)\pi \,, \\ k'_{n}L - \frac{l\pi}{2} + \delta_l(k'_{n}) &= n\pi \,, \end{aligned} \tag{2.11}$$

which gives

$$(k'_{n+1} - k'_n)\left(L + \frac{d\delta_l}{dk'_n}\right) = \pi \tag{2.12}$$

The density of states per unit of k' is

$$\rho'_l(k) = \frac{1}{\pi}\left(L + \frac{d\delta_l}{dk}\right) \tag{2.13}$$

The first term in the right-hand side of Eq.2.14 corresponds to the electron density of states in the system without impurity. The change in the density of states due to the presence of the impurity is

$$\delta\rho'_l(k) = \frac{1}{\pi}\frac{d\delta_l}{dk} \tag{2.14}$$

It is useful to rewrite this expression in order to obtain the density of states per unit of energy

$$\delta\rho'_l(\omega) = \frac{1}{\pi}\frac{d\delta_l}{d\omega} \tag{2.15}$$

If the summation is carried out over all l values, assuming that for each orbital moment l there are $(2l+1)$ possible values of its projections m_l and that we have two possible spin projections, σ, we obtain the total change in the number of states of energies lower or equal to ϵ

$$\Delta N(\epsilon) = \sum_l \sum_{m_l} \sum_\sigma \int^\epsilon \delta\rho'_l(\omega)d\omega = \frac{2}{\pi}\sum_l (2l+1)\ \delta_l(\epsilon) \tag{2.16}$$

where we have assumed that the phase shift at the bottom of the band is zero. The change in the number of states below the Fermi energy is equal to the change in the number of electrons. Because of the property of electroneutrality, the screening of the impurity by the conduction electrons is total and the latter quantity must be equal to the excess charge brought by the impurity, i.e. to the difference between the impurity ion and that of the ions of the rest of the lattice. Thus, we have

$$Z = \frac{2}{\pi} \sum_{l} (2l+1)\, \delta_l(\epsilon_F) \tag{2.17}$$

This relation is called the Friedel sum rule. If now the impurity is taken as point-like, according to quantum mechanics, it is sufficient to take into account only s-scattering. In the case of spin degeneracy

$$\delta_0(\epsilon_F) = \frac{\pi Z}{2} \tag{2.18}$$

The Friedel sum rule relates the charge of the impurity to the phase shift at the Fermi level.

2.2.2.c The partial Friedel sum rule

It was shown [37],[50] that the Friedel sum rule is applicable for the interacting Anderson model in each spin channel. We will not give here the detailed derivation of this theorem. The derivation makes use of some exact properties of the localized electron retarded Green function. It turns out to be exact in the case of a wide flat conduction band. The letter condition is not necessary. If it is not the case one has to include the contribution of the free electron gas to the charge of the impurity.

The expression of the retarded Green function, $\mathcal{G}_\sigma(\varepsilon)$, in Eq.2.4 generally is unknown. Nevertheless, the use of exact results for the self-energy at $T = 0$ in an interacting Fermi liquid [37, 5] provides us with useful information about $\mathcal{G}_\sigma(\varepsilon)$. At zero temperature only electrons at the Fermi surface, i.e. at $\varepsilon_k = \mu$, are relevant and one can show that

$$n_{0\sigma} = \frac{1}{\pi}\, \mathtt{Im}\, \ln \mathcal{G}_\sigma(\mu + i\eta). \tag{2.19}$$

This relation is known as the generalized Friedel sum rule. The Friedel sum rule which expresses the complete screening of the impurity by conduction electrons (see Fig.2.3) in each spin channel, imposes that $n_{0\sigma}$ is equal to the change in the number of conduction electrons with spin σ resulting from the addition of the impurity, and hence is related to the transmission phase shift δ_σ at the Fermi level, $n_{0\sigma} = \frac{1}{\pi}\delta_\sigma$. Therefore δ_σ coincides with the phase of the Green's function at the Fermi level $\mathcal{G}_\sigma(\mu + i\eta) = |\mathcal{G}_\sigma(\mu + i\eta)|\, e^{i\delta_\sigma}$. If we denote the associated self-energy by $\Sigma_\sigma(\mu + i\eta)$, one gets

$$\mathtt{Im}\, \mathcal{G}_\sigma(\mu + i\eta) = \mathtt{Im}\, [\, \Sigma_\sigma(\mu + i\eta)] \; |\mathcal{G}_\sigma(\mu + i\eta)|^2 \tag{2.20}$$

and finally, since $|\mathcal{G}_\sigma(\mu + i\eta)| = \mathtt{Im}\, \mathcal{G}_\sigma(\mu + i\eta)/\sin\delta_\sigma$, we have

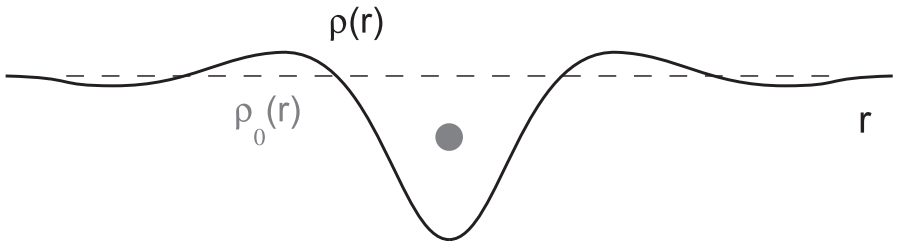

Figure 2.3: Dependence of the charge density (vertical axis) as a function of distance (schematically). Dashed line corresponds to the unperturbed charge density.

$$\mathcal{G}_\sigma(\mu + i\eta)) = \sin\delta_\sigma e^{i\delta_\sigma} / \,\mathtt{Im}\,\Sigma_\sigma(\mu + i\eta). \tag{2.21}$$

Using exact results for the self-energy of a Fermi liquid at Fermi level, $\varepsilon_k = \mu$, and $T = 0$ and considering elastic scattering only, one can show that the only contribution to the imaginary part of self-energy is brought by the hopping terms and one has $\mathtt{Im}\,\Sigma_\sigma(\mu + i\eta) = -\pi(V_L^2 + V_R^2)\rho_\sigma(\mu)$ leading to

$$T_{k_F\sigma}^{res,\alpha\beta} = -2\frac{V_\alpha V_\beta}{(V_L^2 + V_R^2)}\sin\delta_\sigma e^{i\delta_\sigma}. \tag{2.22}$$

Equation (2.22) extends the result obtained by Ng and Lee [50] for the magnitude of the transmission amplitude to the full complex transmission amplitude including the phase factor. In the case of a symmetric quantum dot when $V_L = V_R = V$, one has $\hat{S}_{k_F\sigma} = C_\sigma \hat{S}_{k_F\sigma}^{res}$, where $\hat{S}_{k_F\sigma}^{res}$ is given by

$$\hat{S}_{k_F\sigma}^{res} = e^{i\delta_\sigma}\begin{pmatrix} \cos\delta_\sigma & i\sin\delta_\sigma \\ i\sin\delta_\sigma & \cos\delta_\sigma \end{pmatrix}. \tag{2.23}$$

The multiplicative phase factor C_σ contains additional information about the spectrum and the filling of the quantum dot. To determine it, we will make use of Levinson's theorem[51],[52].

2.2.2.d Levinson's theorem

In its original form, Levinson's theorem applies to the scattering of a particle of angular momentum l by a spherically symmetric potential [51] which falls off sufficiently rapidly at large distances. It relates the zero-energy phase shift δ_l to the number of bound states, N_l^B, of the same angular momentum l supported by the potential

$$\delta_l(k = 0) = \pi N_l^B \tag{2.24}$$

where the phase is defined as usual from the solution of the Schrödinger equation for the radial part of the wave function

$$\left[\frac{d^2}{dx^2} + k^2 + \frac{l(l+1)}{r^2} - U(r)\right] f_l(r) = 0 \tag{2.25}$$

where $f_l(r) \sim \sin(kr - l\pi/2 + \delta(k))$ in the limit $r \to \infty$ and $U(r)$ is the scattering potential. The scattering phase shift, $\delta(k)$, is a continuous function of k with $\delta(k) \to 0$ as $k \to \infty$.

If now we consider the scattering of the particles by a many-body system, such as the collisions of nucleons with light nuclei or of the electrons with atoms, the phase shift does not show any apparent relation to the number of composite bound states, so that the correspondence between the zero-energy phase shift and the number of bound states seems to be lost. The need of a generalization of Levinson's theorem to include spin or non-local potentials was first pointed out by P. Swan [53] in 1955. Of special interest to the problem considered in our work is the extension of Levinson's theorem to the scattering of a particle by a compound system, i.e. for instance by an atom. In a pioneering paper in 1955, Swan relates $\delta_l(0)$ to the number of composite bound states N_l^B of angular momentum $\hbar l$ formed by the incident particle and the atom, *plus* an additional number denoted by N_{Pauli}, equal to the number of states from which the incident particle is excluded by the Pauli principle. Thus the extension of Levinson's theorem to that problem reads:

$$\delta_l(0) = \pi(N_l^B + N_{Pauli}) \tag{2.26}$$

A large number of papers [54],[55] in nuclear physics has then been devoted to this subject and corroborated Swan's statement. One can also find in these papers illustrations of Levinson's theorem for some given examples of the scattering of a particle by an atom (see Table 1 of [53] or Table I of [55]).

In the case of electron-hydrogen scattering, the composite bound state formed by the electron and hydrogen atom can be either a triplet or a singlet spin state (corresponding to antisymmetric or symmetric spatial wave function respectively). In each of the two cases, the phase shift is found to be π. But whereas for the singlet spin state, the value of π arises from the formation of 1 bound state (H^-), the origin of the π value for the phase shift in the triplet spin state is of different nature: even if there is no bound state formed, the number of excluded states equal to 1 in this case still guarantees a value of π for the phase shift. The corresponding triplet state (antisymmetric with respect to spacial coordinates of the incident and target electrons) of H^- is a $1s2s$ state because of the Pauli exclusion principle and it is known to be not found. The excluded state is $1s_\uparrow s_\uparrow$. The $2s$ wave function has an extra node as compared to the $1s$ function Fig.2.4. The scattering of an electron by H at small energies involves the same function inside the potential well range as for an electron forming a virtual state of H^-. Hence an extra loop will give a contribution of π to the zero-energy phase shift $\delta(0)$ without the formation of any bound state. We will keep this example in mind in the following when we will consider the scattering of an electron by a quantum dot.

In the case of a QD which can be viewed as an artificial atom [23, 24, 25, 26, 27, 28] in the configuration $1s$, it follows that $\ln\det \hat{S}_{k_F\sigma}/(2i\pi)$ is equal to the total number of states i.e. $\sum_\sigma n_{0\sigma} = n_0$ in which $n_{0-\sigma}$ is the number of bound states formed by the incident particle and the atom (Kondo singlet state in the Kondo regime), and $n_{0\sigma}$ is the number of states from which the incident particle is excluded by the Pauli principle

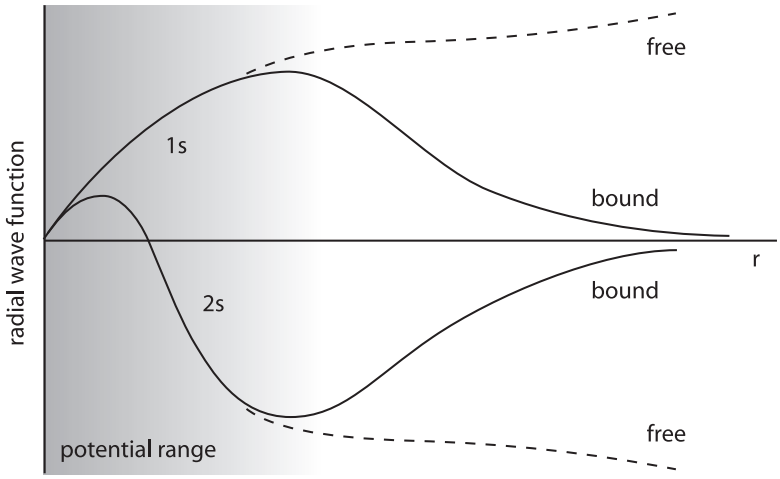

Figure 2.4: Bound and free wave functions for the $1s$ and $2s$ states.

$$\frac{1}{2\pi i}\,\ln\det\hat{S}_{k_F\sigma} = n_0 \tag{2.27}$$

Clearly the latter result disagrees with what can be deduced from Eq.2.23, $\ln\det\hat{S}_{k_F\sigma}/(2i) = \pi n_{0\sigma}$ which is a generalization of the result obtained in Ref.[50]. Our physical understanding of this discrepancy is that the Anderson model fails to capture the full physics describing the experimental device. We believe instead that the quantum dot is more properly described by an artificial atom. We do not intend for the moment to treat the more general problem of the electron scattering by an artificial atom. We propose instead to keep on working with the simplified Anderson model and to capture the extra physical ingredients contained in the artificial atom by introducing a multiplicative phase factor C_σ in front of the S-matrix, Eq.2.3. One can easily check that the so-defined $\hat{S}_{k_F\sigma}$ is still a unitary matrix and that the optical theorem is satisfied: $\hat{T}_{k_F\sigma}\hat{T}^\dagger_{k_F\sigma} = -2\,\mathtt{Im}\,\hat{T}_{k_F\sigma}$, where $\hat{T}_{k_F\sigma} = -i(1-\hat{S}_{k_F\sigma})$. The value of C_σ is determined in order to guarantee extended Levinson's theorem. By applying extended Levinson's theorem, Eq.2.27 to $\hat{S}_{k_F\sigma}$ given by Eq.2.3,

$$\frac{1}{2\pi i}\,\ln\det\hat{S}_{k_F\sigma} = \frac{1}{2\pi i}\,\ln\left\{C_\sigma^2\,e^{2i\delta_\sigma}\right\} \tag{2.28}$$

one finds $\mathrm{C}_\sigma = e^{i\delta_{-\sigma}}$ and

$$\hat{S}_{k_F\sigma} = e^{i\delta}\begin{pmatrix}\cos\delta_\sigma & i\sin\delta_\sigma\\ i\sin\delta_\sigma & \cos\delta_\sigma\end{pmatrix}, \tag{2.29}$$

where $\delta = \sum_\sigma \delta_\sigma$.

According to extended Levinson's theorem, the phase shift counts not only the number of bound states formed by the conduction electron and the scatterer, but also the number of states from which the electrons are excluded by the Pauli principle. As a result, the scattering phase is related to the total occupancy of the quantum dot, i.e. $(n_{0\uparrow} + n_{0\downarrow})$, and our belief is that this is precisely what the quantum interferometry experiments measure.

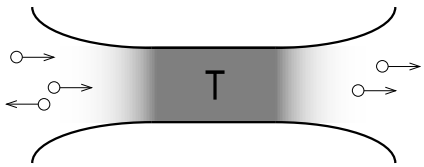

Figure 2.5: The conductance through the scattering region is proportional to the probability for the electron to be transmitted.

2.2.3 Landauer conductance and Aharonov-Bohm effect

2.2.3.a Landauer approach

In the Landauer approach the current through a conductor is expressed in terms of the probability with which an electron can be transmitted through it. This approach has proved to be very useful for the description of mesoscopic transport. To simplify the discussion we consider the zero temperature limit. Then the current is finite in the energy range $\mu_L > \epsilon > \mu_R$ only, where $\mu_{L(R)}$ is the left(right) chemical potential. If one considers the transport properties at equilibrium, $\mu_L \approx \mu_R$, one can assume that the transmission does not depend of energy so that the entire energy range can be viewed as a single energy channel. Under these assumptions the conductance through the mesoscopic device is given by the Landauer formula

$$G = \frac{2e^2}{h} MT \tag{2.30}$$

where T is the transmittance or transmission probability that an electron injected at one end of the conductor is transmitted to the other end. The multiplicative factor M is the number of transverse modes in the conductor. In the case when the transmission probability is different in each channel, one should consider the summation over all the transmitting channels separately. Generally we will assume that $M = 1$. Suppose now that the scattering problem for the conductor can be solved and the outgoing waves are related to the incoming ones by the S-matrix. The transmission probability can then be easily calculated

$$T(\epsilon) = |S_{LR}(\epsilon)|^2 \tag{2.31}$$

where S_{LR} is the off-diagonal element of the S-matrix. In the case of a two-terminal conductor with a single conducting mode we finally have

$$G = \frac{2e^2}{h} T \tag{2.32}$$

where T is given by Eq.2.31. This result has been generalized by Buttiker in the case of multi-terminal conductors.

So the conductance through a mesoscopic conductor depends on the magnitude of the transmission amplitude, $|S_{LR}|$ and not on its phase. So the phase shift can not be deduced from conductance measurements. We will discuss in the following an alternative experimental setup which allows one to determine the phase shift.

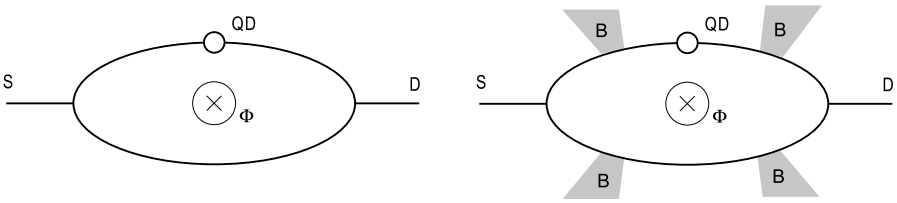

Figure 2.6: Schematic representation of an Aharonov-Bohm interferometer. Electrons injected at the source (S) are collected at the drain (D). The ring of the interferometer consists of two arms: the reference arm and the one in which the quantum dot is imbedded. The closed interferometer (left) is not equivalent to the double slit experiment since it includes multiple traversals of the ring and therefore does not provide access to δ_{QD}. To overcome this difficulty base regions (B) are introduced (right) which collect the back-scattered electrons to ensure that only two forward-propagating paths reach the drain.

2.2.3.b Aharonov-Bohm effect in an open interferometer

In an Aharonov-Bohm interferometry experiment, spin-σ electrons coming from the source through each of the two arms interfere at the drain. When a magnetic flux Φ threads the ring formed by two arms, a possible gauge transformation for the transmission and reflection amplitudes in both arms yields

$$\begin{aligned} t_{ref} &\rightarrow t_{ref}\, e^{i\theta} \\ t_{QD} &\rightarrow t_{QD} \end{aligned} \tag{2.33}$$

where $\theta = 2\pi\Phi/\Phi_0$, is the Aharonov-Bohm phase, and $\Phi_0 = h/e$ is the quantum of magnetic flux. We choose to let the transmission amplitude through the quantum dot unchanged. For the sake of simplicity we assume the transmission amplitude through the reference arm in the absence of magnetic field to be real, $\arg(t_{ref}) = 0$. In general we can also assume the two arms of the interferometer to be geometrically equivalent. The latter assumption is not always satisfied. The geometric difference between the arms may lead to a constant contribution to the phase shift which does not play any role. We also assume the current through the quantum dot to be fully coherent. Moreover, because of its open structure there is no multiple traversals of the ring which is equivalent to a double-slit geometry setup. The source-drain conductance can then be computed using the Landauer formula Eq.2.32

$$G_{AB} = \frac{2e^2}{h}|t_{ref}e^{i\theta} + t_{QD}|^2 \tag{2.34}$$

where the transmission amplitude of the quantum dot is complex $t_{QD} = |t_{QD}|\, e^{i\delta_{QD}}$. One gets

$$G_{AB} = \frac{2e^2}{h}\, t_{ref}^2 + \frac{2e^2}{h}\, |t_{QD}|^2 + \frac{4e^2}{h} t_{ref}|t_{QD}|\, \cos(\theta - \delta_{QD}) \tag{2.35}$$

The first two terms of Eq.2.35 correspond to the conductance of the reference arm and quantum dot respectively. The last term is due to the interference of the electron wave function leading to oscillations of the conductance as a function of the magnetic flux Φ enclosed by the "ring" formed by the two arms. One gets for the periodic conductance oscillations, δG, at the drain

$$\delta G_{AB} = \frac{2e^2}{h} \sum_{\sigma} \cos(2\pi\Phi e/h - \delta_{QD}), \tag{2.36}$$

where we have replaced the factor 2 by the summation over the spin indices.

The periodic AB oscillations are entirely determined by the phase difference between the transmission amplitudes of both arms, i.e. $2\pi\Phi e/h + \delta_{QD}$, where δ_{QD} is the transmission phase shift introduced by the quantum dot. Contrary to the conductance the Aharonov-Bohm current is sensitive to the phase of transmission amplitude, S_{LR}. Thus the interference experiment opens the way to the measurements of the transmission phase shift introduced by (magnetic) impurities.

In practice, the phase shift is measured in the following way. For a given value of the gate voltage V_G applied to the quantum dot (here we consider that all the other voltages, for instance the one controlling the coupling strength to the leads $\Gamma_{L(R)}$ are kept unchanged) the Aharonov-Bohm oscillations of the conductance (or current) are given by $\delta G(B\,; V_G)$ as a function of the magnetic field $\Phi = BS$ (where S is the surface enclosed by the ring, and B is the magnetic field which is assumed to be constant). Then tuning the gate voltage to $V_G + \delta V_G$, the Aharonov-Bohm oscillations are measured again and lead to $\delta G' = \delta G(B\,; V_G + \delta V_G)$. Since the transmission phase shift, δ_{QD}, varies with V_G, the oscillations for $V_G + \delta V_G$ are shifted towards those observed at V_G by an amount of $\delta(\delta V_G) \equiv \delta_{QD}(V_G) - \delta_{QD}(V_G + \delta V_G)$. Then the evolution of a phase shift as the function of V_G can be studied. So even if two arms are not identical geometrically and t_{ref} introduces an additional phase in the oscillations, this one is cancelled in the final and geometric asymmetry does not cause any trouble.

In this work, we neglect the role of the Fano effect on the phase shift considered by some authors [56] and concentrate on the contribution of the quantum dot to the interference pattern.

2.2.3.c Experimental check of the dependence of the conductance with the phase shift

In our approach according to Eq.2.29, δ_{QD} is equal to $\delta = \pi n_0$, and the phase of the AB oscillations measures δ, i.e. the total occupation number n_0 within a multiplicative factor of π. As far as the conductance is concerned, its expression is given by the Landauer formula, $G \propto \sum_\sigma |T^{LR}_{k_F\sigma}|^2$. Using Eq.2.29, $T^{LR}_{k_F\sigma} = i \sin\delta_\sigma e^{i\delta}$, and one has $G \propto \sum_\sigma \sin^2\delta_\sigma$. In the absence of magnetic field, $\delta_\uparrow = \delta_\downarrow = \delta/2$, one gets

$$G \propto \sum_{\sigma} \sin^2 \delta/2. \tag{2.37}$$

The latter result was already obtained by Ng and Lee Ref.[50]. The experimental situation has evolved since then and one now disposes of simultaneous measurements of G

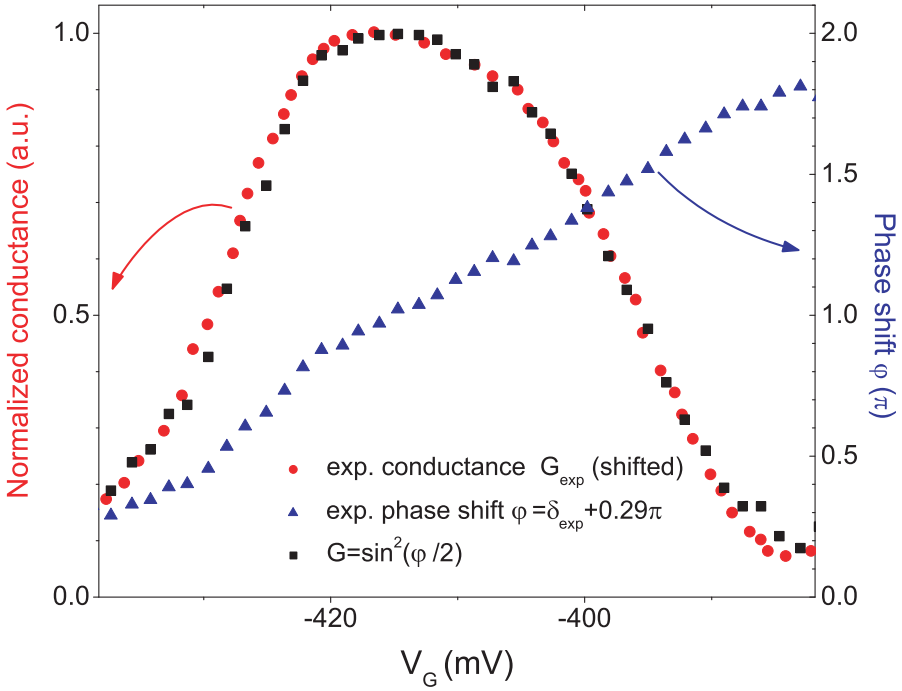

Figure 2.7: Experimental conductance $G_{exp}(V_G)$ (red squares) and phase shift $\Phi(V_G)$ (blue triangles) as a function of the gate voltage V_G (values taken from Ref.[35] incorporating a shift in the V_G-scale for $G_{exp}(V_G)$ evaluated to $\Delta V_G = 15mV$, and a shift in the δ-scale equal to $\Delta\delta = 0.29\pi$). The comparison of the curve $G(V_G) = \sin^2(\Phi(V_G)/2)$ (black squares) with $G_{exp}(V_G)$ (red squares) provides a check to the prediction made in Eq. 2.37.

and δ_{QD}. Our suggestion in this work is to check the theoretical prediction of Eq.2.37 by reporting the experimental results obtained in the unitary limit at different values of the gate voltage, for the conductance G on the one hand, and the phase shift δ_{exp} extracted from the shift of the periodic conductance oscillations on the other hand.

Before examining the experimental test, let us make the following remarks: (i) in an interferometry experiment, only relative values of the transmission phase shifts can be measured since the zero is entirely undetermined. We propose to fix the zero in order to enforce $\delta = \pi$ at the position of the maximum of the visibility, evaluated to $V_G = 423mV$. This implies a shift in the δ-scale evaluated to $\Delta\delta = 0.29\pi$ with $\phi = \delta + \Delta\delta$; (ii) typically the measurement of the conductance G is performed in an "one-arm" device (pinching off the reference arm with the barrier gate) while that of the phase shift or visibility is done in a "two-arm" device as realized in an AB interferometer. Provided that the transport is coherent, the evolution of the visibility with the gate voltage is known to mimic that of the conductance. Yet getting both dependences closer, shows that the passage from an "one-arm" to a "two-arm" experiment introduces a shift in the gate voltage scale. We evaluate this shift to be $\Delta V_G = 15mV$, Fig.2.8. To be consistent with, we then take the values of G at $(V_G - \Delta V_G)$, and of δ at V_G; (iii) lastly the conductance is normalized by its maximum value at $V_G = 423mV$. Taking all these

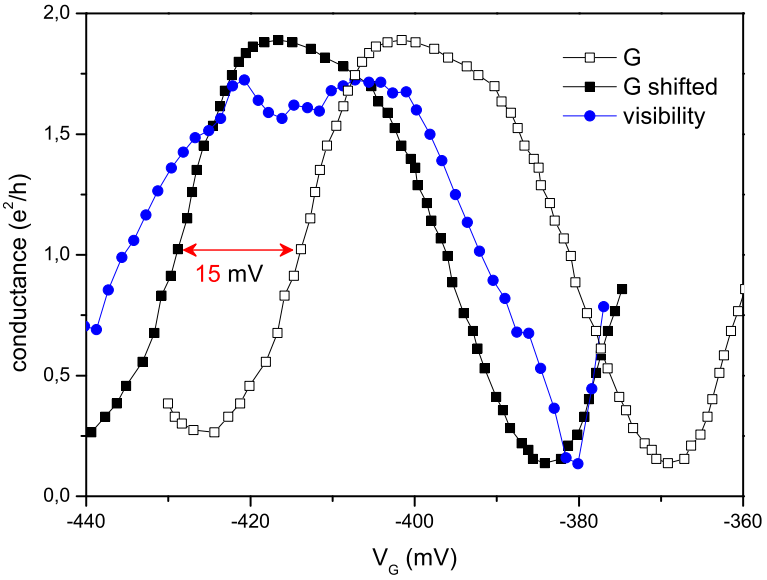

Figure 2.8: V_G-dependence of both the conductance, G, of the quantum dot measured in an "one-arm" experiment and the visibility measured in a "two-arm" experiment [35]. The comparison of these 2 curves let a shift appear δV_G of the order of 15 mV.

points into account, the result of the test is reported in Fig.2.7. One can see from the graph that the experimental dependence of $\sin^2 \delta/2$ with the gate voltage reproduces that of the "shifted" conductance G_{exp} in a quite remarkable way. The latter experimental test brings further support to the validity of Eqs.(2.36-2.37) with $\delta_{QD} = \delta$. A shifted conductance $G(V_G - \delta V_G)$ is deduced as a function of V_G (used in Fig.2.8).

2.2.4 Scattering phase shift

2.2.4.a Diagonalization of the hamiltonian of the Anderson model with two reservoirs

As discussed previously, according to the Friedel sum rule, the transmission phase shift δ is given by the occupation number n_0 of the localized state within a multiplicative factor of π. Following Eq.(2.1), the system is described by a Anderson model with two reservoirs, left and right. An important step has been got over by Glazman and Raikh[49] by diagonalizing the starting hamiltonian. It is easier to work with the Anderson hamiltonian written in the momentum representation

$$H = \sum_{k\sigma} \varepsilon_k c^\dagger_{k\sigma L} c_{k\sigma L} + \sum_{k\sigma} \varepsilon_k c^\dagger_{k\sigma R} c_{k\sigma R} + \varepsilon_0 \sum_\sigma d^\dagger_\sigma d_\sigma + U n_{0\uparrow} n_{0\downarrow} + \sum_{k\sigma} \left(V_L c^\dagger_{k\sigma L}\, d_\sigma + h.c. \right) + \sum_{k\sigma} \left(V_R c^\dagger_{k\sigma R}\, d_\sigma + h.c. \right) \tag{2.38}$$

where $c^\dagger_{k\sigma L}$, $c^\dagger_{k\sigma R}$ and $d^\dagger$ are operators which create an electron in a state with momentum k and spin σ in the left and right reservoirs and at the impurity site respectively; $n_{0\sigma} = d^\dagger_\sigma d_\sigma$ is the particle operator at the impurity site. One can express the Hamiltonian defined in Eq.2.38 in terms of quasiparticle creation operators

$$\begin{aligned} \alpha^\dagger_{k\sigma} &= u\, c^\dagger_{k\sigma L} + v\, c^\dagger_{k\sigma R} \\ \beta^\dagger_{k\sigma} &= u\, c^\dagger_{k\sigma R} - v\, c^\dagger_{k\sigma L} \end{aligned} \tag{2.39}$$

which are symmetrized and antisymmetrized combinations of the initial "left" and "right" reservoir creation operators. The parameters of the Bogoliubov transformation are given by

$$\begin{aligned} u &= V_L/V \\ v &= V_R/V \\ V &= \sqrt{|V_L|^2 + |V_R|^2} \end{aligned} \tag{2.40}$$

it is easy to see that the hamiltonian take the following diagonal form

$$H = \sum_{k\sigma} \varepsilon_k \alpha^\dagger_{k\sigma} \alpha_{k\sigma} + \varepsilon_0 \sum_\sigma d^\dagger_\sigma d_\sigma + U n_{0\uparrow} n_{0\downarrow} + V \sum_{k\sigma} \left(\alpha^\dagger_{k\sigma}\, d_\sigma + d^\dagger_\sigma\, \alpha_{k\sigma} \right) + \sum_{k\sigma} \varepsilon_k \beta^\dagger_{k\sigma} \beta_{k\sigma} \tag{2.41}$$

One can see from Eq.2.39, only one type of states is hybridized to the localized state whereas the other one is fully decoupled from it. Therefore the system is described by a Anderson model with a single reservoir and a hybridization potential $\widetilde{V} = \sqrt{V_L^2 + V_R^2}$, equal to $V\sqrt{2}$ in the case of a symmetric quantum dot when $V_L = V_R = V$. This property of the two-reservoir Anderson model shows that the problem of calculating, for example, the tunnelling transparency can be reduced to the well-known problem of conductivity of a metal. Thus in the case of interest of a quantum dot connected to two reservoirs of electrons (see Fig.2.1) the transparency of barrier will increase under the same condition as when the Kondo effect manifest itself in bulk metals.

2.2.4.b Solution of the Anderson model

As it is known, the Anderson model is integrable and an exact solution exists based on the use of the Bethe ansatz [17],[15]. The occupation number n_0 can be derived by

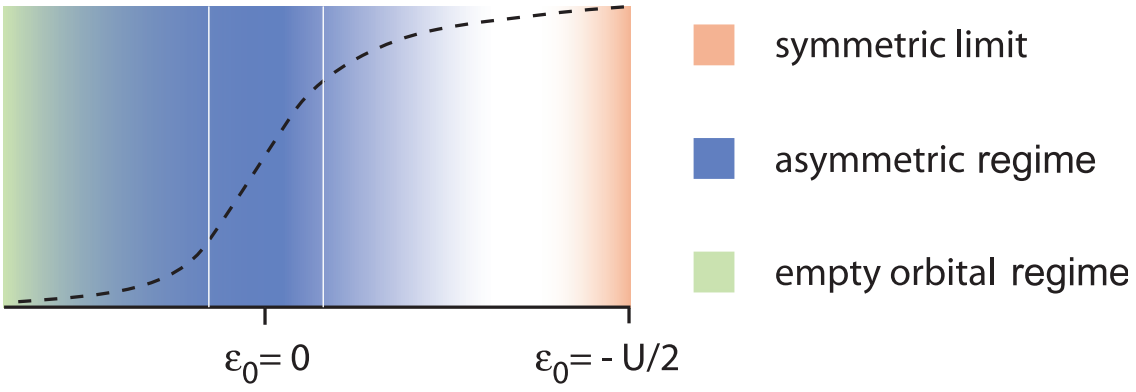

Figure 2.9: Different regimes of the Anderson model in the "weak" coupling regime $\Gamma \ll U$. The dashed line corresponds to the occupation number (schematic). The symmetric limit correspond to values of ε_0 such that $(U + 2\varepsilon_0) \ll \sqrt{U\Gamma}$. Detailed calculations show that in this limit $n_0 = 1$ and the deviation at $\varepsilon_0 + U/2 \sim \sqrt{U\Gamma}$ is estimated to $1-n_0 \sim (\Gamma/U)^{3/2}$. The asymmetric limit corresponds to $(U+2\varepsilon_0) \gg \sqrt{U\Gamma}$. In the weak coupling regime, $\Gamma \ll U$, and in the intermediate valence regime $|\varepsilon_0| \ll U$ (represented by two white vertical lines), n_0 exhibits a universal behavior as a function of ε_0^* (Eq.2.42). At $\varepsilon_0^* = 0$ the occupation number takes the universal value $n_0 = 2-\sqrt{2}$. The empty orbital regime is obtained when $n_0 \to 0$.

solving a system of integral equations. We have solved the equations of the Bethe ansatz (B.A.) numerically at $T = 0$ (integral equations [2a-2b-4a-4b] of Ref.[57]). This allows us to determine the value of n_0 as a function of the parameters of the Anderson model ε_0, V and U.

It turns out that the three parameters, ε_0, V and U, do not affect the results of the B.A. calculations in a separate way but only via their combined ratios ε_0/U and Γ/U, where $\Gamma = \pi V^2 \rho_0$ is the width of the virtual bound state and ρ_0 is the bare density of states of conduction electrons at the Fermi level.

Let us then denote by $n_0(\varepsilon_0, \Gamma/U)$ the value of the localized state occupation number for the corresponding values of the parameters. Due to the particle-hole symmetry of the model (Eq.(3.6) of [58]), the following relation stands: $n_d(-(\varepsilon_0 + U), \Gamma/U) = 2 - n_d(\varepsilon_0, \Gamma/U)$. This automatically ensures the occupation number in the symmetric limit $\varepsilon_0 = -U/2$ to be equal to 1, i.e. $n_d(-U/2, \Gamma/U) = 1$ whatever Γ/U is. Furthermore it follows from the preceding relation that the study can be restricted to $-U/2 \leq \varepsilon_0 \leq U/2$, since the results for $-U/2 \geq \varepsilon_0 \geq -3U/2$ can easily be derived from them. The results of the calculations are reported in Fig.2.10(a) showing the dependence of n_0 as a function of the normalized energy $-(\varepsilon_0/U + 1/2)$ at different values of Γ/U. For large coupling strengths $\Gamma/U \geq 0.25$, we have checked that the variation of n_0 with ε_0 obeys the Breit-Wigner formula associated with the formation of a virtual bound state, i.e. $n_0 = 1 - \frac{2}{\pi}\arctan(\widetilde{\varepsilon_0}/\Gamma)$ in which $\widetilde{\varepsilon_0}$ is the renormalized energy of the localized state. Oppositely for weak coupling strengths $\Gamma/U \leq 0.25$, the energy dependence of n_0 exhibits a plateau around the symmetric limit $\varepsilon_0 = -U/2$. This plateau is the direct manifestation of the Kondo resonance formed at the Fermi level. The latter feature can

be viewed as the beginnings of the "staircase" variation of n_0 with ε_0 that is reached in the localized regime $\Gamma/U \to 0$.

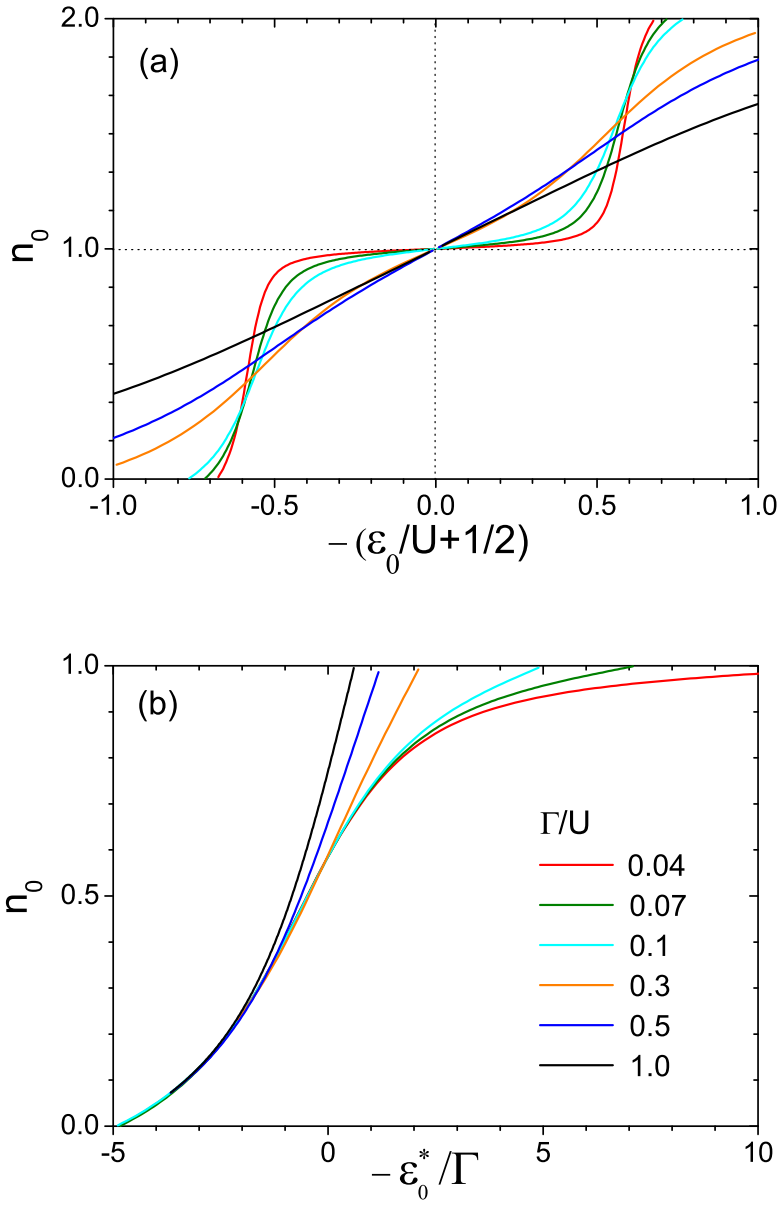

Figure 2.10: (a) Occupation number n_0 as a function of the normalized energy $(-\varepsilon_0/U + 1/2)$ of the localized state for the Anderson model at different values of Γ/U where $\Gamma = \pi V^2 \rho_0(E_F)$. Note that $n_0 = 1$ at the symmetric limit $\varepsilon_0 = -U/2$. Let us also remark the presence of a plateau in the vicinity of the symmetric limit in the weak coupling regime $\Gamma/U \leq 0.25$ resulting from the formation of the Kondo resonance at the Fermi level; (b) The same quantity as a function of renormalized energy $-\varepsilon_0^*/\Gamma = -\varepsilon_0/\Gamma - 1/\pi \ln(\alpha U/\Gamma)$ (with $\alpha = \pi e/4$) at different values of Γ/U. Note the existence of a universal behavior in the asymmetric regime when $\Gamma/U \leq 0.25$.

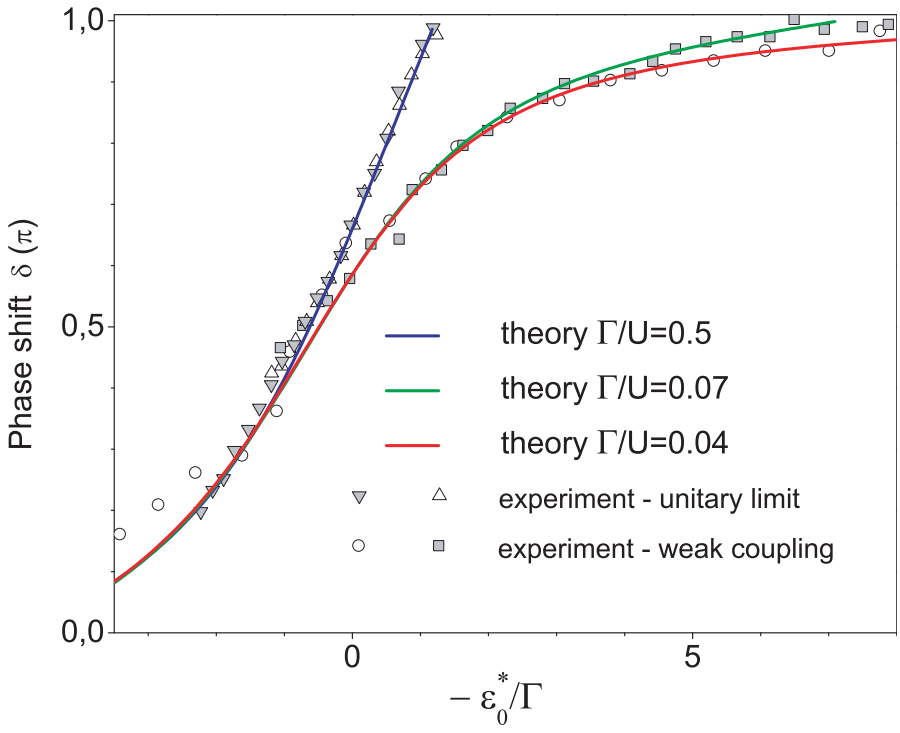

Figure 2.11: Fit of the experimental data on the gate voltage dependence of the phase shift with the theoretical results on $\delta = \pi n_0$ as a function of $-\varepsilon_0^*/\Gamma$. Making use of the electron-hole symmetry, the experimental results obtained above the symmetric limit are reported in the same scale as those obtained below it. They are represented by triangles pointing down and up respectively in the unitary limit, and by squares and circles respectively in the weak-coupling regime. The values are extracted from ref.[35] adding a shift in the δ-scale equal to 0.29π and 0.01π in the unitary limit and weak-coupling regimes respectively. The best fit is obtained for $\Gamma/U = 0.5$ in the unitary limit both below and above the symmetric limit, and for $\Gamma/U = 0.07$ or 0.05 in the weak-coupling regime depending whether the experimental results below or above the symmetric limit respectively are considered.

Therefore one disposes of two parameters, Γ/U and ε_0/U, to fit the experimental data. The value of ε_0 is governed by the strength of the gate voltage V_G. As usual, we consider a linear correspondence between both quantities. In order to help us finding the best fitting parameter Γ/U, we propose to take advantage of a result pointed out by Haldane [59] according to which the physical quantities observed in the asymmetric regime of the Anderson model are universal functions of the renormalized energy

$$\varepsilon_0^*/\Gamma = \varepsilon_0/\Gamma + 1/\pi \ln(\alpha U/\Gamma) \tag{2.42}$$

where $\alpha = \pi e/4$. In Fig.2.10(b), we have plotted the results of our calculation for n_0 as a function of $-\varepsilon_0^*/\Gamma$. In the asymmetric regime when $(U + 2\varepsilon_0) \gg \sqrt{\Gamma U}$ and $|\varepsilon_0| \ll U$ (intermediate valence region), the behavior of n_0 as a function of $-\varepsilon_0^*$ is universal as it is observed in Fig.2.10(b). The universality is reached when $\Gamma/U \leq 0.25$ and the validity

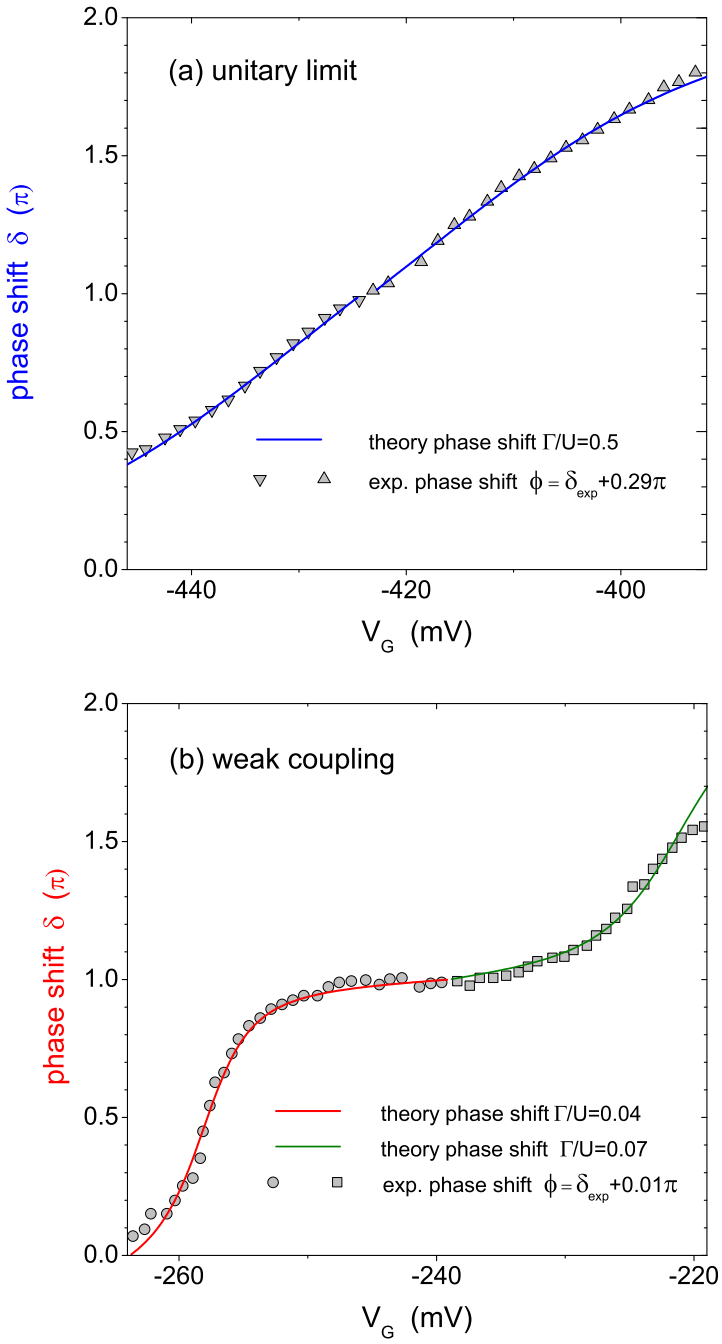

Figure 2.12: Phase shift as a function of the gate voltage V_G. (a) unitary limit. Theoretical results from Bethe ansatz calculations at $\Gamma/U = 0.5$ (blue line) compared to the experimental data for $\Phi/\pi = \delta_{exp}/\pi + 0.29$ represented by triangles pointing up and down successively; (b) weak-coupling regime. Theoretical results from Bethe ansatz calculations at $\Gamma/U = 0.07$ and 0.04 (red and green lines respectively) compared to the experimental data for $\Phi/\pi = \delta_{exp}/\pi + 0.01$ represented by circles and squares successively.

of the universal behavior holds along the range $|\varepsilon_0^*/\Gamma - 1/\pi \ln(\alpha U/\Gamma)| \ll U/\Gamma$. The domain of universality shrinks when Γ/U increases until vanishing when $\Gamma/U \geq 0.25$. As a general result, $\varepsilon_0^* = 0$ belongs to the domain of universality and $n_0(\varepsilon_0^* = 0, \Gamma/U \ll 0.25) = 2-\sqrt{2}$. Lastly one can see that in the limit $n_0 \to 0$, the curves $n_0 = f(\varepsilon_0^*/\Gamma, \Gamma/U)$ at various values of Γ/U, lie on top of each other displaying an asymptotic behavior. This can be proved by noticing that in the expression of $n_0(-\varepsilon_0^*/\Gamma)$ resulting from the Breit-Wigner formula the renormalization of Γ is negligible in the $n_0 \to 0$ limit. The existence of both these universal and asymptotic behaviors is of the valuable help in fitting the experimental data. Fig.2.12 reports the results of the fit in comparison with the experimental data available for the unitary limit and weak coupling regimes.

The experimental results incorporates a shift in the δ-scale, $\Phi = \delta + \Delta\delta$ in order to get $\Phi = \pi$ at the symmetric limit (signaled either by a maximum or a dip in the visibility as a function of V_G in each of the two regimes considered). One gets $\Delta\delta = O.29\pi$ and 0.01π respectively. The best fit is obtained for $\Gamma/U = 0.5$ in the unitary limit both below and above the symmetric limit, and for $\Gamma/U = 0.07$ or 0.05 in the weak coupling strength regime depending whether one considers the regime below or above the symmetric limit. Finally we go back to the variation of δ with $(-\varepsilon_0/U + 1/2)$ at the values of Γ/U defined just above, and fit the experimental data $\Phi(V_G)$ with them. Once having the x-scales translated in order to let the symmetric limit $\delta = \pi$ coincide, the last thing that we have to do is to fix the $\varepsilon_0/U \leftrightarrow V_G$ correspondence. The best choice in both regimes considered is obtained for $\Delta V_G/\Delta(\varepsilon_0/U) = 32mV$. As can been seen from Fig.2.12, our theoretical predictions are in remarkable quantitative agreement with the experimental data. The fit is all the more remarkable that it is done in presence of a single fitting parameter Γ/U that we have adjusted by taking benefit of the existence of a universal behavior in the asymmetric regime.

2.3 Conclusion

In conclusion, we have proposed a theoretical analysis of the transmission phase shift of a quantum dot in the presence of Kondo correlations and confronted our results to the Aharonov-Bohm interferometry and conductance measurements. We have shown the presence of a factor of 2 of difference between the total phase of the S-matrix (responsible for the shift in the A-B oscillations), and the one appearing in the expression of the conductance $G \sim \sin^2(\delta/2)$ implying a partial phase shift per spin. Our calculations based on Bethe ansatz combined with the use of the Friedel sum rule lead to a remarkable quantitative agreement with experimental results. The whole discussion so far has been restricted to the low temperature limit. One of the upcoming goals will be to include finite temperature effects as well as to study the influence of a magnetic field. It will also be interesting in the future to investigate the out-of-equilibrium situation. The analysis of these questions requires some special techniques and will be discussed in Chapter 4.

Theoretical Analysis of the Transmission Phase Shift of a Quantum Dot in the Presence of Kondo Correlations

A. Jerez,[1,2] P. Vitushinsky,[3] and M. Lavagna[3,*]

[1]European Synchrotron Radiation Facility, 6, rue Jules Horowitz, 38043 Grenoble Cedex 9, France
[2]Institut Laue Langevin, 6, rue Jules Horowitz, 38042 Grenoble Cedex 9, France
[3]Commissariat à l'Energie Atomique, DRFMC/SPSMS, 17, rue des Martyrs, 38054 Grenoble Cedex 9, France

(Received 10 March 2005; published 14 September 2005)

We study the effects of Kondo correlations on the transmission phase shift of a quantum dot coupled to two leads in comparison with the experimental determinations made by Aharonov-Bohm (AB) quantum interferometry. We propose here a theoretical interpretation of these results based on scattering theory combined with Bethe ansatz calculations. We show that there is a factor of 2 difference between the phase of the S-matrix responsible for the shift in the AB oscillations and the one controlling the conductance. Quantitative agreement is obtained with experimental results for two different values of the coupling to the leads.

DOI: 10.1103/PhysRevLett.95.127203 PACS numbers: 75.20.Hr, 72.15.Qm, 73.21.La, 73.23.Hk

Quantum dots (QD), small puddles of electrons connected to leads, can be obtained in a controlled fashion because of recent progress in nanolithography. Under certain conditions a dot can be modeled as a localized spin coupled to Fermi baths (the leads). A Kondo effect takes place [1–3] when the temperature is lowered. A key ingredient of the Kondo effect is the phase shift δ an electron undergoes when it crosses the dot. While its direct measurement was out of scope in bulk systems, it became feasible recently in quantum dots via Aharonov-Bohm (AB) interferometery [4]. We mention here the experimental results obtained in two cases corresponding to a strong coupling to the leads [4,5]. In the unitary limit, the phase shift climbs almost linearly with V_G with a value at the middle of the Kondo enhanced valley which is almost π. At a smaller value of the coupling strength, the phase shift develops a wide plateau at almost π. We call the latter case the "Kondo regime." Early theoretical work on the phase shift for the bulk Kondo effect [6,7] predicts $\delta = \pi/2$. In the context of QD, Gerland *et al.* [8] had obtained, on the basis of numerical renormalization group and Bethe ansatz calculations, a variation of δ with the energy of the localized state leading to a value of $\pi/2$ in the symmetric limit, in disagreement with the recent experimental results quoted above [4,5]. In this Letter, we propose a new theoretical interpretation of the experimental results based on scattering theory and Bethe ansatz calculations. Our main prediction concerns a factor of 2 difference found between the phase of the S matrix observed by the phase shift measurements and the phase governing the conductance.

Let us consider a quantum dot coupled via tunnel barriers to two leads L and R, and capacitively to a gate maintained at the voltage V_G. The system can be described [9,10] by a one-dimensional Anderson model with two reservoirs L and R,

$$H = -t\sum_{\sigma}\Big[\sum_{i\geq 1}(c^{\dagger}_{i,\sigma}c_{i+1,\sigma} + \text{H.c.}) + \sum_{i\leq -2}(c^{\dagger}_{i,\sigma}c_{i+1,\sigma} + \text{H.c.})\Big] - V_R\sum_{\sigma}(c^{\dagger}_{0,\sigma}c_{1,\sigma} + \text{H.c.}) - V_L\sum_{\sigma}(c^{\dagger}_{-1,\sigma}c_{0,\sigma} + \text{H.c.}) + \varepsilon_0\sum_{\sigma}n_{0\sigma} + Un_{0\uparrow}n_{0\downarrow}, \quad (1)$$

Consider the elastic component of the S matrix, $\hat{S}_{k\sigma}$, describing the scattering of a spin-σ electron with momentum k off the impurity. It is given by [6,10,11] $\hat{S}_{k\sigma} = \mathrm{C}_{\sigma}(\hat{I} - i\hat{T}^{\mathrm{res}}_{k\sigma})$, where C_{σ} is a multiplicative phase factor and $\hat{T}^{\mathrm{res}}_{k\sigma}$ is the T matrix with matrix elements given by

$$T^{\mathrm{res},\alpha\beta}_{k\sigma} = 2\pi V_{\alpha}V_{\beta}\rho_{\sigma}(\varepsilon_k)\mathcal{G}_{\sigma}(\varepsilon_k + i\eta), \quad (2)$$

where $\alpha, \beta = L$ or R, $\rho_{\sigma}(\varepsilon_k)$ is the density of states of conduction electrons for σ and ε_k, and $\mathcal{G}_{\sigma}(\varepsilon_k + i\eta)$ is the exact localized electron retarded Green's function. Using exact results [6,12] on the self-energy at $T = 0$ in an interacting Fermi liquid, one can show that $n_{0\sigma} = \frac{1}{\pi}\,\mathrm{Im}\,\ln\mathcal{G}_{\sigma}(\mu + i\eta)$. Friedel's sum rule [12,13] requires $n_{0\sigma}$ to be equal to the change in the number of conduction electrons with spin σ resulting from the addition of the impurity. Hence it is related to the transmission phase shift δ_{σ} at the Fermi level, $n_{0\sigma} = \frac{1}{\pi}\delta_{\sigma}$. Therefore δ_{σ} coincides with the phase of the Green's function at the Fermi level $\mathcal{G}_{\sigma}(\mu + i\eta)$. If we denote the associated self-energy by $\sum_{\sigma}(\mu + i\eta)$, one gets $\mathcal{G}_{\sigma}(\mu + i\eta) = \sin\delta_{\sigma}e^{i\delta_{\sigma}}/\mathrm{Im}\Sigma_{\sigma}(\mu + i\eta)$. with $\mathrm{Im}\Sigma_{\sigma}(\mu + i\eta) = -\pi(V_L^2 + V_R^2)\times\rho_{\sigma}(\mu)$ [6,12] at $T = 0$ leading to

$$T^{\mathrm{res},\alpha\beta}_{k_F\sigma} = -2\frac{V_{\alpha}V_{\beta}}{(V_L^2 + V_R^2)}\sin\delta_{\sigma}e^{i\delta_{\sigma}}. \quad (3)$$

In the case of a symmetric QD with $V_L = V_R = V$, one has

$S^{LR}_{k_F\sigma} = S^{RL}_{k_F\sigma} = C_\sigma i \sin\delta_\sigma e^{i\delta_\sigma}$ and $S^{LL}_{k_F\sigma} = S^{RR}_{k_F\sigma} = C_\sigma \times \cos\delta_\sigma e^{i\delta_\sigma}$. The multiplicative phase factor C_σ contains additional information about the spectrum and the filling of the quantum dot. To determine it, we make use of Levinson's theorem [14,15]. In its original form, the theorem applies to the potential scattering of a particle in a given momentum l and relates the zero-energy phase shift δ_l to the number of bound states of the same l supported by the potential. It was generalized [16,17] later on to the case of the scattering of a particle by a neutral compound system as constituted, for instance, by an atom. In the present case of a QD, which can be viewed as an artificial atom, it follows that $\ln \det \hat{S}_{k_F\sigma}/(2i\pi)$ is equal to the total number of states, i.e., $\sum_\sigma n_{0\sigma} = n_0$. By applying generalized Levinson's theorem to $\hat{S}_{k_F\sigma}$, one finds $C_\sigma = e^{i\delta_{-\sigma}}$ and

$$\hat{S}_{k_F\sigma} = e^{i\delta}\begin{pmatrix} \cos\delta_\sigma & i\sin\delta_\sigma \\ i\sin\delta_\sigma & \cos\delta_\sigma \end{pmatrix}, \tag{4}$$

where $\delta = \sum_\sigma \delta_\sigma$. One can easily check that, $\hat{S}_{k_F\sigma}$ being a unitary matrix, the optical theorem is fulfilled: $\hat{T}_{k_F\sigma}\hat{T}^\dagger_{k_F\sigma} = -2\,\mathrm{Im}\hat{T}_{k_F\sigma}$, where $\hat{T}_{k_F\sigma} = -i(\hat{I} - \hat{S}_{k_F\sigma})$.

In an open Aharonov-Bohm interferometry experiment [5], spin-σ electrons coming from the source through each of the two arms interfere coherently at the drain, leading to periodic oscillations of the differential conductance, the argument of which is given by $2\pi\Phi e/h + \delta_{\mathrm{QD}}$. Φ is the magnetic flux and δ_{QD} is the transmission phase shift introduced by the QD, equal to $\delta = \pi n_0$ [cf. Eq. (4)]. In this Letter, we neglect the role of the reference arm on the phase shift considered by some authors [18] and concentrate on the contribution of the quantum dot to the interference pattern. The conductance through the QD is expressed by the Landauer formula [19,20], $G \propto \sum_\sigma |T^{LR}_{k_F\sigma}|^2$. Using Eq. (4), we get $G \propto \sum_\sigma \sin^2\delta_\sigma$. In the absence of magnetic field, $\delta_\uparrow = \delta_\downarrow = \delta/2$, one gets

$$G \propto \sum_\sigma \sin^2\delta/2. \tag{5}$$

Because of recent developments in experimental techniques, one now disposes of simultaneous measurements of G and δ_{QD}. In this Letter we check the validity of the theoretical prediction of Eqs. (4) and (5) by reporting the experimental results for G and δ_{QD} obtained in the unitary limit at different values of V_G. Before examining the experimental test, we make the following remarks: (i) in an interferometry experiment, only relative values of the transmission phase shifts can be measured. Hence we set $\delta = \pi$ at the location of the maximum of the visibility, evaluated to $V_G = 423$ mV. This implies a shift in the δ scale evaluated to $\Delta\delta = 0.29\pi$ with $\varphi = \delta + \Delta\delta$; (ii) typically the measurement of the conductance G is performed in a "one-arm" device (pinching off the reference arm with the barrier gate), whereas that of the visibility is done in a "two-arm" device. As a result, while the evolution of the visibility with V_G mimics that of the conductance, the value of the former is shifted with respect to that of the latter, by $\Delta V_G = 15$ mV. Therefore we take the values of G at $(V_G - \Delta V_G)$, and of δ at V_G; (iii) the conductance is normalized by its maximum value at $V_G = 423$ mV. Taking all these points into account, the graph reported in Fig. 1 shows that the experimental dependence of $\sin^2\varphi/2$ with V_G reproduces that of the "shifted" conductance G_{exp} in a quite remarkable way, providing further support to the validity of Eqs. (4) and (5) [21].

We now want to evaluate n_0 in order to derive $\delta = \pi n_0$. Starting from Eq. (1), one can show [9] that only the symmetric linear combination of electrons couples to the localized state. Therefore if we are interested only in n_0, it is sufficient to study a single reservoir Anderson model with a hybridization potential $\tilde{V} = \sqrt{V_L^2 + V_R^2}$. We have solved the equations of the Bethe ansatz (BA) numerically at $T = 0$ [22–24]. This allows us to determine the value of n_0 as a function of the parameters of the Anderson model ε_0, V, and U. The three parameters enter through their ratios ε_0/U and Γ/U, where $\Gamma = \pi V^2\rho_0$. Denote by $n_0(\varepsilon_0, \Gamma/U)$ the value of n_0 for the corresponding values of the parameters. The following relation holds due to the particle-hole symmetry of the model [23]: $n_0(-(\varepsilon_0 + U), \Gamma/U) = 2 - n_0(\varepsilon_0, \Gamma/U)$. This automatically ensures $n_0(-U/2, \Gamma/U) = 1$ in the symmetric limit $\varepsilon_0 = -U/2$ whatever Γ/U is. Furthermore, it follows from the preceding relation that the study can be restricted to $-U/2 \le \varepsilon_0 \le U/2$ and the remaining part can be deduced from it. The results of the calculations are reported in Fig. 2(a). For strong coupling strengths $\Gamma/U \ge 0.25$, n_0 is found to climb almost linearly with $-(\varepsilon_0/U + 1/2)$, whereas for weak coupling strengths $\Gamma/U \le 0.25$, the energy dependence of n_0 develops a plateau around $\varepsilon_0 = -U/2$. This

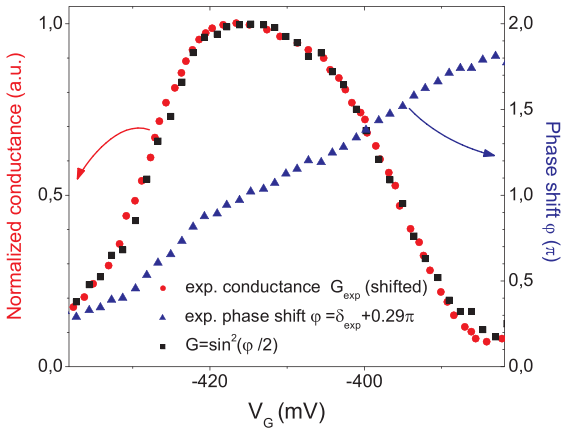

FIG. 1 (color online). Experimental conductance $G_{\mathrm{exp}}(V_G)$ and phase shift $\varphi(V_G)$ as a function of V_G (values taken from Ref. [4]; cf. text). Comparison is made with the curve $G(V_G) = \sin^2[\varphi(V_G)/2]$.

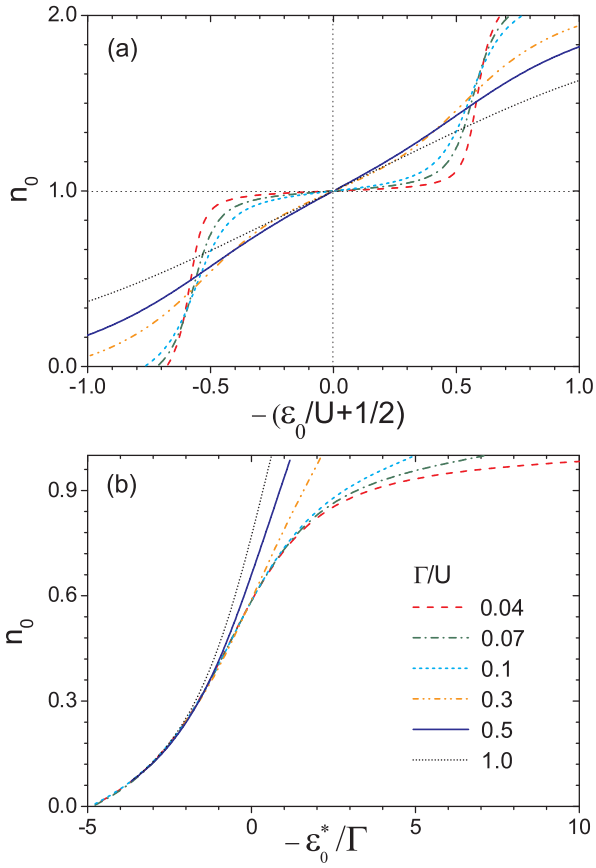

FIG. 2 (color online). (a) Theoretical results from the BA calculations for the occupation number n_0 as a function of the normalized energy $(-\varepsilon_0/U + 1/2)$ at different values of Γ/U. Note that $n_0 = 1$ at the symmetric limit $\varepsilon_0 = -U/2$ and the existence of a plateau in its vicinity when $\Gamma/U \leq 0.25$. (b) The same quantity as a function of the renormalized energy ε^*/Γ at different values of Γ/U.

change of behavior is due to the fact that the extent of the local moment regime (centered around $\epsilon_0 = -U/2$ with $n_0 \simeq 1$) increases when Γ/U decreases. As the temperature is lowered, the Kondo resonance develops through this local moment regime. This plateaulike structure can be viewed as the beginnings of the "staircase" variation of n_0 with ε_0 obtained in the localized regime $\Gamma/U \to 0$.

The experimental data can be fitted then with two parameters, Γ/U and ε_0/U. The value of ε_0 is governed by the strength of the gate voltage. Fitting the experimental data from results presented in Fig. 2(a) is a difficult task since one needs to fix the correspondence between ε_0/U and V_G on the one hand (we take it linear as usual, independent of the regime considered), and to find the best fitting value for Γ/U in the different regimes on the other hand. A valuable help for doing this is provided by taking advantage of some special properties of the Anderson model. These properties can easily be recognized when physical quantities such as n_0 are plotted as a function of some renormalized energy defined as $\varepsilon^*/\Gamma = \varepsilon_0/\Gamma + g(U/\Gamma)$. In the asymmetric regime [24] when $(U + 2\varepsilon_0) \gg \sqrt{\Gamma U}$ and $|\varepsilon_0| \ll U$, $g[U/\Gamma]$ equals $\frac{1}{\pi} \times \ln(\pi e U/(4\Gamma))$ and the behavior of n_0 as a function of $-\varepsilon_0^*/\Gamma$ is universal [24,25]. This property is illustrated in Fig. 2(b). The universality is reached when $\Gamma/U \leq 0.25$ and the range of energy over which universal behavior extends is given by $|\varepsilon_0^*/\Gamma - 1/\pi \ln(\alpha U/\Gamma)| \ll U/\Gamma$. One can also see from Fig. 2(b) that in the empty level regime ($n_0 \to 0$), the curves $n_0 = f(\varepsilon_0^*/\Gamma, \Gamma/U)$ at various values of Γ/U merge, displaying an asymptotic behavior [26]. The existence of both these universal and asymptotic behaviors is of valuable help in fitting the experimental data. Figure 3 reports the results of the fit in the unitary limit and Kondo regimes. The experimental results incorporate a shift in the δ scale, $\varphi = \delta + \Delta\delta$ in order to get $\varphi = \pi$ at the symmetric limit. We establish the correspondence between V_G and ε_0/U by fitting the experimental data to the theoretical results in the empty level regime when all the curves merge. One finds $\Delta V_G/\Delta(\varepsilon_0/U)$ of the order of 30 mV in both of the regimes considered. The best fit is obtained for $\Gamma/U = 0.5$ in the unitary limit both below and above the symmetric limit, and for $\Gamma/U = 0.04$ or 0.07 in the Kondo regime (below or above the symmetric limit, respectively). Finally, by keeping the same correspondence between V_G and ε_0/U and using $\delta = \pi n_0$, we derive the dependence of the phase shift with V_G from results obtained in Fig. 2(a). As can been

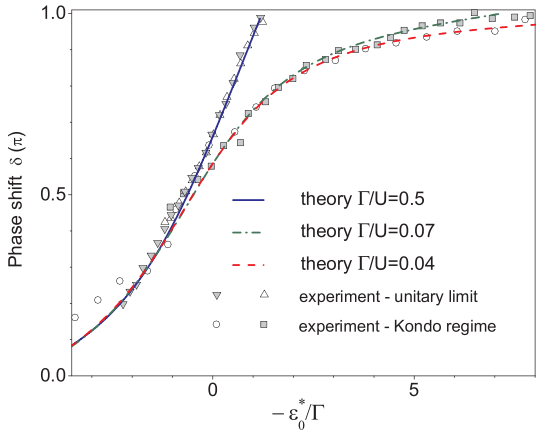

FIG. 3 (color online). Fit of the experimental data for the V_G dependence of the phase shift with the BA results for $\delta = \pi n_0$ as a function of $-\varepsilon_0^*/\Gamma$. Making use of the electron-hole symmetry, experimental results both below and above the symmetric limit are reported using the same scales. They are represented by triangles pointing down and up, respectively, in the unitary limit, and by circles and squares, respectively, in the Kondo regime (incorporating a shift in the δ scale; cf. text). The best fit is obtained for $\Gamma/U = 0.5$ in the unitary limit (both below and above the symmetric limit), and for $\Gamma/U = 0.07$ or 0.05 in the Kondo regime (below or above the symmetric limit, respectively).

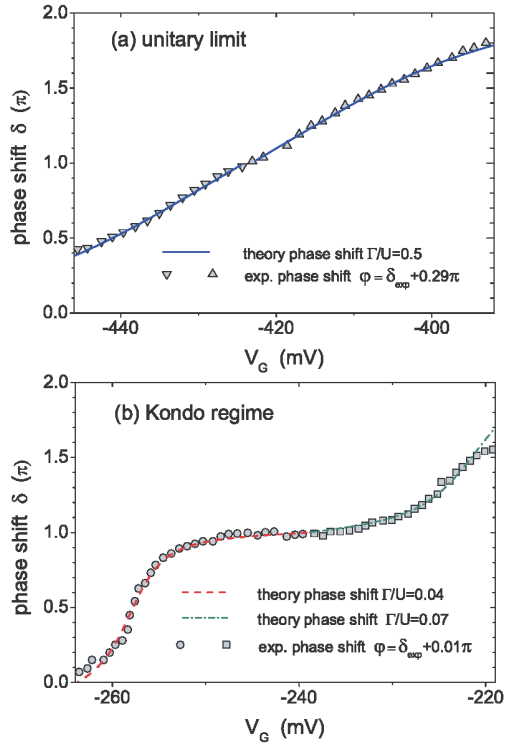

FIG. 4 (color online). Phase shift as a function of the gate voltage V_G. (a) Unitary limit. Theoretical results from Bethe ansatz calculations at $\Gamma/U = 0.5$ compared to the experimental data for $\varphi/\pi = \delta_{\mathrm{exp}}/\pi + 0.29$ (triangles pointing down and up). (b) Kondo regime. Same thing with $\Gamma/U = 0.04$ and 0.07, $\varphi/\pi = \delta_{\mathrm{exp}}/\pi + 0.01$ (circles and squares).

seen from Fig. 4, our theoretical predictions are in quantitative agreement with the experimental data. The fit is all the more remarkable that it is performed in the presence of a single fitting parameter Γ/U only.

In conclusion, we have proposed a theoretical analysis of the transmission phase shift of a quantum dot in the presence of Kondo correlations and confronted our results with the Aharonov-Bohm interferometry and conductance measurements. We have explained the presence of a factor of 2 difference between the total phase of the S-matrix (responsible for the shift in the AB oscillations), and the one appearing in the expression of the conductance $G \sim \sin^2(\delta/2)$. Our calculations based on Bethe ansatz lead to a remarkable quantitative agreement with experimental results. The whole discussion so far has been restricted to the low temperature regime. One of the next goals will be to include finite temperature effects as well as to study the role of a magnetic field and consider the out-of-equilibrium situation.

We thank N. Andrei for his encouragement and discussions during the course of this work. We also thank P. Nozières and E. Kats for helpful discussions. A. J. thanks the Physics Department at Rutgers University for hospitality. M. L. acknowledges the hospitality of the Aspen Center for Physics and the Kavli Institute for Theoretical Physics in Santa Barbara where part of this work has been done. This work was supported by the Institute for Condensed Matter Physics (IPMC) of Grenoble.

*Also at the Centre National de la Recherche Scientifique (CNRS), France.

[1] D. Goldhaber-Gordon, J. Gores, M. A. Kastner, H. Shritkman, D. Mahalu, and U. Meirav, Phys. Rev. Lett. **81**, 5225 (1998).
[2] S. M. Cronenwett, T. H. Oosterkamp, and L. P. Kouwenhoven, Science **281**, 540 (1998).
[3] W. G. Van der Wiel, S. De Franceschi, T. Fujisawa, J. M. Elzerman, S. Tarucha, and L. P. Kouwenhoven, Science **289**, 2105 (2000).
[4] Y. Ji, M. Heiblum, D. Sprinzak, D. Mahalu, and H. Shtrikman, Science **290**, 779 (2000).
[5] Y. Ji, M. Heiblum, and H. Shtrikman, Phys. Rev. Lett. **88**, 076601 (2002).
[6] D. C. Langreth, Phys. Rev. **150**, 516 (1966).
[7] P. Nozières, J. Low Temp. Phys. **17**, 31 (1974).
[8] U. Gerland, J. von Delft, T. A. Costi, and Y. Oreg, Phys. Rev. Lett. **84**, 3710 (2000).
[9] L. I. Glazman and M. É. Raĭkh, JETP Lett. **47**, 452 (1988).
[10] T. K. Ng and P. A. Lee, Phys. Rev. Lett. **61**, 1768 (1988).
[11] E. Merzbacher, *Quantum Mechanics* (Wiley, New York, 2000).
[12] A. C. Hewson, *The Kondo Problem to Heavy Fermions* (Cambridge University Press, Cambridge, U.K., 1993).
[13] J. Friedel, Can. J. Phys. **34**, 1190 (1956).
[14] N. Levinson, K. Dan. Vidensk. Selsk. Mat. Fys. Medd. **25**, 9 (1949).
[15] L. I. Schiff, *Quantum Mechanics* (McGraw-Hill, New York, 1968).
[16] L. Rosenberg and L. Spruch, Phys. Rev. A **54**, 4978 (1996).
[17] L. Rosenberg and L. Spruch, Phys. Rev. A **54**, 4985 (1996).
[18] J. Konig, W. Hofstetter, and H. Schoeller, Phys. Rev. Lett. **87**, 156803 (2001).
[19] R. Landauer, Philos. Mag. **21**, 863 (1970).
[20] N. S. Wingreen and Y. Meir, Phys. Rev. B **49**, 11 040 (1994).
[21] Note that Eq. (5) is valid only when $T \ll T_K$. Whereas the condition is satisfied in the experiments performed in the unitary limit, the relation does not hold for experiments performed in the Kondo regime when weaker coupling strength introduces a reduction of T_K.
[22] N. Kawakami and A. Okiji, J. Phys. Soc. Jpn. **51**, 2043 (1982).
[23] N. Kawakami and A. Okiji, J. Phys. Soc. Jpn. **51**, 1145 (1982).
[24] A. M. Tsvelick and P. B. Wiegmann, Adv. Phys. **32**, 453 (1983).
[25] F. D. M. Haldane, Phys. Rev. Lett. **40**, 416 (1978).
[26] This can be proved by noticing that Γ is almost unrenormalized in the $n_0 \to 0$ limit.

Chapter 3

Phase Lapses

3.1 Introduction

In the experiment the transmission phase shift is obtained from the measurements of the net current at the drain of the Aharonov-Bohm interferometer ring. For a given value of the gate voltage V_G which controls the occupancy of the quantum dot Aharonov-Bohm oscillations of the drain current are observed as a function of the magnetic flux threading the ring. These oscillations are shifted when a gate voltage is applied to the dot. The value of the corresponding shift is related to the transmission phase shift through the quantum dot. The phase determined by quantum interferometry increases continuously with the gate voltage V_G until exhibiting an abrupt jump at a given value of V_G corresponding to an even number of electrons in the dot. The latter jump is also named as a "phase lapse". The detailed description of the experimental technique and the main results are given in Sec.1.2. A large number of papers is devoted to the interpretation of the abrupt jumps observed in the phase shift [39, 40, 41, 42]. A review of the different approaches can be found in Ref.[60].

In this chapter we propose to discuss the evolution of the coherent contribution to the drain current as a function of the magnetic field and the gate voltage, $I_{AB} = I_{AB}(B, V_G)$, rather then the behavior of the transmission phase shift of the quantum dot as a function of V_G, $\delta = \delta(V_G)$. The results for the current are represented as a $2D$ plot in the plane (B, V_G). The evolution of the transmission phase shift of the quantum dot is then deduced from these plots as the change in the position of the maxima of I_{AB} with the gate voltage V_G. Thus, we carry out the analysis in a way analogous to the one used by experimentalists.

The drain current strongly depends on the state of the quantum dot. We calculate the drain current in the cases when the quantum dot is in the unitary limit, the Kondo correlation and the Coulomb blockade regimes. We briefly discuss each of these regimes and the crossover between them.

3.2 Phase lapse at $T = 0$ in the unitary limit and Kondo correlation regimes

3.2.1 Magnetic and non-magnetic regimes. Phase diagram at $T = 0$

Following Ref.[6], when the Coulomb repulsion energy U is large, the ground state of the system described by the Anderson model is most of the time nonmagnetic. Using the Hartree-Fock approximation, Anderson showed that the model leads to a transition between a magnetic and a non-magnetic states depending on the values of the density of state of conduction electrons, the coupling strength and the Coulomb repulsion energy (see for example Eq.2.38 or Fig.2.1). Fig.3.1 reports the phase diagram of the model as a function of $\pi\Gamma/U$ and $\epsilon_F - \epsilon_0/U$. It shows that in the case of large coupling strength $\Gamma \gtrsim U$ there is no magnetic moment at the impurity site. On the contrary, small values of the coupling strength $\Gamma \ll U$ lead to the formation of a magnetic moment at

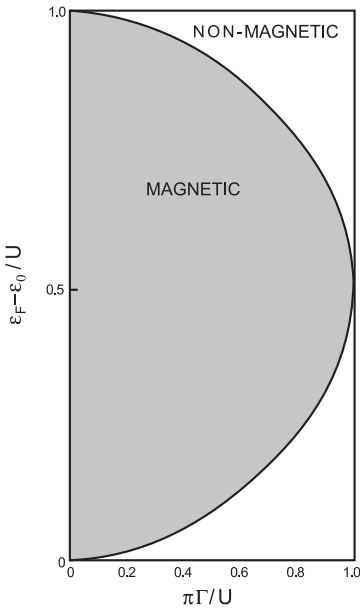

Figure 3.1: Phase diagram of the Anderson model as a function of $\pi\Gamma/U$ and $\epsilon_F - \epsilon_0/U$ in the Hartree-Fock approximation (Ref.[6]).

the impurity site. The system shows a magnetic behavior in a range of $\epsilon_F - \epsilon_0$ which becomes larger and larger when Γ/U decreases.

The Hartree-Fock approximation used by Anderson [6] qualitatively describes the system at high-temperatures. At low temperatures due to the Kondo effect, the magnetic moment at the impurity site is screened by the spins of the conduction electrons. The ground state is therefore nonmagnetic too. Thus, in the limit of zero temperature the system shows a non-magnetic behavior for any value of the parameters ϵ_0, Γ and U. In this limit the results presented in the Chapter 2 hold and we will derive benefit from them.

3.2.2 Net current through an Aharonov-Bohm ring

The net current at the drain of an AB ring at equilibrium is proportional to the bias voltage $I_{AB} = V_{SD}\, G_{AB}$ where G_{AB} is the total conductivity of the ring given by

$$G_{AB} = \frac{2e^2}{h} |t_{ref}|^2 + \frac{2e^2}{h} |t_{QD}|^2 + \frac{4e^2}{h} \mathtt{Re}\left[t_{ref} t^*_{QD}\right] \tag{3.1}$$

For the transmission amplitude t_{QD} of the quantum dot, we take the expression derived in Chapter 2

$$t_{QD} = -ie^{i\delta} \sin \delta/2 \tag{3.2}$$

where $\delta = \pi n_0$. Thus the knowledge of the occupation number as a function of the energy (or the gate voltage) is sufficient to calculate the ring current. The ring current can then be calculated as a function of the magnetic field, $\Phi = BS$, and the gate voltage,

$n_0 = n_0(V_G)$. The transmission amplitude t_{ref} through the reference arm can be taken as real. First, we assume that $t_{ref} = 1$. Later we will address the question of the effect of the magnitude of t_{ref} on the ring current.

Now we assume Eq.3.2 to be valid in the case when the spectral density on the impurity site is given by a series of localized levels (or resonances)

$$\epsilon_0 \sum_\sigma c_\sigma^\dagger c_\sigma \longmapsto \sum_\lambda \epsilon_\lambda \sum_\sigma c_{\sigma\lambda}^\dagger c_{\sigma\lambda} \tag{3.3}$$

The total occupation number is given by the sum of the occupation numbers of each localized level

$$n_0 = \sum_\lambda \sum_\sigma n_{0\lambda\sigma} = \sum_\lambda n_{0\lambda} \tag{3.4}$$

where $n_{0\lambda} = \sum_\sigma n_{0\lambda\sigma}$. For simplicity, we assume all the resonances to be described by the same parameters. To calculate the ring current, given by Eq.3.1, we use the sum of the solutions of the Bethe ansatz equations for the occupation number for each λ, Eq.3.4. We study two different regimes: the unitary limit and the Kondo correlation regimes for which $\Gamma/U = 0.5$ and $\Gamma/U = 0.04$ respectively.

3.2.2.a Unitary limit regime

The unitary limit regime corresponds to large values of the coupling strength. We take the value obtained from the fit performed in Chapter 2: $\Gamma/U = 0.5$. In this case the Kondo temperature is high, T_K from 1.5 to 2 K. The low-temperature limit, $T \ll T_K$, is then experimentally accessible. The occupation number in this regime increases almost linearly as a function of the energy (or the gate voltage), see Fig.1.17(a) or Fig.2.12(a). The occupation number as a function of ϵ_0 is obtained from the exact Bethe ansatz solution of the Anderson model for the case $\Gamma/U = 0.5$.

The $2D$ plot of the ring current as a function of the Aharonov-Bohm phase, $\theta = 2\pi\Phi/\Phi_0$, and gate voltage, V_G, is shown in Fig.3.2. To fit the experimental results we need to consider the opposite direction of the magnetic field: $\theta \to -\theta$. This $2D$-plot is in excellent agreement with the experimental results (see Fig.2a of Ref.[35]). The phase shift defined as earlier shows a gradual increase from 0 to 2π. 2π corresponds to the period of the Aharonov-Bohm oscillations of the current. The points where $I_{AB} = I_{ref}$ are indicated by a dashed (see Figs.3.2 and 3.3) line which corresponds to the evolution of the phase shift as a function of V_G.

The transmission amplitude t_{QD} vanishes when the occupation of the dot reaches the value $n_0 = 2$ i.e. when $\delta = 2\pi$ since $\sin \delta/2 = 0$. This fact results in a abrupt change of the position of the maxima of the Aharonov-Bohm current oscillations and therefore in a "phase lapse" in the phase evolution. Strictly speaking, at this point there is no oscillation of the current. When the transmission amplitude vanishes, the arm of the interferometer which the quantum dot is embedded in, is locked. The source-drain current is then given by the current through the reference arm $I_{ref} \propto |t_{ref}|^2$ only which does not depend on the magnetic flux. When the gate voltage V_G further increases, the

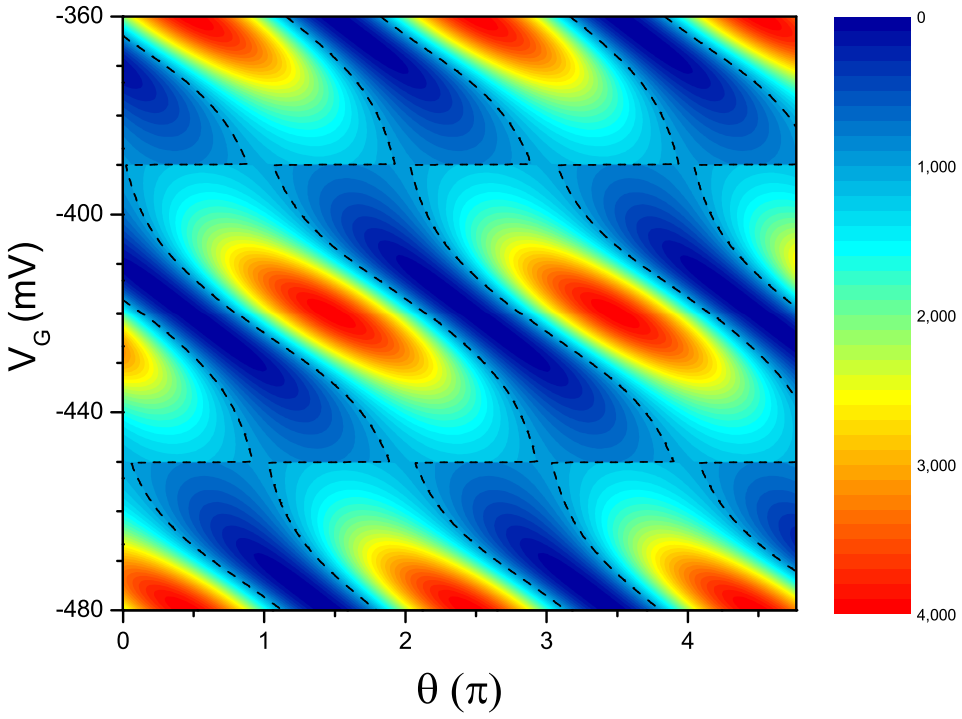

Figure 3.2: The $2D$ plot of the ring current (transparency) as a function of the magnetic field θ and the gate voltage V_G when the quantum dot is in the unitary limit regime.

maxima of the ring current turn out to be shifted by half of the period of the Aharonov-Bohm oscillations $\Delta\delta = \pi$. The maxima of the ring current do not return to their initial positions. This feature of the transmission phase shift is usually named as an "incomplete phase lapse". It results from the change of sign of the magnitude of the transmission amplitude when δ reaches the value 2π. We would like to emphasize at this point the importance of the factor of 2 that we found in the factor sin $\delta/2$ contained in t_{QD}, to get an incomplete phase lapse

3.2.2.b Kondo correlation regime

The Kondo correlation regime corresponds to small values of the coupling strength Γ. We take the value obtained from one of the fits given in Chapter 2: $\Gamma/U = 0.04$. This regime corresponds to a very low Kondo temperature: T_K from 1.0 to 0.1 mK. The occupation number in this regime exhibits a staircase behavior as a function of the energy or the gate voltage. The plateau occurs in the vicinity of $\epsilon_\lambda = -U/2$.

The $2D$ plot of the ring current as a function of the Aharonov-Bohm phase, $\theta = 2\pi\Phi/\Phi_0$, and the gate voltage, V_G, is shown in Fig.3.3. Since the Kondo temperature is

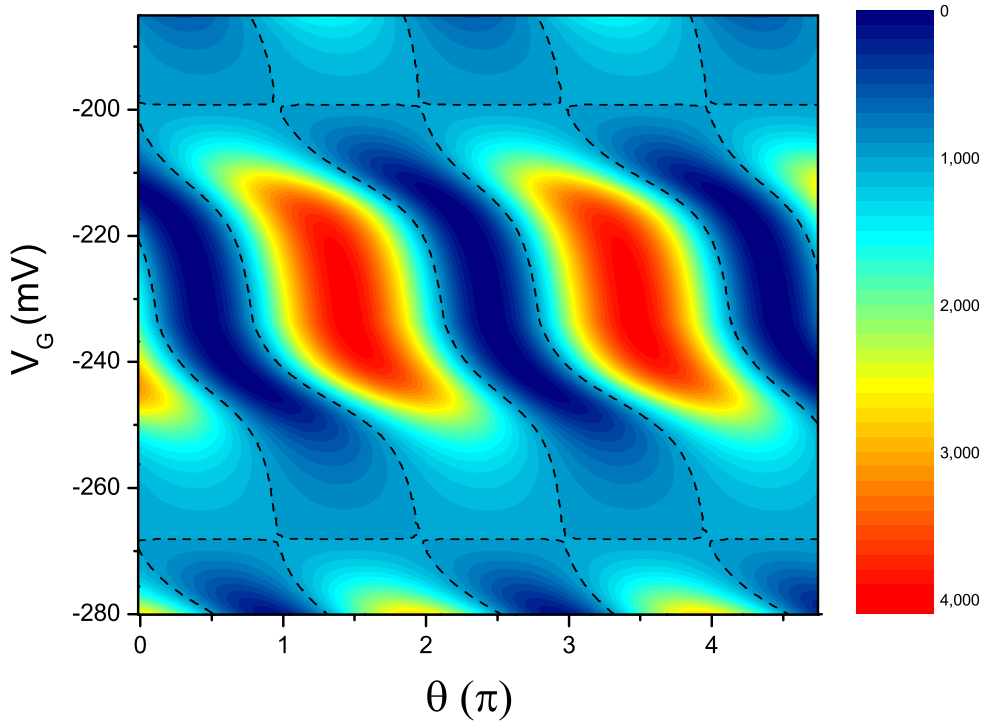

Figure 3.3: The $2D$ plot of the ring current (transparency) as a function of the magnetic field θ and the gate voltage V_G when the quantum dot is in the Kondo correlation regime.

low, the temperature at which the experiments are performed always puts the system at $T > T_K$ (high temperature limit). The conductance in the vicinity of the symmetric limit of the Anderson model (at the middle of the odd valley, $n_0 = 1$) is suppressed. On the contrary, our result, displayed in Fig.3.3 corresponds to the $T = 0$ limit, when the conductance reaches the unitary limit $2e^2/h$.

The phase evolution shows a gradual increase from 0 to π followed by a plateau, and then again by an increase from π to 2π. When the phase reaches the value $\delta = 2\pi$ the transmission amplitude, t_{QD}, vanishes. This zero of the transmission amplitude results in an abrupt change of the position of the maxima of the Aharonov-Bohm current oscillations. When the gate voltage V_G further increases, the maxima of the ring current turn out to be shifted by half of the period of Aharonov-Bohm current oscillations exactly as in the previous case when the coupling strength to the leads is strong (unitary limit, see Fig.3.2). As before, we emphasize that the "incomplete phase lapse" which occurs in the V_G-dependence of the phase results from the factor of 2 difference between the sinus and exponential terms in t_{QD}.

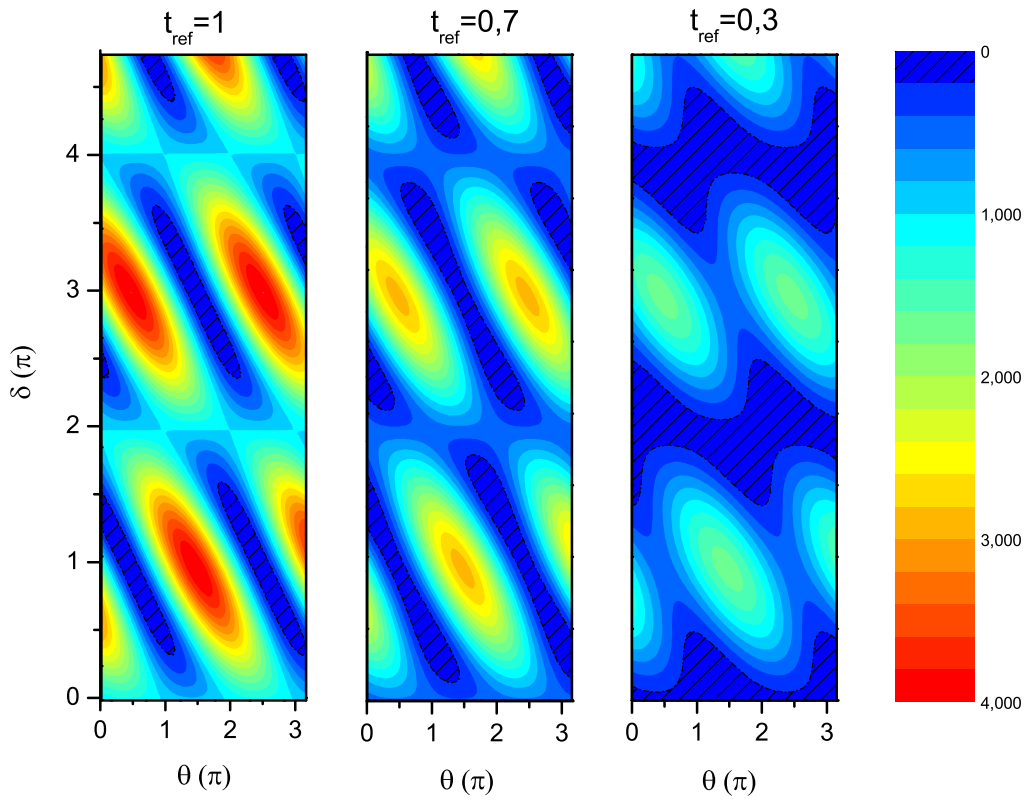

Figure 3.4: The $2D$ plot of the ring transparency as a function of $\theta = 2\pi\Phi/\Phi_0$ and $\delta = \pi n_0(V_G)$ at different values of t_{ref}: 1.0, 0.7 and 0.3. The points where $T_{AB} = 0.2$ are indicated by a dashed line.

3.2.3 Dependence of the source-drain current with the transmission amplitude of the reference arm t_{ref}

Previously, we have assumed that the transmission amplitude through the reference arm is real and corresponds to a fully open channel $t_{ref} = 1$. In general situations, it is not true, the reference arm may introduce an additional phase to the Aharonov-Bohm current oscillations. The conductance of the reference arm is generally lower than the conductance of an open channel, especially in the case of open interferometers. The transmission amplitude of the reference arm can be written as $t_{ref} = |t_{ref}|e^{i\alpha}$. If now we assume that the phase α does not depend on the gate voltage V_G and magnetic flux Φ, it can be omitted in the discussion since the measurements can only determine relative phase shift. The phase factor of the transmission amplitude of the reference arm gives a constant contribution to the phase which can be removed in the determination of δ_{QD}. Therefore one assumes the transmission amplitude through the reference arm to

be real, $t_{ref} = |t_{ref}|$. The question of the influence of the magnitude of t_{ref} may then be addressed. In the linear-response regime the current is proportional to the transparency. The complete expression for the ring transparency at $T = 0$ is given by

$$T_{AB}(\delta, \theta) = t_{ref}^2 + \sin^2(\delta/2) + 2t_{ref} \sin(\delta/2) \sin(\theta - \delta) \tag{3.5}$$

Here we have replaced the dependence of the current on the gate voltage by the phase δ which is a monotonous function of V_G as it is given by the sum rule expressed in Eq.2.27. For the transmission amplitude through the arm which the quantum dot is embedded in, we have used $t_{QD} = ie^{i\delta} \sin(\delta/2)$ (see Chapter 2). The result is shown in Fig.3.4. The ring transparency is determined for 3 values of t_{ref} (1.0, 0.7 and 0.3). When the reference transmission decreases, the peaks of the current are reduced in height and broadened. The height of the peaks decreases from $T_{AB} = 4$ for $t_{ref} = 1$, to $T_{AB} = 1.7$ for $t_{ref} = 0.3$. In Fig.3.4 the points where $T_{AB} = 0.2$ are indicated by a dashed line. One can clearly see from Fig.3.4 that when t_{ref} is small, the consecutive peaks are separated by a large region where the ring current is small. This can be the reason why experimentally the span of the phase through two (single-particle) resonances is lower than the expected value of 2π. Nevertheless, one can notice that the main feature, the existence of an incomplete phase lapse, occurs at any value of t_{ref}.

3.3 Conductance evolution in the low-temperature ($T \ll T_K$) and high-temperature ($T \gg T_K$) regimes

3.3.1 Phase diagram at finite T

At $T = 0$ and when the quantum dot is in the nonmagnetic state, we have shown that the conductance is given by

$$G = G_0 \sin^2 \frac{\delta}{2} \tag{3.6}$$

where $\delta = \pi n_0$ and $G_0 = 2e^2/h$ is twice the quantum of conductance. In the context of quantum dots, we have tested this prediction using independent experimental determinations [36, 35] of the transmission phase shift, δ, and of the conductivity G (see Fig.2.7). The question which now arises is the following: what happens to the transport through a quantum dot when the temperature increases?

To simplify the discussion, we assume that the coherent contribution to the current is brought by the electrons at the Fermi level only. The effect of temperature on the transmission phase shift will be discussed in Chapter 4.

3.3.1.a $T \ll T_K$

In the framework of the local Fermi liquid theory the low temperature corrections to the resistivity were calculated by P.Nozieres [48]. Since the correction to the resistivity are given by the expansion of $\sin^2[\delta(\epsilon)]$ on powers of ϵ one can transpose the result obtained

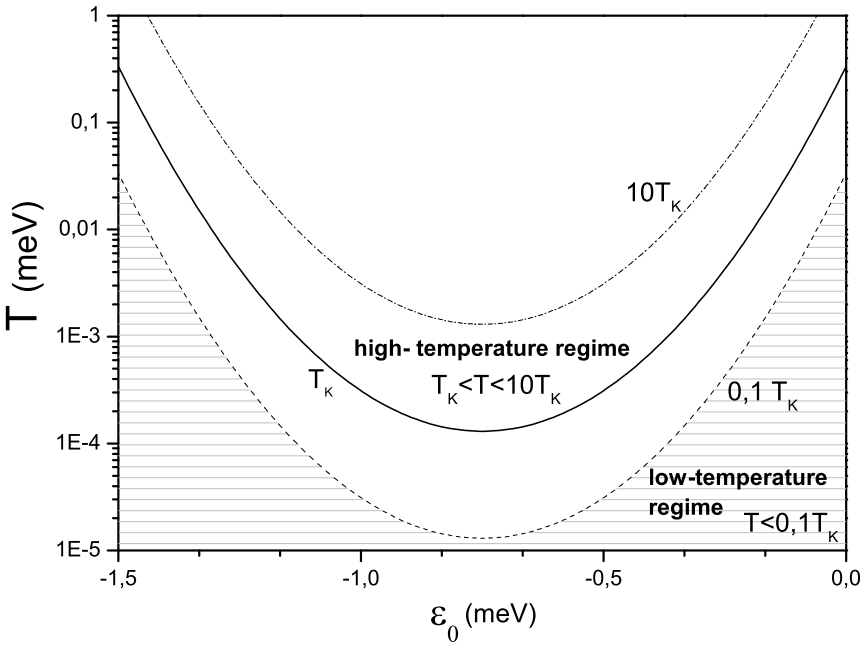

Figure 3.5: Phase diagram of the Anderson model for $U = 1.5$ meV and $\Gamma/U = 0.05$.

for the resistivity in $3D$, to the conductance of a quantum dot in $1D$. Taking only the s-scattering ($l = 0$) into account, the conductivity is given by

$$G(T) = G(0)\left[1 - c\left(\frac{T}{T_K}\right)^2\right] \tag{3.7}$$

with $c = \pi^4/16 \approx 6.088$. This expression is in good agreement with the almost exact NRG calculations [61] in the range of temperatures $0 \leq T \leq 0.1\,T_K$, see Fig.3.5. The behavior is clearly observed experimentally. In Fig.3.6 we have compared the V_G-dependence of the experimentally measured conductance at $T = 150$ mK in the unitary limit regime (page "Kondo effect at Unitary Limit (increasing temperature)" of Ref.[62]) and the prediction for $G(T)$ given by Eq.3.7 where the zero temperature conductance, $G(0)$, is taken from Eq.3.6. The lowest experimentally accessible temperature $T = 50$ mK is assimilated to the zero temperature limit (see Fig.2.7). One can notice that the conductance G as a function of V_G exhibits a peak around the value that we denote by V_G^0. The value that we find for V_G^0 is $V_G^0 = -397$ mV. For the dependence of T_K with V_G, we use a periodic parametrization, $T_K = T_K^0 + a(V_G - V_G^0)^2$ where T_K^0 is the Kondo temperature in the symmetric limit ($\min T_K = T_K^0$) and a is the curvature. This parametrization is not correct generally and if not, one should use the exact expression given in Ref.[59]. However the experimental results [29] show that the parabolic parametrization leads to reliable results for $T_K = f(V_G)$. Since the exper-

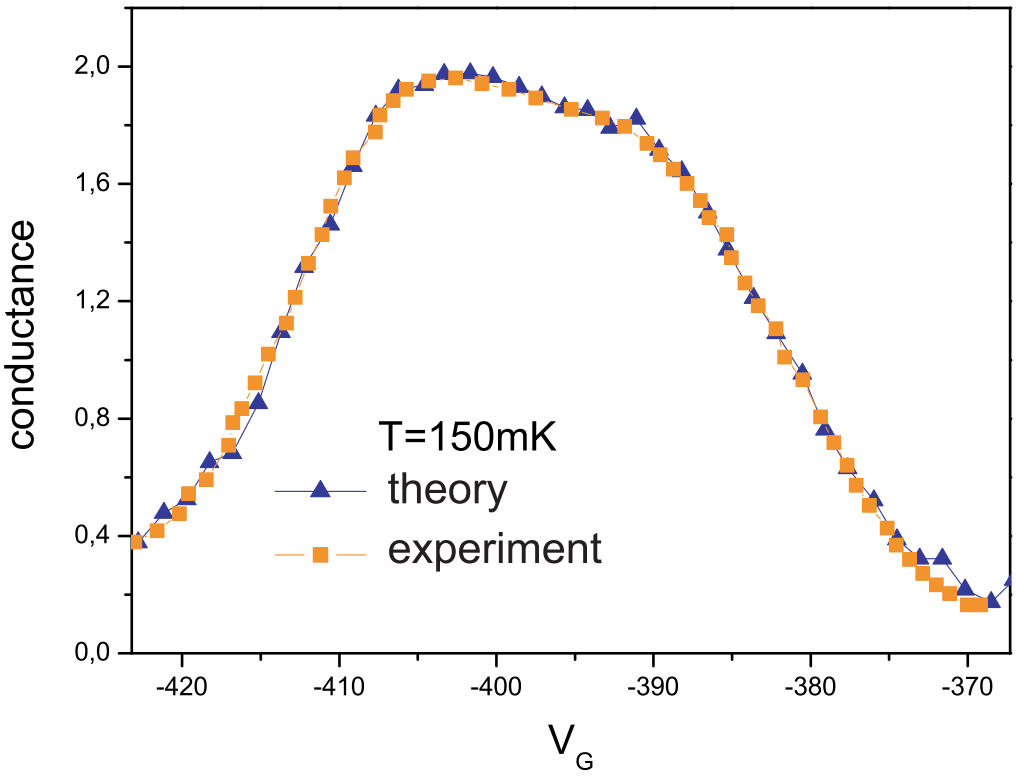

Figure 3.6: Experimentally measured conductance of the quantum dot at $T = 150$ mK (orange squares, [62]) compared to the low-temperature Fermi-liquid prediction (blue triangles) as a function of V_G.

imental temperature is fixed, the parameter that one can use to fit the experimental curve is the Kondo temperature $T_K(V_G)$. The best fit is obtained for $T_K^0 = 1.824$ K and $a = 0.09$ K/mV^2. Thus the temperature at which the experiments are carried out is low, $T \ll T_K^0 = \min T_K$ (see Fig.3.5), and the system is always in the low-temperature regime described by the Fermi liquid theory. The conductance given by the expression of Eq.3.7 is in good agreement with the experimentally measured conductance for all values of V_G.

The experimental conductance at $T = 300$ mK and at higher temperatures are out of scope of the low temperature Fermi liquid description. They correspond to a crossover [12, 61] between the low-temperature (strong coupling) and high-temperature regimes.

3.3.1.b $T \geq T_K$

At temperatures $T \geq T_K$ the system is no longer described by the Fermi liquid theory. Performing parquet diagram summation, Hamann [63] showed that in the limit $T \gg T_K$ the T-dependence of the conductance is given by

$$G(T) = \frac{G(0)}{2}\left[1 - \frac{\ln(T/T_{KH})}{\left[\ln^2(T/T_{KH}) + \pi^2 S(S+1)\right]^{1/2}}\right] \tag{3.8}$$

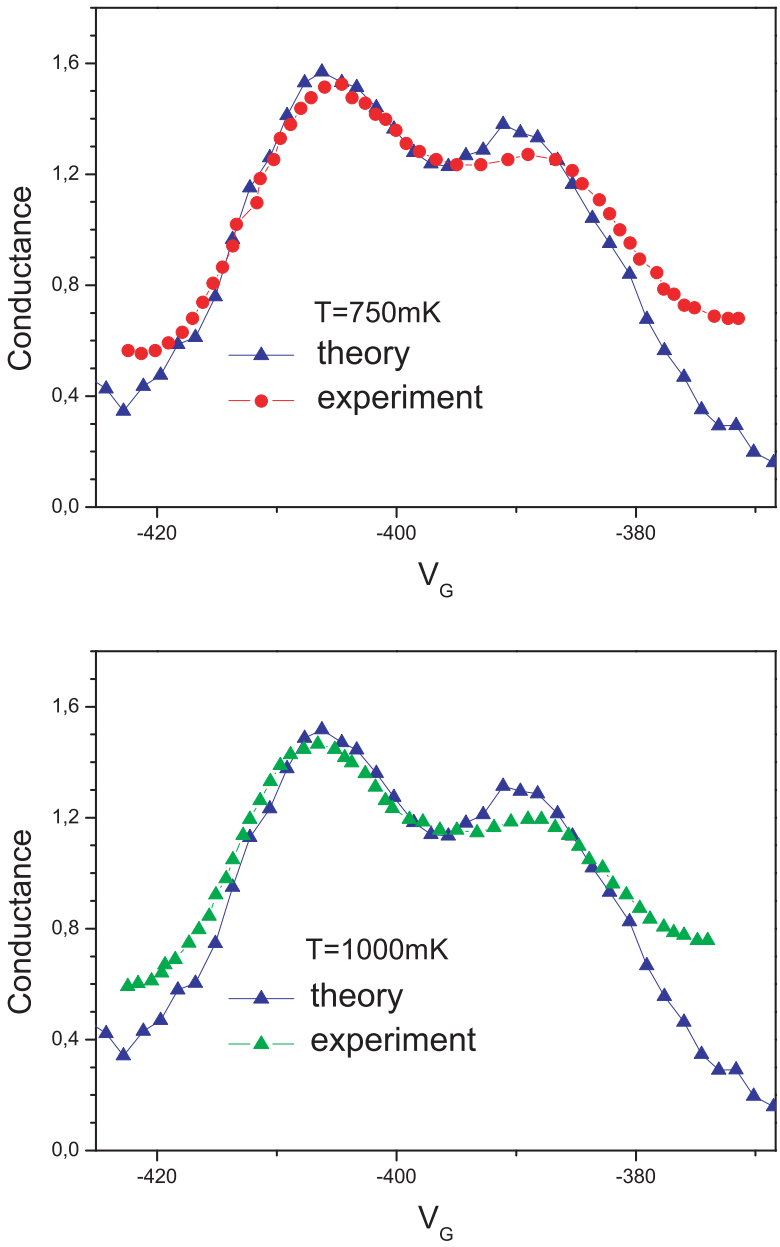

Figure 3.7: Experimentally measured conductance of the quantum dot [62] compared to the high-temperature results given by Eq.3.8, as a function of V_G at $T = 750$ mK (above) and $T = 1000$ mK (below). The experimental data are represented by red circles (at 750 mK) and green triangles (at 1000 mK). In both cfigures the theoretical points are represented by blue triangles.

where $T_{KH} = T_K/1.2$ and S is the total spin of the impurity (we take $S = 1/2$). The result expressed in Eq.3.8 is in good agreement with the NRG results [61] in the range $T_K \leq T \leq 10\,T_K$. In the range $0.5T_K < T < T_K$ the comparison with the NRG results show that the expression given by Eq.3.8 gives the correct result within an error of $\sim 10\%$ (see Fig.13 in Ref.[61]). The crossover regime that we have mentioned earlier takes place in the temperature range $0.1T_K < T < T_K$, see Fig.3.5. At higher temperatures, $T > 10\,T_K$, the conductance given by Eq.3.8 deviates considerably from the correct result since it is derived for s-d model which neglects the charge fluctuations. The latter are important at high temperatures.

In Fig.3.7 we have compared the V_G dependence of the conductance measured at 750 and 1000 mK and the prediction following Eq.3.8 where we have kept the same V_G-dependence of T_K as the one chosen in the low temperature regime ($T \ll T_K$). One can note that the temperature at which the experiments are carried out is lower than the Kondo temperature at the symmetric limit when T_K takes its minimum value, T_K^0. Nevertheless, the conductance given by Eq.3.8 is in good agreement with the experimentally measured conductance in the vicinity of the symmetric limit ($V_G = -397$ mV). Away from the symmetric limit, the Kondo temperature is higher and, as a result, the fit is less accurate.

We want to emphasize that once the Kondo temperature is fixed, there is no other fitting parameter left in the description.

3.3.1.c $T \gg \Gamma$

When the temperature is larger than $T = \Gamma \gg T_K$, the conductance given by Eq.3.8 strongly deviates from the correct results (given, for example, by NRG calculations [61]). When the temperature is lower than both the mean level spacing and the Coulomb repulsion energy, $T \ll \delta E \ll U$, only one localized state participates in the transmission of electrons between the leads and the dot. In this regime the coherent part of the conductance results from the the resonant scattering by the localized state. The transmission amplitude is then given by the Breit-Wigner formula [34] which can be rewritten in the form

$$t_{QD} = ie^{i\delta} \sin \delta \tag{3.9}$$

where $\delta = \pi n_{0\lambda}$ and $n_{0\lambda} = \arctan \frac{\Gamma_\lambda}{\epsilon - \epsilon_{0\lambda}}$ is the occupation of one localized level. Now we propose to make the same assumption as for the transmission amplitude of a quantum dot at $T = 0$ (see Sec.3.2.2). We assume that Eq.3.9 is valid in the case when the spectral density on the impurity site is given by a series of localized levels. n_0 is then equal to the total occupation of the dot.

3.3.1.d Experimental situation

The experimental temperature T_{exp} corresponds to a horizontal line on the phase diagram sketched in Fig.3.5. When the temperature at which the experiment is carried out is very low, $T \ll T_K^0$, the system is in the low-temperature regime for all values of

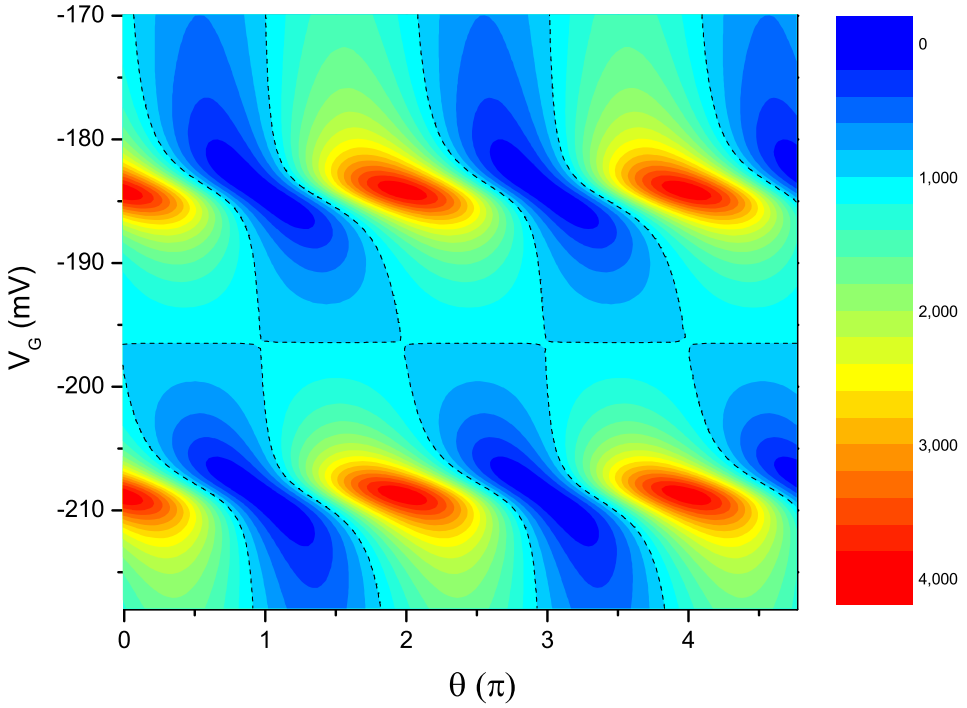

Figure 3.8: The $2D$ plot of the ring current (transparency) as a function of the magnetic field θ and the gate voltage V_G when the quantum dot is in the Coulomb blockade regime.

ϵ_0. A different situation takes place when T_{exp} is comparable to the other temperatures characteristic of the system.

When the temperature increases, in the vicinity of the symmetric limit of the Anderson model, the system enters into a crossover regime between the low-temperature and the high-temperature regimes. Away from the symmetric limit the system is still in the low-temperature regime. The conductance is well described by the Fermi liquid theory (Eq.3.7) in a range of ϵ_0 far from the symmetric limit (see Fig.3.5) while in the vicinity of the symmetric limit it is strongly suppressed. Nevertheless, the coherent contribution to the current through the quantum dot or its transparency is still given by Eq.3.6. Thus even if the total ring current at the middle of the valley (symmetric limit) is weak if is not zero the phase shift does not exhibit any phase lapse.

When the temperature is increased further, the system enters into the Coulomb blockade regime. The coherent part of the ring current can then be calculated using Eq.3.1 with the transmission amplitude given by Eq.3.9.

3.4 Ring current in the Coulomb blockade regime

In order to calculate the ring current, we consider two localized levels with energies ϵ_0 and $\epsilon_0 + U$ with the same coupling strength Γ which is taken to be small $\Gamma \ll U$. The total occupation number n_0 is then given by Eq.3.4 with $\lambda = 1$ and 2. It can be approximated by

$$n_0(\epsilon) = \frac{1}{\pi}\left[\arctan\frac{\Gamma}{\epsilon_0 - \epsilon} + \arctan\frac{\Gamma}{\epsilon_0 + U - \epsilon}\right] \tag{3.10}$$

where $\Gamma \ll U$.

The coherent part of the total ring conductance as a function of the magnetic field and the gate voltage is shown in Fig.3.8. The shift of the periodic Aharonov-Bohm oscillations from their initial position increases from 0 to π where π coincide with half of the period of the oscillations as a function of the magnetic field. At this point, $\delta = \pi$, the current through the arm with the quantum dot, vanishes and the oscillations disappear. When the gate voltage increases again, the oscillations turn out to be shifted by half of the period of the Aharonov-Bohm oscillations. As far as the transmission phase shift is considered, this corresponds to a complete phase lapse.

3.5 Conclusions

The expression for the transmission amplitude for the quantum dot in the Kondo regime at $T = 0$ obtained in Chapter 2 correctly describes (i) the conductance of the quantum dot, (ii) the phase evolution with the energy ϵ_0 of the localized level and (iii) the unexpected abrupt change of the transmission phase shift - the phase lapses which are found to be incomplete. All these results are in agreement with the experimental observations. Using the same arguments as for the case of a quantum dot in the Kondo regime, we show the presence of a complete phase lapse in the Coulomb blockade regime.

Experimentally, the crossover between the Kondo and the Coulomb blockade regimes is characterized by a complex behavior of the system. At the same temperature the quantum dot can be in different regimes depending on the value of the gate voltage V_G. In the odd valley at low temperatures (in the Kondo regime), the phase shift does not show any phase lapse, the phase exhibits an "off-resonant" behavior. When the temperature T increases (or the coupling strength Γ is reduced), the quantum dot gradually passes into the Coulomb blockade regime. The increase of the transmission phase shift by π in the vicinity of each resonance is governed by the resonant scattering off a quasilocal state in the dot. A complete phase lapse occurs at the middle of the valley when $\Gamma \ll T \ll \delta E \ll U$. The net current through the quantum dot has also an incoherent component resulting in a finite value of the conductance (at finite temperatures) contrary to the result, given by Eq.3.9 ($\delta = \pi$ at the middle of the valley). We have neglected the latter contribution in this chapter.

Chapter 4

Transmission phase shift at finite temperature in the out of equilibrium situation

4.1 Introduction

4.1.0.e Quantum dots vs impurity atoms

Quantum dots have provided one with new opportunities to control the Kondo effect experimentally. Whereas the values of the parameters such as the coupling strength of the impurity spin to the spins of the conduction electrons or the Coulomb repulsion energy between electrons on the impurity site are out of experimental control and even generally unknown in bulk systems, they can instead be turned individually in quantum dots.

This opens the way to a systematic study of the Kondo effect. Moreover, the quantum dot investigation field can also push research on the Kondo effect into new directions, and artificial structures can be studied in regimes which are out of scope for magnetic impurities in bulk systems. Thus new physical questions can be addressed.

4.1.0.f Nonequilibrium

In this chapter we propose to investigate one of these new directions, namely the nonequilibrium situation. We will also focus our attention on the scattering phase shift. There exist different types of nonequilibrium setups, but we will focus our attention mostly on nonequilibrium implementation at finite (static) bias voltages. For the case of a magnetic atom embedded in a bulk metal, achieving the nonequilibrium situation may be daunting, but this is not the case for quantum dots. A quantum dot weakly coupled to its leads constitutes a Kondo system in which nonequilibrium regime can be routinely achieved. More generally, an impurity in a small structure in which the applied bias voltage is dropped over a mesoscopic length is a nonequilibrium Kondo system.

Measurements of the phase shift (as well as of the conductance, but we will not address this question here) in nonequilibrium quantum dot setups have been performed in Heiblum's group [36, 35] at the Weizmann Institute of Science.

Quantum dots are small confined puddles of electrons realized at the surface of two-dimensional electron gas. These devices are characterized by large charging energy which in our description corresponds to the Coulomb repulsion energy U. This parameter essentially depends on the size of the device. Other parameters as the coupling strength to each lead, the energy structure or the filling of the quantum dot can be controlled individually. The Coulomb blockade and Kondo effects were observed under certain conditions in these quantum dots. Thus the quantum dots can be used to investigate the nonequilibrium manifestation of the Kondo effect. The applied bias voltage, as it has been observed, has nearly the same effect on the phase shift as heating - it leads to the suppression of the Kondo plateau located at $\delta \approx \pi$ but owns also some characteristic features. As it was already mentioned, this type of measurements is possible only under the condition that the coherence length is much larger than the system size (which in the context of the phase measurements is not the size of the quantum dot only but that of the Aharonov-Bohm interferometer). Usually, at equilibrium, this condition imposes restrictions on temperature, but the presence of finite bias voltage, $V_{SD} \neq 0$, also introduces decoherence processes which result in a reduced visibility

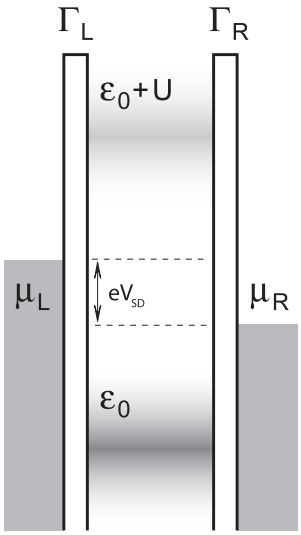

Figure 4.1: The two-reservoir Anderson model. The localized doubly degenerated discrete interacting level is coupled via tunnel barriers to two reservoirs of free electrons (Fermi seas). In general, the reservoirs can have different chemical potentials, $\mu_L - \mu_R = eV_{SD}$, that corresponds to the source-drain (bias) voltage. In the case then $V_{SD} = 0$ this model is equivalent to the standard equilibrium one-reservoir Anderson model.

(roughly speaking, the interference contribution to the Aharonov-Bohm source-drain current) and this makes the phase shift measurements impossible. Thus, experimentally measurements are limited both by temperature and bias voltage.

4.1.0.g Anderson model

As we have already mentioned in Chapter 1, following Glazman and Raikh [49] and Ng and Lee [50], one can describe the quantum dot coupled to two leads by a model analogous to the the Anderson model — a site with discrete, interacting levels coupled to two reservoirs — named as the Anderson model with two reservoirs sketched in Fig.4.1. As it was proved by Glazman and Raikh [49] at equilibrium these models are equivalent. This equivalence shows that the quantum dots can be described by a standard Anderson model which under certain conditions gives rise to a to the Kondo effect at low temperatures. This model has been used successfully to describe experiments on quantum dots at equilibrium. On the contrary, at nonequilibrium the two-reservoir Anderson model can not be mapped to the single-reservoir Anderson model. One needs to work with a two-reservoir Anderson model to describe the Kondo effect when the dot is biased out of equilibrium. The latter model is more general and has proved to give an excellent description in both the equilibrium and the nonequilibrium situation. The nonequilibrium properties have been intensively investigated since then. Here we use this model to describe the scattering off the quantum dot driven out of equilibrium.

Coming back to the equilibrium situation it was established that at zero temperature the Kondo resonance in the density of states pinned at the chemical potential in the leads

leads to a perfect transparency of a quantum dot when it is symmetrically coupled to the leads. More precisely, for all the values of ε_0 between 0 and U, where ε_0 is the bare-level energy and U is Coulomb repulsion energy, the conductance of the dot is $2e^2/h$. Out of equilibrium, the presence of the two chemical potentials dramatically affects the Kondo resonance. The latter is found to be splitted and strongly reduced in height [64, 65]. This effect is responsible for the suppression of the enhanced conductance through a quantum dot in the Kondo regime. It is thus expected that the scattering phase shift is affected by the presence of V_{SD}, as it is experimentally observed.

It is important to note that the (equilibrium) Anderson model is integrable and that an exact solution can be found by use of Bethe Anzatz method [17],[15]. The arguments of integrability are also used to solve the two-reservoir Anderson model out of equilibrium [66]. Although the integrability is used, the nature of the problem is such that the results that are obtained are not exact, but should be considered as an approximation.

4.1.0.h Calculation of the current

In the framework of the Keldysh nonequilibrium technique it is possible to derive a formal expression for the fully nonlinear current through the nonequilibrium QD in terms of the localized electron exact Green function [67, 68]. The analysis supports arbitrary interactions in the mesoscopic region, but the leads are assumed to be noninteracting. It was shown then that the nonequilibrium current through a quantum dot can be expressed in a way similar to the equilibrium case. However, the expression for the current in the interacting case ($U \neq 0$) cannot be obtained in general from the Landauer formula ,i.e. the transmission function (or the transmission probability) cannot be written as $\mathsf{T}(\epsilon) = t^{\dagger}(\epsilon)t(\epsilon)$, where $t(\epsilon)$ is the transmission amplitude containing additional information about the transmission phase shift [67]. The Landauer formula for the linear response in conductance holds for the noninteracting case ($U = 0$) and the interacting case at zero temperature. At finite temperatures and bias voltages, current has both coherent and incoherent contributions [69, 68]. The first one, the coherent contribution, obeys the Landauer formula and is supposed in our approach to be the only contribution to the interference current.

4.1.0.i Calculation of the phase

As far as phase shift calculations are concerned, an important contribution was made by Gerland et al.[38]. The effect of the Kondo correlations on the phase shift (indeed, on the transmission amplitude) was studied. The evolution of the phase shift in the different regimes finite temperatures, magnetic fields and/or bias voltages was investigated as well. At equilibrium these calculations confirm the Friedel sum rule within high accuracy. The transport properties are found to be drastically affected by the source-drain voltage, V_{SD}. The transmission amplitude was calculated using mainly numerical renormalization group (NRG) approach.

The phase is calculated in the linear response regime (in the case of a finite voltage for a large range of temperatures). The expression for the total transmission amplitude

is given by the "thermally averaged transmission amplitude" through the dot for the electrons incident with mean energy eV_{SD}, Eq.(2) of [38]. Within this approximation, roughly speaking, only electrons within the thermal energy window $\mu \pm T$, where T is the temperature, contribute to the current. Out of equilibrium one expects the current to be carried by electrons within wider energy window $\mu_L + T > \varepsilon > \mu_R - T$ [69] (here we consider $\mu_L > \mu_R$). Another important point is the assumption that the quantum dot is not driven out of equilibrium by the source and drain. This assumption is believed to be realistic for real Aharonov-Bohm interferometers. Nevertheless at large bias voltages the ground state of a quantum dot in general is not an equilibrium one and we propose to take into account the corresponding effects.

We derive the fully nonlinear expression for the scattering phase shift at finite bias voltages and temperatures. The calculations that we performed are based on the Landauer-Buttiker approach and do not involve linear-response formalism. The linear-response expression, as well as the equilibrium results, can be obtained as a limiting case of our calculations. We define the scattering phase shift as the shift of the Aharonov-Bohm source-drain current oscillations, $\Delta(V_G) \equiv \delta I_{AB}(\theta; V_G)$, where $\theta = 2\pi\Phi/\Phi_0$ is the Aharonov-Bohm phase and V_G is the gate voltage which controls the ground state of the quantum dot. This definition is consistent with the experimentally measured quantity. So, starting from the expression for the current through the A-B ring, we are able to express the scattering phase shift, Δ, in terms of the localized electrons retarded Green function. The latter Green function, is generally difficult to obtain analytically. This part of the work was done numerically. Furthermore, using Kramers-Kronig relations one can relate the real and imaginary parts of the retarded Green function. Thus to obtain Δ it is enough to know the density of states of the localized electrons. To obtain the values of the density of states we used the Keldysh technique [70, 71], appropriate for nonequilibrium problems, combined with perturbative methods (that we will present later on). We expect our result to correctly describe the nonequilibrium behavior of the system.

Let us comment about shortcomings of the method that we propose. To obtain the density of states of localized electrons we apply the non-crossing approximation [72, 73, 74]. We know that the latter approximation may lead to a considerable error in the evaluating of the height of the Kondo peak. As the scattering phase shift depends strongly on the behavior of the density of states at the Fermi level, unlike the occupation number, for example, we expect our result to be less accurate in certain cases. The most "sensitive" regime is the equilibrium zero-temperature limit. Although the zero-temperature equilibrium phase shift can be obtained using Levinson's theorem combined with the Friedel sum rule, see Chapter 2, the equilibrium regime ($\mu_L = \mu_R$) at zero temperature is out of reach of this method. The error introduced by this method remains considerable up to temperatures of the order of several T_K [75]. Nevertheless, at high temperatures or finite bias voltages, the error is expected to be not crucial. Another important shortcoming of our approach is the use of a finite-U Anderson model. This assumption is experimentally justified. It turns out that the Coulomb repulsion energy is the largest energy scale in the described systems but, however, all the experi-

mentally studied systems correspond to a large but finite U. Thus we can only propose a qualitative analysis of the problem.

4.2 Noncrossing approximation (NCA)

To obtain a well-behaved density of states from the non-equilibrium perturbation theory, one needs some way of summing diagrams to all orders in the hopping V. In finite-order perturbation theory there exist divergences associated with the bare level ϵ_0 and, at $T = 0$, logarithmic divergences near the chemical potentials due to the Kondo effect. To control these divergences, we employ the noncrossing approximation, which has been used successfully to treat the infinite-U Anderson model at equilibrium [72, 76].

4.2.1 Large-N expansion

When the diagrammatic perturbation theory is used, the introduction of a new parameter N, the degeneracy factor, makes some new techniques available which provide one with a way of calculating dynamic response functions or the one-electron Green function. These are the $1/N$ expansion or large-N approaches. Some simplifications are found in the large-N limit and the method itself becomes exact in the limit $N \to \infty$. These simple approximation schemes work very well for values of N that are of interest for application to rare earth impurities. Even for $N = 2$, which is also the case of quantum dots, one can get semi-quantitative results, which can be accurate to within a few percents for some physical quantities [76].

It is possible to classify the terms in the perturbation expansion in powers of the hopping V according to the order in $1/N$. We will not give here a complete set of rules of drawing and evaluating the diagrams but we propose a simple analysis in terms of a $1/N$ expansion.

The lower order non-vanishing terms for the reduced resolvent propagators in a perturbation expansion in V are given by

$$R_0^{(2)}(\omega) = \sum_{k,m} \frac{|V_k|^2}{(\omega-\epsilon_0)^2} \frac{f(\epsilon_k)}{\omega-\epsilon_m+\epsilon_k} \tag{4.1}$$

$$R_{1,m}^{(2)}(\omega) = \sum_{k} \frac{|V_k|^2}{(\omega-\epsilon_m)^2} \frac{1-f(\epsilon_k)}{\omega-\epsilon_0+\epsilon_k} \tag{4.2}$$

where ϵ_0 is the energy of the empty site, ϵ_m is the energy of the site occupied by a single electron with momentum projection m, ϵ_k is the energy of conduction electron and $f(\epsilon)$ is the Fermi distribution function. The reduced resolvent is

$$R_\alpha(\omega) = \mathtt{Tr}_c \langle\alpha|\langle c|(\omega-\hat{H})^{-1}|c\rangle|\alpha\rangle/Z_c$$

where the subscript c denotes the trace over the conduction states, $|c\rangle$; $|\alpha\rangle$ are the impurity states $|n_F, 0\rangle$ and $|n_F+1, m\rangle$. The states $|\alpha\rangle$ are many-body states which include Coulomb interactions. The standard diagrammatic methods which use Wick's theorem are not applicable. Nevertheless one can develop an applicable form of perturbation theory but we do not address this question here. Our aim is just to classify the terms in the perturbation expansion along their dependence on the degeneracy factor N. Later

we will use the perturbation expansion for the Anderson hamiltonian in the slave boson representation. These auxiliary particles can be treated as ordinary particles.

The diagrams of the next, third, order in the expansion for $R_0(\omega)$ are given in Fig.4.2. Contributions from diagrams with non-overlapping conduction electrons, such as Fig.4.2

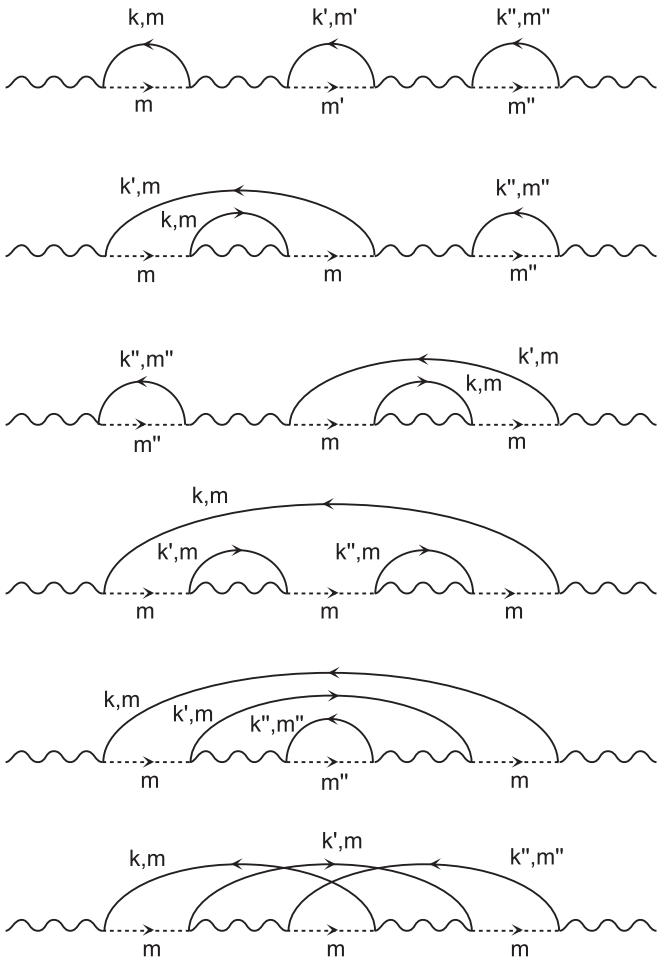

Figure 4.2: All the diagrams of order $|V|^6$ contributing to the $R_0(\omega)$. Solid, dashed and wavy lines represent conduction electron propagator, zero-order $R_{1,m}(\omega)$ and $R_0(\omega)$ correspondingly.

(1), (2) and (3), factorize. All the self-energies presented in the diagram Fig.4.2(1), the last part of diagram Fig.4.2(2) and the first part of diagram Fig.4.2(3) correspond to second order self-energy terms. The first part of diagram Fig.4.2(2) and the last part of diagram diagram Fig.4.2(3) represent the fourth order self-energy term.

The diagrams may be classified along their dependence on the degeneracy factor N. If the hopping matrix element is scaled along a factor $1/\sqrt{N}$, $V \to V/\sqrt{N}$, then the diagrams can be classified according to their dependence on $(1/N)^r$, where $r \in \mathbb{N}$. This scaling is required to enable a physically meaningful limit $N \to \infty$ to be taken. One

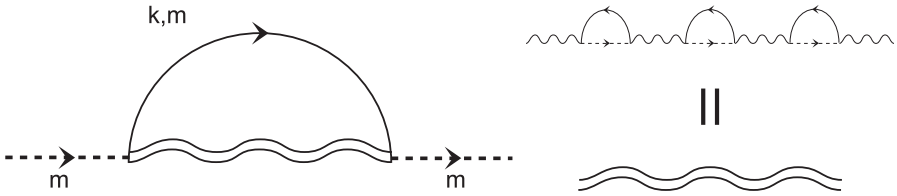

Figure 4.3: The leading order diagrams for $R_{1,m}(\omega)$ in a $1/N$ expansion. The double wavy line represents the "dressed" $R_0(\omega)$ propagator.

can see that in the diagram Fig.4.2(1) 3 independent m summations show up and so is of order $(1/N)^0$. The contribution to $R_0(\omega)$ self-energy shown in Fig.4.2(2), (3) and (5) are of order $(1/N)^1$ since they have only two independent m summations, and diagrams (4) and (6) have only one free m and are of order $(1/N)^2$.

The order $(1/N)^0$ diagrams for $R_0(\omega)$ are summed by taking the second order self-energy into account. The lowest order diagrams for $R_{1,m}(\omega)$ are of order $(1/N)^1$. All the diagrams for $G_{1,m}(\omega)$ to order $(1/N)^1$ are obtained by dressing the internal propagator $G_0(\omega)$ with the second order self-energy term. This is schematized diagrammatically in Fig.4.3.

4.2.2 NCA

We now consider ways of taking more diagrams into account by setting up self-consistent calculations for the two lowest order diagrams for the $R_0(\omega)$ and $R_{1,m}(\omega)$ propagators (or self-energy terms). As it can be seen, at lowest order in perturbation theory the $\Sigma_0(\omega)$ self-energy involves $\Sigma_{1,m}(\omega)$ while $\Sigma_{1,m}(\omega)$ self-energy involves $\Sigma_{1,m}(\omega)$. By using the two relations self-consistently, one obtains a set of coupled integral equations. The coupled equation for the self-energies (for a flat conducting band) are

$$\Sigma_0(\omega) = \frac{N\Delta}{\pi}\int \frac{f(\epsilon)}{\omega - \epsilon_m + \epsilon - \Sigma_{1,m}(\omega+\epsilon)}\,d\epsilon \tag{4.3}$$

$$\Sigma_{1,m}(\omega) = \frac{\Delta}{\pi}\int \frac{1-f(\epsilon)}{\omega - \epsilon_0 - \epsilon - \Sigma_0(\omega-\epsilon)}\,d\epsilon \tag{4.4}$$

where $\Delta = \pi|V|^2\rho$. This procedure allows us to take all non-crossing diagrams into account, and known generally as the Non-Crossing Approximation (NCA).

Solving these self-consistent equations corresponds to summing a subset of diagrams to all orders in the hopping matrix element V. This subset includes all diagrams with noncrossing conducting lines but does not correspond to any specific order in the $1/N$ expansion. It can be shown that all diagrams of leading order in $1/N$ (i.e. $(1/N)^0$ and $(1/N)^1$), where N is the number of (spin) degrees of freedom, are included in this subset. The lowest order diagram, which is not included in $R_0(\omega)$ is the one in Fig.4.2(6), which is of order $(1/N)^2$. In principle, those coupled equations can be made exact by including the vertex parts, $\Lambda(\omega, \epsilon_k)$, in the integrals to take into account the crossing diagrams (see Fig.4.4). As the lowest order contribution to these vertex parts, such as diagram

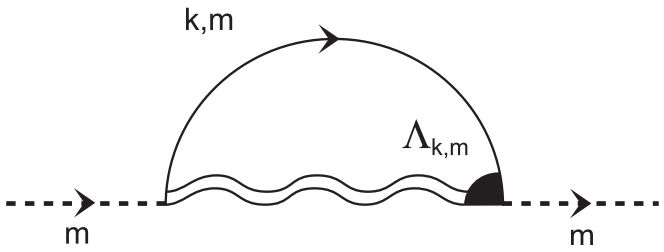

Figure 4.4: A schematic representation of the complete sum of diagrams for $\Sigma_{1,m}(\omega)$ self-energy, where $\Lambda_{k,m}$ take into account all the vertices.

(6) in Fig.4.2, are of order $(1/N)^2$ or higher, they are negligible in the large-N limit. Therefore the noncrossing approximation is expected exact in the large-N limit.

4.3 Slave bosons

The Anderson Hamiltonian can be studied using perturbation expansion theory in powers of the Coulomb interaction U. The expansion is performed about the non-interacting limit $U = 0$, so that the standard Feynman diagram method based on Wick's theorem can be used. The main problem in using this approach comes from the fact that, in systems of physical interest, U is usually the largest energy scales in the problem. In the latter case the result of perturbation theory to finite order are in general not good enough. In order to get reliable result in the strong coupling limit the summation of infinite series of diagrams is required. Diagrammatic techniques are reliable when the expansion parameter is a small quantity. For the Anderson impurity with $U \to \infty$, one can think of treating the hopping strength V as a perturbation. However, the standard diagrammatic approach also requires that the unperturbed hamiltonian to be that of a noninteracting system, i.e. quadratic in the second-quantized operators. In the limit of infinite U the bare Hamiltonian can be made quadratic by transforming the Hamiltonian into a new Hamiltonian, expressed in terms of new local operators. These operators create the three possible states of the site: a boson operator $b^\dagger$, which creates an empty site, and two fermion operators [77, 78, 79], $f_\sigma^\dagger$, which create a singly occupied states.

$$\begin{cases} |0\rangle &= b^\dagger|\Omega\rangle \\ |\sigma\rangle &= f_\sigma^\dagger|\Omega\rangle \end{cases} \tag{4.5}$$

In these expressions $|\Omega\rangle$ is the vacuum state. The initial ordinary electron operator on the site, which transforms an empty site into singly occupied site or vice versa, are decomposed into a boson operator and fermion operator

$$\begin{aligned} c_\sigma &= b^\dagger f_\sigma \\ c_\sigma^\dagger &= f_\sigma^\dagger b \end{aligned} \tag{4.6}$$

The slave bosons in (4.6) acts as a bookkeeping device which prevents double occupancy of the site. When an electron creation operator acts on the occupied site, the boson part acting on the vacuum annihilates the state

$$c_\sigma^\dagger f_{\bar\sigma}^\dagger|\Omega\rangle = f_\sigma^\dagger b f_{\bar\sigma}^\dagger|\Omega\rangle = 0 \tag{4.7}$$

In the slave boson representation, the Hamiltonian for the infinite-U Anderson model becomes

$$H = \sum_{\sigma;k\in L,R} \epsilon_{\sigma k} c_{\sigma k}^\dagger c_{\sigma k} + \sum_\sigma \epsilon_\sigma f_\sigma^\dagger f_\sigma + \sum_{\sigma;k\in L,R} \left(V_{k\sigma} c_\sigma^\dagger b^\dagger f_\sigma + \text{H.c.}\right) \tag{4.8}$$

The first two terms form the unperturbed, quadratic Hamiltonian and the last term, which represents hopping between site and leads, can be handled as a perturbation. The fermions and bosons are treated as ordinary particles in the perturbation expansion. The lowest-order diagrams are shown for the boson and fermion propagators in Fig.4.5.

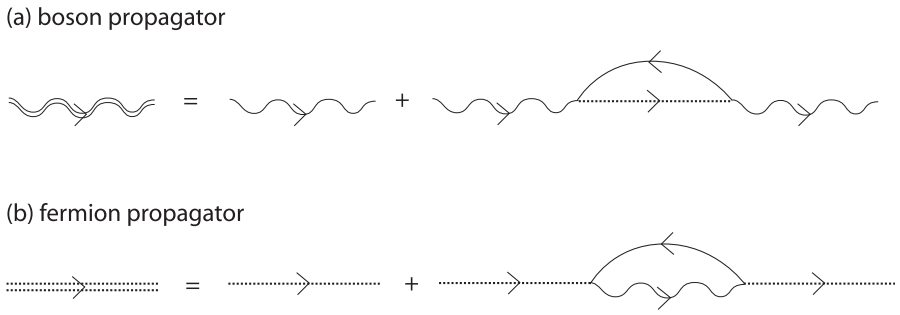

Figure 4.5: Diagrammatic expansion for (a) the slave-boson and (b) the fermion propagators. Wavy, dashed and solid lines correspond to the boson, fermion and lead electrons propagators respectively. The coupling between site and leads is treated as perturbation, so each vertex corresponds to a tunneling event.

While summation of few lower-diagrams is possible, techniques are also available to sum whole classes of diagrams such as NCA approach discussed previously.

So far we seem to have the great advantage that we are now dealing with operators for which the standard Wick's theorem is applicable. However, we still have to apply the constraint

$$\mathrm{Q} = b^\dagger b + \sum_\sigma f_\sigma^\dagger f_\sigma = 1 \tag{4.9}$$

which states that the physical states are restricted to the $\mathrm{Q} = 1$ ensemble. This difficulty can be solved by introducing a Lagrange multiplier (which is also named as the "complex chemical potential"). We will show below, when we will describe the Keldysh diagrammatic approach, how this constraint can be handled.

4.4 Keldysh formalism

We will now describe how to set up a diagram technique that is in principle suitable for calculating the Green's functions of systems in any non-equilibrium state. The diagram technique enables us to express the Green function of a system of interacting particles in terms of the functions for an ideal gas.

The usual (equilibrium) diagram technique at zero temperature involves the calculation of chronological products as

$$\langle\phi|T\left\{A(t)B(t')...\right\}|\phi\rangle \tag{4.10}$$

where $A(t)$, $B(t)$ ... are operators in the Heisenberg representation and $|\phi\rangle$ is the eigenstate of the system. A simplification is possible using the interaction representation

$$|\phi(t)\rangle = e^{iH_0t}e^{-iHt}|\phi(0)\rangle \tag{4.11}$$

where the full hamiltonian of the system, H, can be divided into two parts: the unperturbed hamiltonian, H_0, and the interaction part, H_{int}, so that $H = H_0 + H_{int}$. Note, that H_0 does not commute with the interaction part H_{int} and Eq.4.11 cannot be compressed. In the interaction representation Eq.4.10 takes the following form

$$\langle\phi_0|S(-\infty,+\infty)T\left\{\tilde{A}(t)\tilde{B}(t')...\,S(+\infty,-\infty)\right\}|\phi_0\rangle \tag{4.12}$$

The matrix S is defined by

$$S(t',t) = T\left[\exp\left\{-i\int_t^{t'} H_{int}(\tau)\,d\tau\right\}\right] \tag{4.13}$$

Where the shortcoming notation means the expansion of $\exp(x)$ in a Taylor series. The interaction Hamiltonian H_{int} is supposed to be adiabatically turned on from $t = -\infty$, and turned off at $t = +\infty$. The advantage of this description is that for evaluating the mean values on the exact eigenstates $|\psi\rangle$ of the system in the presence of interactions (generally unknown) one can use the eigenstates $|\phi_0\rangle$ of the unperturbed Hamiltonian, which are much easier to find. The main effort now is the evaluation of the S matrix. In the absence of irreversible effects, following Gell-Mann and Low theorem, the state of the system at $t = +\infty$ is identical to the state of the system at $t = -\infty$ up to a phase factor

$$S(+\infty,-\infty)|\phi_0\rangle = e^{i\alpha}|\phi_0\rangle \tag{4.14}$$

so that

$$\langle\phi_0|S(-\infty,+\infty)T\left\{\tilde{A}(t)\tilde{B}(t')...\,S(+\infty,-\infty)\right\}|\phi_0\rangle = \frac{\langle\phi_0|T\left\{\tilde{A}(t)\tilde{B}(t')...\,S(+\infty,-\infty)\right\}|\phi_0\rangle}{\langle\phi_0|S(+\infty,-\infty)|\phi_0\rangle} \tag{4.15}$$

The result expressed in Eq.4.14 is in the basis of the equilibrium diagrammatic approach. Out of equilibrium, in the presence of irreversible effects, this statement is no longer valid. The mean values can still be calculated as before using Eq.4.10, the only difference is that averaging is now taken over any quantum state of the system, and not necessary over the stationary state as in the equilibrium case. Since in a nonequilibrium system real dissipation or absorption of energy can occur, the state of the system in general is not known at $t = +\infty$ and one mast relate all quantities to the state of the system at $t = -\infty$. Such kind of generalization of the usual zero-temperature formulation is possible. In practice, this means that instead of having integrals from $t = -\infty$ to $t = +\infty$, as in Eq.4.13, all integrals have to be carried out along the path that starts and ends at $t = -\infty$. One can rewrite Eq.4.12 in terms of generalized time-ordering operator T_c

$$\langle\phi_0|S(-\infty,+\infty)T\left\{\tilde{A}(t)\tilde{B}(t')...S(+\infty,-\infty)\right\}|\phi_0\rangle = \langle\phi_0|T_c\left\{\tilde{A}(t)\tilde{B}(t')...\,S_c\right\}|\phi_0\rangle \tag{4.16}$$

where T_c is an operator ordering the times from left to right, not as usual from $-\infty$ to $+\infty$, but along the contour C made of a "positive" branch going from $-\infty$ to $+\infty$ and with a "negative" branch going from $+\infty$ to $-\infty$ as it is shown in Fig.4.6.

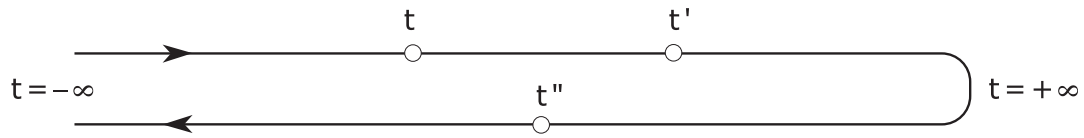

Figure 4.6: Keldysh contour C where $t < t'' < t'$ but $t_c < t'_c < t''_c$.

Thus on the "positive" branch, the times are ordered from $-\infty$ to $+\infty$, while on the "negative" branch the time order is inverted compared to the usual case: from $+\infty$ to $-\infty$. Any time of the negative branch (t" from Fig.4.6) is considered as posterior to any time on the positive branch (any of t or t' from Fig.4.6). All the times $\{t, t', ...\}$ of the chronological product in Eq.4.16 are on the positive branch, but the S-matrix

$$S_c = S(-\infty,+\infty)S(+\infty,-\infty) = T\left[\exp\left\{-i\int_c H_{int}(\tau)\,d\tau\right\}\right] \tag{4.17}$$

will introduce times on the negative branch of the contour in the perturbation expansion. Consequently, a Green function will depend not only on the times at which the operator acts, but also on the corresponding branch of the contour. Thus the Green function carries the additional indices and the usual perturbation expansion of the Dyson equation takes a matrix form. It is now possible to calculate the expression Eq.4.16 using standard diagram technique but since the times belonging to the negative branch (noted with subscript $-$) are posterior to any time belonging to the positive branch (noted with subscript $+$), we must introduce four Green functions

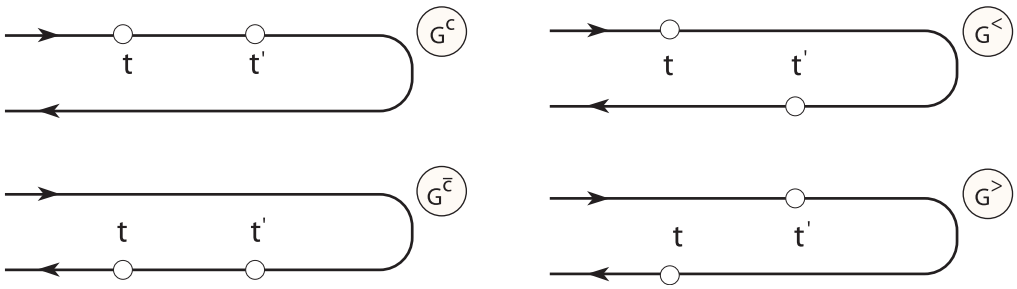

Figure 4.7: The four Green functions depending whether the time variables t and t' are on the positive or negative branches of the contour C

$$\left\{\begin{array}{lcll} G^c(r,t;r',t') & = & -i\langle T_c\left\{c(r,t_+)c^\dagger(r',t'_+)\right\}\rangle = & -i\langle T\left\{c(r,t)c^\dagger(r',t')\right\}\rangle \\ G^{\bar{c}}(r,t;r',t') & = & -i\langle T_c\left\{c(r,t_-)c^\dagger(r',t'_+)\right\}\rangle = & -i\langle \bar{T}\left\{c(r,t)c^\dagger(r',t')\right\}\rangle \\ G^>(r,t;r',t') & = & -i\langle T_c\left\{c(r,t_-)c^\dagger(r',t'_+)\right\}\rangle = & -i\langle c(r,t)c^\dagger(r',t')\rangle \\ G^<(r,t;r',t') & = & -i\langle T_c\left\{c(r,t_+)c^\dagger(r',t'_-)\right\}\rangle = & i\langle c^\dagger(r',t')c(r,t)\rangle \end{array}\right. \tag{4.18}$$

where T orders the times from $-\infty$ to $+\infty$ and $\bar{T}$ from $+\infty$ to $-\infty$.

In the diagram calculation the integrations, as we have already mentioned, are performed along the contour C; this is equivalent to perform the integrations from $-\infty$ to $+\infty$ and sum over subscript $(+)$ or $(-)$ of the branches of the contour C. Because the negative branch of the of the contour C goes from $+\infty$ to $-\infty$, any point of this branch corresponds to a $(-)$ sign (because of time differential $dt_- = -dt$), or equivalently any interaction on this branch corresponds to a $(-)$ sign. This summation over the branch indices is equivalent to using 2×2 matrices. Therefore the standard diagrammatic technique still holds, if one defines a Green function matrix

$$\mathbf{G} = \begin{pmatrix} G^c & G^> \\ G^< & G^{\bar{c}} \end{pmatrix} \tag{4.19}$$

The Dyson equation may then be written as

$$\mathbf{G}(r,t;r',t') = \mathbf{G}^0(r,t;r',t') + \int \mathbf{G}^0(r,t;r_1,t_1)\mathbf{\Sigma}(r_1,t_1;r_2,t_2)\mathbf{G}(r_2,t_2;r',t')\, dr_1 dr_2 dt_1 dt_2 \tag{4.20}$$

where

$$\mathbf{\Sigma} = \begin{pmatrix} \Sigma^c & \Sigma^> \\ \Sigma^< & \Sigma^{\bar{c}} \end{pmatrix} \tag{4.21}$$

is the self-energy matrix and $\mathbf{G}^0$ is the Green function matrix in the absence of interaction.

In an inhomogeneous non-equilibrium system the Green functions depend on the pairs of variables $X = (r, t)$ and $X' = (r', t')$ separately, and not only on their difference $X - X'$ as in the equilibrium case. However, if the system is in the steady state or, more generally, when the hamiltonian does not depends on time in the Shrödinger representation, all Green functions depend only on the difference $t - t'$. We will also consider that the system is spatially homogeneous so that all functions depend only on the difference of coordinates $r - r'$ and then can be Fourier-transformed with respect to these variables

$$\mathbf{G} = \mathbf{G}^0 + \mathbf{G}^0\mathbf{\Sigma}\mathbf{G} \tag{4.22}$$

where the Green functions $\mathbf{G}$ and self-energies $\mathbf{\Sigma}$ are the matrices defined by Eqs. 4.19 - 4.21. The four Green functions thus defined are not independent. They are linearly related in a way that is obvious from their definitions

$$G^c + G^{\bar{c}} = G^< + G^> \tag{4.23}$$

In the same way

$$\Sigma^c + \Sigma^{\bar{c}} = -(\Sigma^< + \Sigma^>) \tag{4.24}$$

The set of equations Eqs.4.22 has the shortcoming of not taking into account the linear dependence of the Green functions (and self-energies). To avoid this problem one can use a linear transformation of the matrix $\mathbf{G}$ in order to reduce one of its elements to zero (using Eq.4.23). This is done with the aid of the formula

$$\tilde{\mathbf{G}} = R^{-1}\mathbf{G}R \tag{4.25}$$

where

$$R = \frac{1}{\sqrt{2}}\begin{pmatrix} 1 & 1 \\ -1 & 1 \end{pmatrix}, \quad R^{-1} = \frac{1}{\sqrt{2}}\begin{pmatrix} 1 & -1 \\ 1 & 1 \end{pmatrix} \tag{4.26}$$

It is easily seen that the transformed matrix can be expressed as

$$\tilde{\mathbf{G}} = \begin{pmatrix} 0 & G^A \\ G^R & F \end{pmatrix} \tag{4.27}$$

where

$$F = G^c + G^{\bar{c}} = G^< + G^> \tag{4.28}$$

When the matrices $\mathbf{G}^0$ and $\mathbf{\Sigma}$ are transformed in this way, the Dyson equation expressed in Eq.4.22 remains invariant

$$\tilde{\mathbf{G}} = \tilde{\mathbf{G}}^0 + \tilde{\mathbf{G}}^0\tilde{\mathbf{\Sigma}}\tilde{\mathbf{G}} \tag{4.29}$$

The transformed matrix $\mathbf{\Sigma}$ is

$$\tilde{\mathbf{\Sigma}} = R^{-1}\mathbf{\Sigma}R = \begin{pmatrix} \Omega & \Sigma^R \\ \Sigma^A & 0 \end{pmatrix} \tag{4.30}$$

using the notations

$$\Omega = \Sigma^c + \Sigma^{\bar{c}} \ , \quad \Sigma^R = \Sigma^c + \Sigma^> \ , \quad \Sigma^A = \Sigma^c + \Sigma^< \tag{4.31}$$

This can be proved by direct calculation, using the equation

$$\Sigma^c + \Sigma^{\bar{c}} = -(\Sigma^> + \Sigma^<) \tag{4.32}$$

Now expanding the transformed matrix Dyson equation we obtain the three following equations.

$$G^R = G^{0R} + G^{0R}\,\Sigma^R\,G^R \tag{4.33}$$
$$G^A = G^{0A} + G^{0A}\,\Sigma^A\,G^A \tag{4.34}$$
$$F = F^0 + G^{0R}\,\Sigma^R\,F + F^0\,\Sigma^A\,G^A + G^{0R}\,\Omega\,G^A \tag{4.35}$$

Two of them, the equations for G^R and G^A, are obviously complex conjugates. Eqs.4.33-4.35 provide a complete description of the system out of equilibrium.

In some cases it is convenient to work with minor, $G^<$, and major, $G^>$, Green functions as they carry information on the occupation of the impurity site. Here we give the Dyson equations for these functions [80]

$$G^< = \left[1 + G^R\Sigma^R\right] G_0^< \left[1 + G^A\Sigma^A\right] + G^R\Sigma^<G^A \tag{4.36}$$
$$G^> = \left[1 + G^R\Sigma^R\right] G_0^> \left[1 + G^A\Sigma^A\right] + G^R\Sigma^>G^A \tag{4.37}$$

For the problem considered in our work (Anderson model), at the starting time $t = -\infty$ the impurity and the leads are unconnected and separately at equilibrium, possibly with different chemical potentials. Formally, the hopping is turned on slowly, and non-equilibrium properties are evaluated long after the hopping is fully established, when a steady state has been achieved, but before the current flow has changed the chemical potentials in the leads.

Before applying the Keldysh formalism to the slave-boson Hamiltonian Eq.4.8, one has to overcome the difficulty associated with the constraint that the physical states are restricted to the Q = 1 ensemble. The problem is that one can not perform diagrammatic calculation in a restricted ensemble. If we use perturbation theory in V we have to enforce the constraint at each order, projecting out all contributions outside the physical subspace. In this sense the Dyson equation is not valid because it was derived for the unrestricted ensemble. The problem can be handled with the aid of a Lagrange multiplier or, as it is often named, a complex chemical potential.

We will start with the formal expression of the expectation values at non-equilibrium. In the Q = 1 ensemble, the expectation value of an operator **O** can be written as

$$\langle \mathbf{O} \rangle_{\mathrm{Q}=1} = \frac{1}{Z_{\mathrm{Q}=1}} \mathrm{Tr} \left\{ e^{-\beta(H_0 - \mu_L N_L - \mu_R N_R)} \, \delta_{\mathrm{Q},1} \, T_c \left[S_c \, \mathbf{O} \right] \right\} \tag{4.38}$$

where H_0 corresponds to the unconnected leads and dot and the partition function is given by

$$Z_{\mathrm{Q}=n} = \mathrm{Tr} \left\{ e^{-\beta(H_0 - \mu_L N_L - \mu_R N_R)} \, \delta_{\mathrm{Q},1} \, T_c \left[S_c \right] \right\} \tag{4.39}$$

with Q = 1. Since the hamiltonian commutes with the charge operator Q the projection on the Q = 1 ensemble can be performed by using a Kronecker δ-function in the statistical averages of Eq.4.38 and Eq.4.39. To relate the averages in the restricted ensemble and in the unrestricted ensemble, we represent the Kronecker a δ-function as an integral over a complex chemical potential

$$\delta_{\mathrm{Q},1} = \frac{\beta}{2\pi} \int_{-\pi/\beta}^{\pi/\beta} d\lambda \; e^{-i\beta\lambda(\mathrm{Q}-1)} \tag{4.40}$$

Incorporating this expression into Eq.4.38 we get

$$\langle \mathbf{O} \rangle_{\mathrm{Q}=1} = \frac{1}{Z_{\mathrm{Q}=1}} \, \frac{\beta}{2\pi} \int_{-\pi/\beta}^{\pi/\beta} e^{i\beta\lambda} d\lambda \, \mathrm{Tr} \left\{ e^{-\beta(H_0 - \mu_L N_L - \mu_R N_R + i\lambda Q)} \, T_c \left[S_c \, \mathbf{O} \right] \right\} \tag{4.41}$$

and then

$$\langle \mathbf{O} \rangle_{\mathrm{Q}=1} = \frac{1}{Z_{\mathrm{Q}=1}} \, \frac{\beta}{2\pi} \int_{-\pi/\beta}^{\pi/\beta} e^{i\beta\lambda} d\lambda \; Z_{GC} \langle \mathrm{O} \rangle_{GC} \tag{4.42}$$

with

$$\langle \mathbf{O} \rangle_{GC} = \frac{1}{Z_{GC}} \mathrm{Tr} \left\{ e^{-\beta(H_0 - \mu_L N_L - \mu_R N_R + i\lambda Q)} \, T_c \left[S_c \, \mathbf{O} \right] \right\} \tag{4.43}$$

and

$$Z_{GC} = \mathrm{Tr} \left\{ e^{-\beta(H_0 - \mu_L N_L - \mu_R N_R + i\lambda Q)} \, T_c \left[S_c \right] \right\} \tag{4.44}$$

where Eq.4.43 gives the average value of the operator **O** calculated in the grand canonical ensemble and Eq.4.44 gives the partition function of the grand canonical ensemble.

The average value of an operator **O** expressed in Eq.4.43 now obeys Wick's theorem and we can use conventional perturbation theory to calculate it. In principle, we can stop here, evaluate averages in the grand canonical ensemble, and project on the physical ensemble by a final integrating over the imaginary chemical potential. Further simplification can be gained, however, by noticing that the grand canonical partition function can be rewritten as a sum over partition functions in the canonical ensembles

$$Z_{GC} = \sum_{Q=0}^{\infty} Z_C(Q) e^{-i\beta\lambda Q} \tag{4.45}$$

By expanding the expression in the grand canonical ensemble as power series we get

$$\langle \mathbf{O} \rangle_{GC} = \langle \mathbf{O} \rangle_0 + \langle \mathbf{O} \rangle_1 e^{-i\beta\lambda} + \langle \mathbf{O} \rangle_2 e^{-2i\beta\lambda} + ... \tag{4.46}$$

$$Z_{GC} = Z(0) + Z(1) e^{-i\beta\lambda} + Z(2) e^{-2i\beta\lambda} + ... \tag{4.47}$$

Since Q = 0 corresponds to the case where there is no Anderson impurity all the physical operators satisfy the condition that $\langle \mathbf{O} \rangle_0 = 0$. Making use of this property we can write

$$\langle \mathbf{O} \rangle_{GC} = \langle \mathbf{O} \rangle_1 Z(0) e^{-i\beta\lambda} + \langle \mathbf{O} \rangle_1 Z(1) e^{-2i\beta\lambda} + \langle \mathbf{O} \rangle_2 Z(0) e^{-2i\beta\lambda} + ... \tag{4.48}$$

all the other terms in the expansion given by Eq.4.48 are of higher orders in $e^{-i\beta\lambda}$. If we perform this expansion for the average value in the restricted ensemble (Eq.4.42)

$$\langle \mathbf{O} \rangle_{\mathrm{Q}=1} = \frac{1}{Z_{\mathrm{Q}=1}} \frac{\beta}{2\pi} \int_{-\pi/\beta}^{\pi/\beta} e^{i\beta\lambda} d\lambda \, \left[\langle \mathbf{O} \rangle_1 Z(0) e^{-i\beta\lambda} + \left(\langle \mathbf{O} \rangle_1 Z(1) + \langle \mathbf{O} \rangle_2 Z(0) \right) e^{-2i\beta\lambda} + ... \right] \tag{4.49}$$

Then

$$\langle \mathbf{O} \rangle_{\mathrm{Q}=1} = \frac{1}{Z_{\mathrm{Q}=1}} \frac{\beta}{2\pi} \int_{-\pi/\beta}^{\pi/\beta} d\lambda \, \langle \mathbf{O} \rangle_1 Z(0) + \frac{1}{Z_{\mathrm{Q}=1}} \frac{\beta}{2\pi} \int_{-\pi/\beta}^{\pi/\beta} e^{-i\beta\lambda} \, d\lambda \, \{ \langle \mathbf{O} \rangle_1 Z(1) + \langle \mathbf{O} \rangle_2 Z(0) \} + ... \tag{4.50}$$

It is easy to see that the second term in the right-hand side of Eq.4.50 (and higher terms) vanishes since it corresponds to integration of periodic function on a period. So finally we have

$$\langle \mathbf{O} \rangle_{\mathrm{Q}=1} = \frac{Z_{\mathrm{Q}=0}}{Z_{\mathrm{Q}=1}} \langle \mathbf{O} \rangle_1 \tag{4.51}$$

where $Z(0) = Z_{Q=0}$ is the partition function in the absence of impurity. The average $\langle \mathbf{O} \rangle \equiv \langle \mathbf{O} \rangle_{GC}$ is given by Eq.4.43 and $\langle \mathbf{O} \rangle_1$ is the coefficient in front of of the term of order $\exp(-i\beta\lambda)$ in $\langle \mathbf{O} \rangle_{GC}$.
The important point is that $\langle \mathbf{O} \rangle_{GC}$ takes the standard form of diagrammatic perturbation theory since the traces in Eq.4.43 and in the partition function expressed in Eq.4.44 are over all states without any restriction. According to Eq.4.51, the non-equilibrium

expectation value of an operator $\mathbf{O}$ in the $\mathrm{Q} = 1$ ensemble results from two contributions: a normalization factor $Z_{\mathrm{Q}=0}/Z_{\mathrm{Q}=1}$, and a coefficient in front of $\exp(-i\beta\lambda)$ for the same operator in the grand canonical ensemble with complex chemical potential $i\lambda$. The normalization factor can be obtained using the identity

$$\langle \mathrm{Q} \rangle_{\mathrm{Q}=1} = 1 \tag{4.52}$$

which implies

$$\frac{Z_{\mathrm{Q}=1}}{Z_{\mathrm{Q}=0}} = \langle b^\dagger b \rangle_1 + \sum_\sigma \langle f_\sigma^\dagger f_\sigma \rangle_1 \tag{4.53}$$

Later, when we will introduce the noncrossing approximation we will come back to this question of how to project our all the contributions to the Dyson equation of the unphysical states.

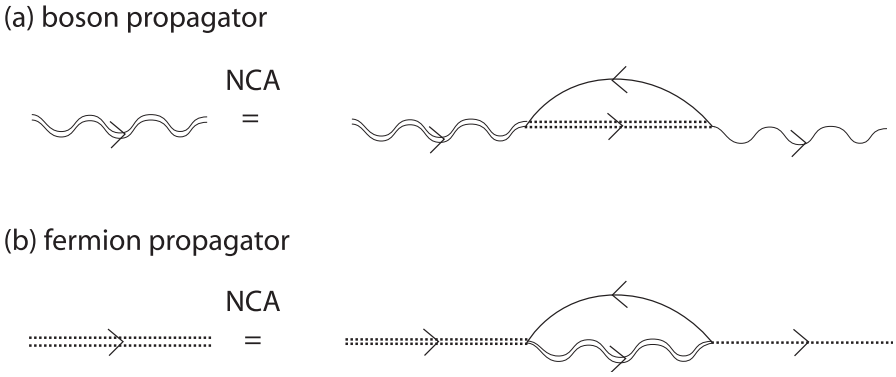

Figure 4.8: Diagrammatic representation of the coupled integral equations for summing diagrams with noncrossing lines (NCA integral equations). Double lines represent dressed propagators. These integral equations include all contributions $O(1)$ and $O(1/N)$ in the large-N expansion.

4.5 NCA for the Anderson model in the slave-boson representation

As it can be seen from Fig.4.5, at lowest order in perturbation theory the boson self-energy involves the fermion propagator while the fermion self-energy involves the boson propagator. By using the two relation self-consistently — the noncrossing approximation, see Fig.4.8 — one obtains a set of coupled integral equations, which can be solved numerically. Solving these self-consistent equations corresponds to summing a subset of diagrams to all orders in the hopping matrix element V. It can be shown that all diagrams of leading order in $1/N$, where N is the number of spin degrees of freedom, are included in this subset. For the case, $N = 2$, of interest for quantum dots, it was shown that the calculated equilibrium occupation number and susceptibility agree with the exact Bethe-Ansatz result to within 0.5%. The method is less accurate for the linear-response conductance. At worst, the linear-response conductance is overestimated by 15% [68], and this can be taken as a limit on the quantitative accuracy of the method.

The NCA coupled integral equations for boson and fermion propagators are presented diagrammatically in Fig.4.8. Each diagram is assigned to a single self-energy bubble, which is determined self-consistently, and the self-energies are iterated to all orders in hopping, V, via Dyson equations.

4.5.1 Application to the out-of-equilibrium regime

Here we present the noncrossing approximation generalized to nonequilibrium. The equations involve not only retarded Green functions, but also the minor and major ones, leading to slightly more complicated equations than at equilibrium.

We will start by calculating the density of states for the $U \to \infty$ Anderson model

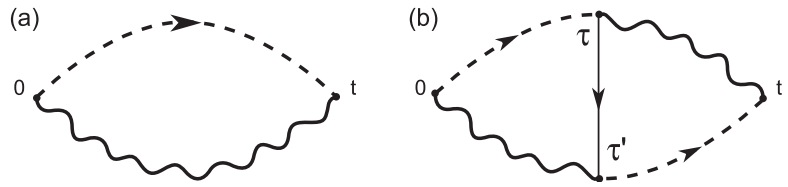

Figure 4.9: (a) A diagrammatic representation of the physical two-particle correlation function within the NCA. (b) The neglected vertex corrections are of order $O\big[(1/N)^2\big]$.

out of equilibrium. The density of states can be expressed in terms of retarded Green function

$$\rho_\sigma(\omega) = \frac{Z_{Q=0}}{Z_{Q=1}} \left[-\frac{1}{\pi} \mathtt{Im}\, G^{R\,(1)}_{\sigma,i\lambda}(\omega) \right] \tag{4.54}$$

where

$$G^{R\,(1)}_{\sigma,i\lambda}(t) = -i\theta(t) \langle \{ c_\sigma(t), c^\dagger_\sigma(0) \} \rangle^{(1)}_{i\lambda} \tag{4.55}$$

is the expectation value of the retarded electron Green function when the Lagrange multiplier $i\lambda$ is introduced to enforce the constraint Eq.4.9. Within the noncrossing approximation, the retarded Green function can be expressed in terms of the full propagators for bosons and fermions. In the slave-boson representation they can be expressed as a Green functions

$$G^{R\,(1)}_{\sigma,i\lambda}(t) = -i\theta(t) \langle \{ b^\dagger(t) f_\sigma(t), f^\dagger_\sigma(0) b(0) \} \rangle^{(1)}_{i\lambda} \tag{4.56}$$

The evaluation of $G^{R\,(1)}_{\sigma,i\lambda}$ functions would require, in principle, further diagrammatic expansion. In the noncrossing approximation, however, we can factorize the boson and fermion parts in Eq.4.56. This latter step corresponds to a neglect of vertex corrections (which are of order $O\,(1/N)^2$) in the expansion of the two-particle correlation functions and keeping only the lowest-order terms in the $1/N$ expansion. This type of diagrams is represented in Fig.4.9(b). So far we have obtained

$$G^{R\,(1)}_{\sigma,i\lambda}(t) = -i\theta(t) \left[\langle b^\dagger(t) b(0) \rangle \langle f_\sigma(t) f^\dagger_\sigma(0) \rangle + \langle f^\dagger_\sigma(0) f_\sigma(t) \rangle \langle b(0) b^\dagger(t) \rangle \right]^{(1)}_{i\lambda} \tag{4.57}$$

This expression can be written as

$$G^{R\,(1)}_{\sigma,i\lambda}(t) = -i\theta(t) \left[D^>(-t) G^<_{f\sigma}(t) - D^<(-t) G^>_{f\sigma}(t) \right] \tag{4.58}$$

where the following notations are used

$$\begin{aligned} D^{>}(t) &= -i\langle b(t)b^{\dagger}(0)\rangle_{i\lambda}^{(0)} \\ D^{<}(t) &= -i\langle b^{\dagger}(0)b(t)\rangle_{i\lambda}^{(1)} \\ G_{f\sigma}^{>}(t) &= -i\langle f_{\sigma}(t)f_{\sigma}^{\dagger}(0)\rangle_{i\lambda}^{(0)} \\ G_{f\sigma}^{<}(t) &= i\langle f_{\sigma}^{\dagger}(0)f_{\sigma}(t)\rangle_{i\lambda}^{(1)} \end{aligned} \tag{4.59}$$

Here it is important to note, that the leading term in the expansion in powers of $\exp(i\lambda\beta)$ is of zero order, $O(1)$ for the major Green functions both for boson and fermions, $G_{f\sigma}^{>}$ and $D^{>}$, and of order $O(\exp(i\lambda\beta))$ for the minor Green functions, $G_{f\sigma}^{<}$ and $D^{<}$. Since each term in Eq.4.58 contains exactly one minor operator, with one boson or fermion lowering operator acting directly to the right, the overall result for the retarded Green function is of order $O\left(\exp(i\lambda\beta)\right)$ as required.

Because the Hamiltonian is time-independent, it is simplest to evaluate the boson and fermion Green functions in the frequency representation. The physical density of states is then given by

$$\rho_{\sigma}(\omega) = \frac{1}{4\pi^2}\frac{Z_{Q=0}}{Z_{Q=1}}\int_{-\infty}^{\infty} d\omega' \left[D^{>}(\omega')G_{f\sigma}^{<}(\omega+\omega') - D^{<}(\omega')G_{f\sigma}^{>}(\omega+\omega')\right] \tag{4.60}$$

The minor and major Green functions can be found using Dyson equations. One can note that in the Dyson equations, additional terms involving minor and major boson and fermion Green functions on the uncoupled site is zero. This contribution can be written as

$$\left(1+G^{r}\Sigma^{r}\right)G_{0}^{<}\left(1+G^{a}\Sigma^{a}\right) \tag{4.61}$$

which can be written in the following way

$$G_{0}^{r}\left(1+G^{r}\Sigma^{r}\right)\frac{G_{0}^{<}}{G_{0}^{r}G_{0}^{a}}\left(1+G^{a}\Sigma^{a}\right)G_{0}^{a} \tag{4.62}$$

Using Dyson equations for G^r and G^a given in Eqs.4.33-4.34

$$\frac{|G^{r}|^2}{|G_{0}^{r}|^2}G_{0}^{<} = \frac{(\omega-\epsilon_0)^2}{(\omega-\tilde{\epsilon}_0)^2+\Gamma^2}\,2\pi i f(\omega)\delta(\omega-\epsilon_0) \tag{4.63}$$

where $\tilde{\epsilon}_0$ corresponds to the renormalization level energy and $f(\omega)$ is the Fermi distribution function. This term thus equals to zero. As we will see later the fermion minor Green function contains information about the occupation of the site. This property, in fact, reflects the loss of memory of the initial occupation of the site in the coupled system. The Dyson equations can be written as

$$D^{\lessgtr}(\omega) = D^{r}(\omega)\Pi^{\lessgtr}(\omega)D^{a}(\omega) \tag{4.64}$$

$$G_{f\sigma}^{\lessgtr}(\omega) = G_{f\sigma}^{r}(\omega)\Sigma_{f\sigma}^{\lessgtr}(\omega)G_{f\sigma}^{a}(\omega) \tag{4.65}$$

where the self energies are given by

$$\Pi^{\lessgtr}(\omega) = -\frac{i}{2\pi}\int_{-\infty}^{+\infty} d\omega' \sum_{\sigma,k\in L,R} |V_{k\sigma}|^2 g^{\gtrless}_{k\sigma}(\omega'-\omega) G^{\lessgtr}_{f\sigma}(\omega') \tag{4.66}$$

$$\Sigma^{\lessgtr}_{f\sigma}(\omega) = \frac{i}{2\pi}\int_{-\infty}^{+\infty} d\omega' \sum_{k\in L,R} |V_{k\sigma}|^2 g^{\lessgtr}_{k\sigma}(\omega-\omega') D^{\lessgtr}(\omega') \tag{4.67}$$

In Eq.4.66-Eq.4.67 the functions $g(\omega)$ are the Green functions of conduction electrons in the leads not coupled to the site.

$$g^{>}_{k,\sigma} = -2\pi i[1-f_{L,R}(\omega)]\delta(\omega-\epsilon_{k,\sigma}) \tag{4.68}$$

$$g^{<}_{k,\sigma} = 2\pi i f_{L,R}(\omega)\delta(\omega-\epsilon_{k,\sigma}) \tag{4.69}$$

It would be correct to include self-energies for the Green functions of the electrons in the leads, which would correspond to calculating the full propagator in the presence of slave fermions and bosons. The self-energy corrections to the conduction electron propagators includes the fermion-boson loop, which brings an extra unwanted factor of $\exp(-i\beta\lambda)$, and will be projected out when final integration over λ is done. As a consequence, one always works with bare conductance electron propagators, which again, is not what one gets initially from the unprojected NCA equations and is not an additional approximation.

Several other relations are required to close the equations for the non-crossing approximation. The retarded Green functions for the boson and fermions in Eq.4.64-Eq.4.65 are given by

$$D^r(\omega) = \frac{1}{\omega - \Pi^r(\omega)} \tag{4.70}$$

$$G^r_{f\sigma}(\omega) = \frac{1}{\omega - \epsilon_\sigma - \Sigma^r_{f\sigma}(\omega)} \tag{4.71}$$

where the retarded self-energies are Hilbert transforms of the major self-energies

$$\Pi^r(\omega) = \frac{i}{2\pi}\int_{-\infty}^{+\infty} d\omega' \frac{\Pi^{>}(\omega')}{\omega-\omega'+i\eta} \tag{4.72}$$

$$\Sigma^r_{f\sigma}(\omega) = \frac{i}{2\pi}\int_{-\infty}^{+\infty} d\omega' \frac{\Sigma^{>}_{f\sigma}(\omega')}{\omega-\omega'+i\eta} \tag{4.73}$$

The advanced Green functions D^a and $G^a_{f\sigma}$ in Eq.4.64-Eq.4.65 are complex conjugates of the retarded Green functions D^r and $G^r_{f\sigma}$. By definition, all retarded Green functions and self-energies can be written as a difference of major and minor Green functions

$$G^r(t) = \theta(t)\left(G^{>}(t) - G^{<}(t)\right) \tag{4.74}$$

The leading term in the expansion in powers of $e^{-i\beta\lambda}$ of the minor Green function is $O(e^{-i\beta\lambda})$ so it must be dropped from the expression for the retarded Green functions Eq.4.74 which are $O(1)$. Further, by taking the Fourier transform of the latter equation we will get the useful relations

$$\begin{aligned} D^{>}(\omega) &= 2i\ \mathtt{Im}\, D^{r}(\omega) \\ G^{>}_{f\sigma}(\omega) &= 2i\ \mathtt{Im}\, G^{r}_{f\sigma}(\omega) \end{aligned} \tag{4.75}$$

To derive these relations, we have used the property that the major Green functions have only imaginary component $G^{>}_{f\sigma}(\omega) = i\ \mathtt{Im}\, G^{>}_{f\sigma}$. The same set of relations holds for the boson and fermion self-energies

$$\begin{aligned} \Pi^{>}(\omega) &= 2i\ \mathtt{Im}\, \Pi^{r}(\omega) \\ \Sigma^{>}_{f\sigma}(\omega) &= 2i\ \mathtt{Im}\, \Sigma^{r}_{f\sigma}(\omega) \end{aligned} \tag{4.76}$$

Once we know the imaginary parts of the retarded self-energies, we can find their real parts using Kramers-Kronig relation

$$\mathtt{Re}\, F(\omega) = -\frac{1}{\pi}\ \mathtt{P.v.} \int_{-\infty}^{+\infty} \frac{\mathtt{Im}\, F(\omega')}{\omega - \omega'}\, d\omega' \tag{4.77}$$

For example the retarded fermion self-energy is

$$\begin{aligned} \Sigma^{r}_{f\sigma}(\omega) = \mathtt{Re}\, \Sigma^{r}_{f\sigma}(\omega) + i\, \mathtt{Im}\, \Sigma^{r}_{f\sigma}(\omega) = \\ \frac{i}{2\pi}\left(\mathtt{P.v.} \int_{-\infty}^{+\infty} \frac{\Sigma^{>}_{f\sigma}(\omega')}{\omega - \omega'}\, d\omega' - \pi i \int_{-\infty}^{+\infty} \Sigma^{>}_{f\sigma}(\omega')\delta(\omega - \omega')\, d\omega' \right) = \\ \frac{i}{2\pi} \int_{-\infty}^{+\infty} \frac{\Sigma^{>}_{f\sigma}(\omega')\, d\omega'}{\omega - \omega' + i\eta} \end{aligned} \tag{4.78}$$

What gives the expression Eq.4.73. Eq.4.72 can be obtained in an analogous way.

These equations form a closed set of equations for the noncrossing approximation from which all the unwanted contributions in the $e^{-i\beta\lambda}$ expansion are projected out. This set of equations can be solved iteratively. In practice, one starts with an initial guess for the major boson Green function, $D^{>}(\omega)$. Then the major fermion self-energy , $\Sigma^{>}_{f\sigma}(\omega)$, can be calculated using Eq.4.67. Once $\Sigma^{>}_{f\sigma}(\omega)$ is calculated, the retarded self-energy is obtained by using Eq.4.73. Then, the retarded fermion Green function can be easily obtained from Eq.4.71. The values of the major fermion Green function, Eq.4.75, can be used in a parallel way to obtain an improved major boson Green function, $D^{>}(\omega)$. This procedure is iterated to convergence. At the end of the procedure we obtain the retarded boson and fermion Green functions. A similar procedure is then followed for the minor Green functions. Following the initial guess for $D^{<}(\omega)$, the fermion self-energies $\Sigma^{<}_{f\sigma}(\omega)$ are obtained from Eq.4.67, and $G^{<}_{f\sigma}(\omega)$ are determined from Eq.4.65. Then by

combining Eq.4.66 and Eq.4.64 one obtains the values of minor boson Green function $D^{<}(\omega)$. The steps are repeated for $D^{<}(\omega)$, and the process iterated to convergence. Finally, the physical density of states $\rho_\sigma(\omega)$ is evaluated by the convolution of the boson and fermion Green functions (Eq.4.60).

In principle one can stop here and evaluate $\rho_\sigma(\omega)$ numerically in or out of equilibrium. Nevertheless, an important simplification of the self-consistent procedure can be made.

Following the work performed for equilibrium case, one can take the energy dependence of the couplings between the reservoirs and the site in the dot to the leads to be Lorentzian

$$\Gamma_\sigma^{L(R)}(\omega) = 2\pi \sum_{k\in L(R)} |V_{k\sigma}|^2 \delta(\omega - \epsilon_{k\sigma}) \equiv \Gamma_{0\sigma}^{L(R)} \frac{W^2}{(\omega-\epsilon_0)^2 + W^2} \tag{4.79}$$

where W is the bandwidth in the leads. The choice of a Lorentzian form allows a simplification of the self-consistent equations. In general, to iterate the noncrossing approximation equations, the retarded self-energies for the bosons and fermions must be evaluated by double integrals over the major Green function. For the Lorentzian coupling, however, one of these integrals can be performed analytically. Combining Eqs.4.66-4.67 with Eqs.4.72-4.73, the boson retarded self-energy can be written as a single integral

$$\Pi^r(\omega) = \sum_\sigma \sum_{L,R} \int_{-\infty}^{+\infty} d\omega' H_\sigma^{L(R)}(\omega' - \omega) G^{>}(\omega') \tag{4.80}$$

with the kernels

$$\begin{aligned} H_\sigma^{L(R)}(\omega) = \frac{1}{(2\pi)^2}\Gamma_\sigma^{L(R)}(\omega) \Bigg[\pi\, f_{L(R)}(\omega) + i\,\mathtt{Re}\left(\Psi\left(\frac{1}{2} - \frac{i\beta(\omega-\mu_{L(R)})}{2\pi}\right)\right. \\ \left. -\Psi\left(\frac{1}{2} + \frac{\beta\left[W - i(\epsilon_{L(R)} - \mu_{L(R)})\right]}{2\pi}\right)\right) \\ -i\frac{\omega - \epsilon_{L(R)}}{W}\left\{\frac{\pi}{2} + \mathtt{Im}\left[\frac{1}{2} + \frac{\beta\left[W - 1(\epsilon_{L(R)} - \mu_{L(R)})\right]}{2\pi}\right]\right\}\Bigg] \end{aligned} \tag{4.81}$$

where β is the inverse temperature and $\Psi(z)$ is the Digamma function. The fermion retarded self-energies can be written as single integrals

$$\Sigma_{f\sigma}^r(\omega) = \sum_{L,R} \int_{-\infty}^{+\infty} d\omega'\, K_\sigma^{L(R)}(\omega - \omega') D^{>}(\omega') \tag{4.82}$$

with the kernels

$$H_\sigma^{L(R)}(\omega) = \frac{1}{(2\pi)^2}\Gamma_\sigma^{L(R)}(\omega)\left[[1-\pi\, f_{L(R)}(\omega)] + i\,\mathtt{Re}\left(\Psi\left(\frac{1}{2} - \frac{i\beta(\omega-\mu_{L(R)})}{2\pi}\right)\right.\right.$$
$$\left. -\Psi\left(\frac{1}{2} + \frac{\beta\left[W - i(\epsilon_{L(R)} - \mu_{L(R)})\right]}{2\pi}\right)\right) \quad (4.83)$$
$$\left. +i\frac{\omega-\epsilon_{L(R)}}{W}\left\{\frac{\pi}{2} - \mathtt{Im}\left[\frac{1}{2} + \frac{\beta\left[W - \imath(\epsilon_{L(R)} - \mu_{L(R)})\right]}{2\pi}\right]\right\}\right]$$

Since the major Green functions and self-energies are just the imaginary parts of the corresponding retarded Green functions (Eq.4.75), the above equations together with relations Eq.4.70 and Eq.4.71 between the retarded Green functions and self-energies, form a closed set. In practice, we start with an initial guess for the major boson Green function and then iterate the equations to convergence. The accuracy of the result can be checked by comparing to the sum rules on the boson and fermion retarded Green functions

$$\int_{-\infty}^{+\infty} d\omega \left[-\frac{1}{\pi}\,\mathtt{Im}\, D^r(\omega)\right] = 1 \quad (4.84)$$
$$\int_{-\infty}^{+\infty} d\omega \left[-\frac{1}{\pi}\,\mathtt{Im}\, G_{f\sigma}^r(\omega)\right] = 1$$

Once the retarded Green functions are calculated, a separate iterative loop is required to evaluate the minor Green functions and energies. Equations Eq.4.66 and Eq.4.67 for the boson and fermion self-energies can be rewritten as

$$\Pi^<(\omega) = -\frac{1}{2\pi}\sum_\sigma\sum_{L,R}\int_{-\infty}^{+\infty} d\omega'\,\Gamma_\sigma^{L(R)}(\omega'-\omega)\left[1 - f_{L(R)}(\omega'-\omega)\right] G_{f\sigma}^<(\omega') \quad (4.85)$$

and

$$\Sigma_{f\sigma}^<(\omega) = -\frac{1}{2\pi}\sum_{L,R}\int_{-\infty}^{+\infty} d\omega'\,\Gamma_\sigma^{L(R)}(\omega-\omega') f_{L(R)}(\omega-\omega') D^<(\omega') \quad (4.86)$$

Together with Eq.4.64 and Eq.4.65, these equations form a closed set of equation for the minor Green function and self-energies. Again, following an initial guess for the boson minor Green function, these equations are iterated to convergence. Since the minor Green functions are defined up to an overall normalization factor, to check the convergence it is necessary to monitor a normalized quantity. The most natural choice is, for simplicity, to monitor the occupation number for each spin state

$$\langle n_\sigma\rangle = \frac{Z_{Q=0}}{Z_{Q=1}}\left[-\frac{i}{2\pi}\int_{-\infty}^{+\infty} d\omega\, G_{f\sigma}^<(\omega)\right] \quad (4.87)$$

where the normalization is provided by the ratio of partition functions, which from Eq.4.49 is given by

$$\frac{Z_{Q=1}}{Z_{Q=0}} = \frac{i}{2\pi}\int_{-\infty}^{+\infty} d\omega \left[D^{<}(\omega) - \sum_{\sigma} G^{<}_{f\sigma}(\omega) \right] \tag{4.88}$$

Finally, the accuracy of the calculations can be verified by the sum rule for the infinite U Anderson model relating the total density of states of one spin state to the occupancy of all the other spin states. In the case of interest (only two spin states $\sigma =\uparrow$ and $\sigma =\downarrow$) the infinite integral of the density of states is given by

$$\int_{-\infty}^{+\infty} \rho_{\sigma}(\omega) d\omega = \frac{1}{4\pi^2}\frac{Z_{Q=0}}{Z_{Q=1}} \int_{-\infty}^{+\infty}\int_{-\infty}^{+\infty} \left(D^{>}(\omega') G^{<}_{f\sigma}(\omega+\omega') - D^{<}(\omega') G^{>}_{f\sigma}(\omega+\omega') \right) d\omega' d\omega \tag{4.89}$$

which can be written as

$$\frac{1}{4\pi^2}\frac{Z_{Q=0}}{Z_{Q=1}} \int_{-\infty}^{+\infty} d\omega' \left(D^{>}(\omega') \int_{-\infty}^{+\infty} d\omega\, G^{<}_{f\sigma}(\omega+\omega') - D^{<}(\omega') \int_{-\infty}^{+\infty} d\omega\, G^{>}_{f\sigma}(\omega+\omega') \right) \tag{4.90}$$

The integration over ω can be performed independently of the integration over ω' using the substitution $\omega'' = \omega + \omega'$. Since the major fermion Green function is just the imaginary part of the retarded Green function, from the sum rule Eq.4.84 we get

$$\int_{-\infty}^{+\infty} d\omega\, G^{>}_{f\sigma}(\omega+\omega') = -2\pi i \tag{4.91}$$

Together with the expression for the occupation number per spin Eq.4.87, one gets

$$\int_{-\infty}^{+\infty} \rho_{\sigma}(\omega) d\omega = n_{\sigma} + \frac{i}{2\pi}\frac{Z_{Q=0}}{Z_{Q=1}} \int_{-\infty}^{+\infty} D^{<}(\omega')\, d\omega' \tag{4.92}$$

where the normalization factor is given by Eq.4.88. Under the notations

$$\mathbf{F} = \int_{-\infty}^{+\infty} F(\omega)\, d\omega \tag{4.93}$$

the latter expression can be rewritten as

$$\int_{-\infty}^{+\infty} \rho_{\sigma}(\omega) d\omega = -\frac{\mathbf{G}_{\sigma}}{\mathbf{D}-\mathbf{G}_{\sigma}-\mathbf{G}_{-\sigma}} + \frac{\mathbf{D}}{\mathbf{D}-\mathbf{G}_{\sigma}-\mathbf{G}_{-\sigma}} = \frac{-\mathbf{G}_{\sigma}+\mathbf{D}}{\mathbf{D}-\mathbf{G}_{\sigma}-\mathbf{G}_{-\sigma}} \tag{4.94}$$

after some not complicated algebra this equation becomes

$$1 + \frac{\mathbf{G}_{-\sigma}}{\mathbf{D}-\mathbf{G}_{\sigma}-\mathbf{G}_{-\sigma}} \tag{4.95}$$

$$\int_{-\infty}^{+\infty} d\omega\, \rho_\sigma(\omega) = 1 - \sum_{\sigma' \neq \sigma} \langle n_{\sigma'} \rangle \tag{4.96}$$

This relation is always satisfied to within 0.001% in our numerical calculations.

4.6 Numerical solution of the NCA equations

In this section we describe the numerical solution of the NCA equations presented earlier in details.

In the calculations that we have performed we used for the value of the bandwidth $W = 60\,\Gamma$. The Green functions are evaluated on the range $[-10W\,;10W]$. All energies and temperatures are taken in units of the total coupling strength to the leads, Γ, and are counted from the bare level energy, ϵ_0. We use an homogenous mesh with a number of points $N = 2^{20}$. This choice is imposed by the fast fourier transform (FFT) procedures which we use to calculate the convolution and the correlation -type integrals.

The algorithm is made of three main steps: the first step is the loop consisted in calculating the retarded (boson and fermion) Green functions; the second one is the loop consisted in calculating the minor (boson and fermion) Green function and finally the third step is built for the final reconstruction of the retarded Green function of physical electrons from auxiliary slave bosons and fermions Green functions.

The closed sets of equations were given in the previous section. Each loop starts with an initial guess for the corresponding (major or minor) boson Green function. We find it appropriate to start with the following expression for the unperturbed major Green function:

$$D_0^{>}(\omega) = -2i\,\mathtt{Im}\,D_0^r(\omega) = -2i\frac{\Gamma_0}{\omega^2+\Gamma_0^2} \tag{4.97}$$

The major Green functions are purely imaginary functions. From a technical point of view we prefer to rewrite all the equations in order to work instead with real functions.

Once the initial guess for the major Green function is made the iterations can start. Any cycle of convergence loop provides us with an improved boson major Green function. The convergence criterium is then tested. We choose to estimate the following integral

$$\int_{-\infty}^{+\infty} \left|D_{n-1}^{>}(\omega) - D_n^{>}(\omega)\right|\, d\omega \;<\; \varepsilon_r \tag{4.98}$$

where n is the number of iterations and ε_r is the required precision. In the first loop corresponding to the calculation of the retarded Green function we usually take $\varepsilon_r \sim 10^{-10}$. Most of the time, from 3 to 6 iterations were required to reach convergence. As soon as the condition Eq.4.98 is fulfilled one obtains the retarded boson and fermion Green functions, required to calculate the minor Green functions. The accuracy of the retarded Green functions that are obtained can be tested by use of the sum rules. Usually the sum rules are satisfied with an accuracy better than 0.1% .

The second loop corresponding to the calculation of the minor Green functions starts with an initial guess for the boson Green function. We have used the same initial guess as for the first loop, Eq.4.97. To control the convergence in this loop, one needs to examine any physical quantity since the normalization is not fixed for the minor Green functions and the condition Eq.4.98 cannot be applied. The simplest choice, in this case, is to monitor the occupation per spin. Within the required precision of $\varepsilon_< \sim 10^{-6}$ the

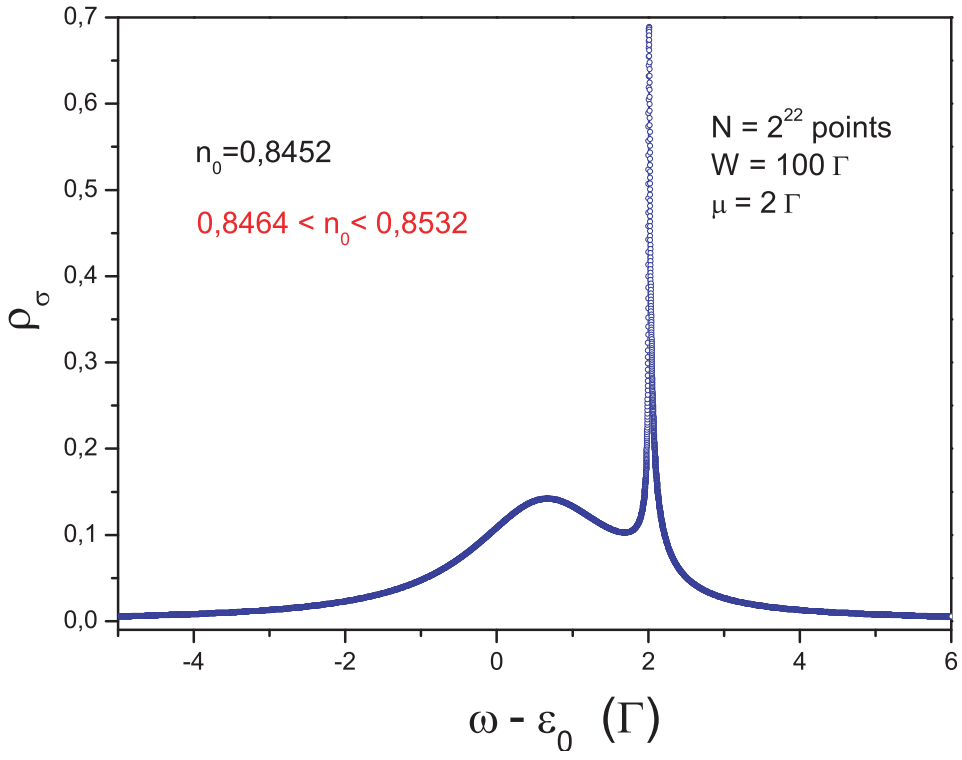

Figure 4.10: Energy dependence of the density of states, $\rho_\sigma(\omega)$ at equilibrium. Draw at $T = 0.005\,\Gamma$, $\mu_L = \mu_R = 2\,\Gamma$, $W = 100\,\Gamma$, the number of points used is $N = 2^{22}$. The total occupation number is found to be close to the exact value.

solution converges generally after 5 or 7 iterations. The numerical error in calculating the minor Green functions includes the error generated in the calculation of the retarded Green functions.

At a final step we calculate the physical density of states, $\rho_\sigma(\omega)$. The final accuracy is controlled by the sum rule for the infinite-U model relating the density of states per spin to the occupancy of all the other spin states (i.e. to the occupation of the opposite spin state in the case considered). This relation is always satisfied to within 0.01%. In order to obtain the full retarded Green function of physical electrons one has to calculate its real part. Relating the density of states to the imaginary part of the retarded Green function, the real part can be obtained by using Kramers-Kronig relations.

In Fig.4.10 the energy dependence of the density of states is reported at $T = 0.005\,\Gamma$. This curve was drawn using the same set of parameters as in Ref.[65] to ensure that our numerical procedures work correctly. Usually we use the lower value of the bandwidth, W, in order to use fewer points that make the calculations easier. The evolution of the density of states with temperature is reported in Fig.4.11. The height of the sharp peak at the Fermi energy is gradually suppressed when temperature is increased and the peak completely disappears at $T = 0.8\,\Gamma$.

The non-equilibrium density of states is shown in Fig.4.12. The applied bias voltage, $eV_{SD} = 0.2\,\Gamma$, splits the Kondo peak into two peaks with strongly reduced height, each of

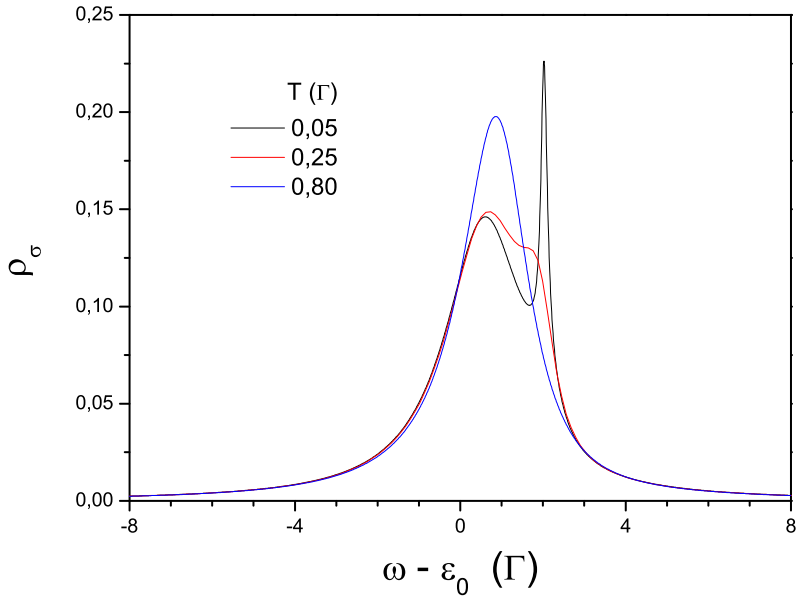

Figure 4.11: Temperature dependence of the equilibrium density of states. To calculate these curves we used: $W = 60\,\Gamma$, $\mu_L = \mu_R = 2\,\Gamma$, $N = 2^{20}$.

these two peaks taking placed at the chemical potentials μ_L and μ_R. As the temperature is increased the peaks merge loosing height and finally disappears at $T = 0.5\,\Gamma$. For larger values of the bias voltage, Fig.4.13, the height of the peaks is drastically reduced even at very low temperature, $T = 0.005\,\Gamma$. Increasing temperature, as usual, leads to a suppression of the peaks.

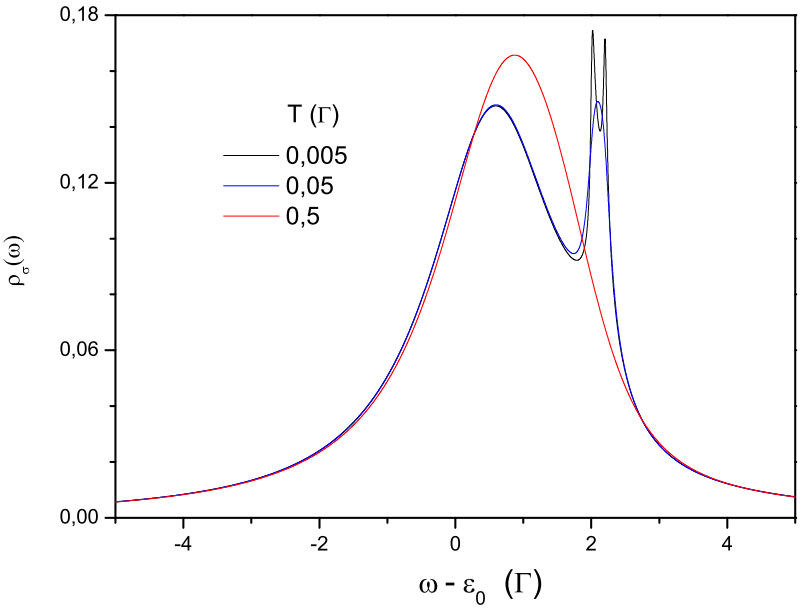

Figure 4.12: Temperature dependence of the non-equilibrium density of states at $eV_{SD} = 0.4\,\Gamma$ (for $W = 60\,\Gamma$, $\mu_L = 2.0\,\Gamma$, $\mu_R = 2.2\,\Gamma$ and $N = 2^{20}$).

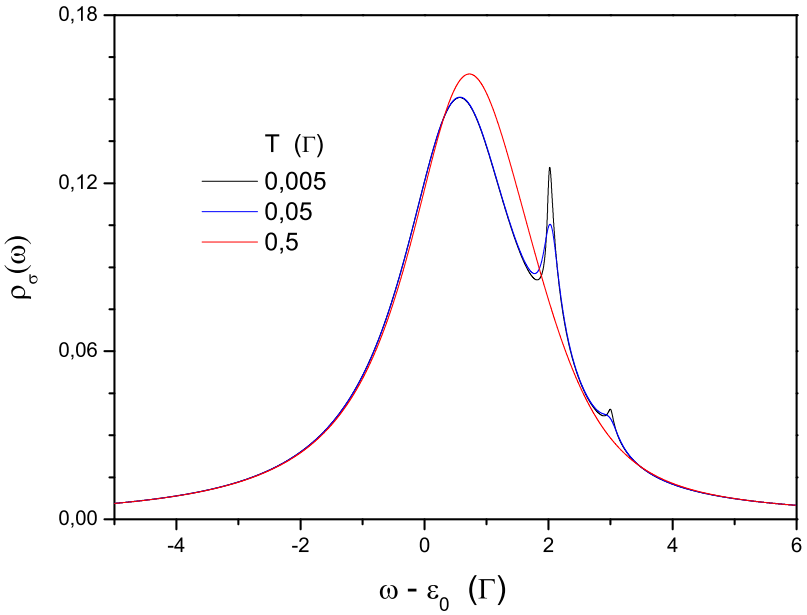

Figure 4.13: Temperature dependence of the non-equilibrium density of states at $eV_{SD} = 1\,\Gamma$ (for $W = 60\,\Gamma$, $\mu_L = 2\,\Gamma$, $\mu_R = 3\,\Gamma$ and $N = 2^{20}$).

4.7 Transmission phase shift of a quantum dot out of equilibrium

In this section we present the study of the effect of finite voltage and temperature on the transmission phase shift of a quantum dot. The non-equilibrium Keldysh formalism together with non-crossing approximation applied to the infinite-U Anderson model allows one to go beyond the linear-response description. We discuss some particular features of the out-of-equilibrium behavior of the transmission phase shift.

The section is organized as follows. First we explain the basic idea of phase shift measurements at equilibrium. In an analogous way, using the Landauer-Buttiker formalism, we define the quantity to be measured in the non-equilibrium setup and derive the expression for this quantity in terms of the localized electron retarded Green function. Then, we present the model and list the methods that we used to solve the problem. The descriptions of the methods themselves were given in the precedent sections. Next, we present the results of our study for the occupation number and the phase shift. We end up this section by giving a brief conclusions.

4.7.1 Phase shift

At equilibrium the transmission phase shift can be calculated in an open Aharonov-Bohm interferometers under the assumptions that (i) the transport through the quantum dot is fully coherent and (ii) the source and the drain do not drive the quantum dot out of equilibrium. In this case the source-drain conductance, G_{SD}, can be calculated using the Landauer formula

$$G_{SD} \propto |t_{ref} e^{i\theta} + t_{QD} e^{i\delta}|^2 \tag{4.99}$$

The further assumptions are made: (iii) only one conduction mode carries the current between source and drain, (iv) both paths are geometrically equivalent and (v) due to the open structure of the interferometer there is no multiple traversal of the ring, which makes the set-up equivalent to the double-slit geometry experiment. The quantities t_{ref} and t_{QD} are chosen to be real, $\theta = 2\pi\Phi/\Phi_0$ is the Aharonov-Bohm phase and δ is the transmission phase shift of the quantum dot. The oscillating part of the conductance with the magnetic field is written as

$$\delta G_{SD} \propto t_{ref} t_{QD} \cos(\theta - \delta) \tag{4.100}$$

where the quantity δ is measured experimentally. The phase shift is the deviation of the Aharonov-Bohm conductance oscillations as a function of the gate voltage. The oscillating term in the expression of the conductance comes from the interference between the electron electronic wave functions transmitted through the reference arm and the arm in which the quantum dot is embedded.

At large bias voltages or/and high temperatures the assumptions (i), (ii) and (iii) are not valid: the transport through the dot has an incoherent component, the dot has a non-equilibrium density of states and several modes carry the current. At zero

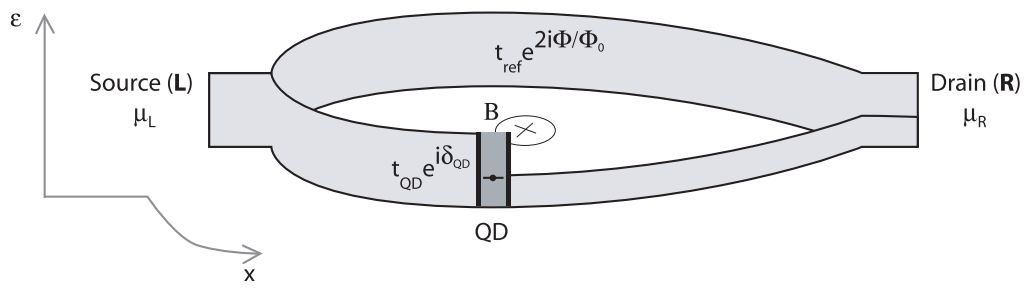

Figure 4.14: Sketch of an Aharonov-Bohm interferometer ring. The electron from the source (μ_L) can reach the drain (μ_R) through either the upper (reference) or lower arm which the quantum dot is embedded in.

temperature the current through the dot is carried by the electrons in the energy layer eV_{SD}. In order to find out which phase (shift) is measured at the experiment, we need to calculate the oscillating part of the source-drain current with the magnetic field. Then again, as in the equilibrium, the transmission phase shift is identified with the shift of the periodic A.B. oscillations with the gate voltage.

We also consider that there is no energy-relaxation process inside the ring. Electrons should be in the same quantum state to interfere, the electron at different energies strictly speaking do not participate in the formation of the interference pattern. If we denote $i(\epsilon)\Delta\epsilon$ the current carried by the electrons in the energy interval $\epsilon \rightarrow \epsilon + \Delta\epsilon$ in the limit $\Delta\epsilon \rightarrow 0$, the net drain current can be written as an integral over the energy [69]

$$I_{SD} = \int i(\epsilon)\, d\epsilon \tag{4.101}$$

where the current $i(\epsilon)$ can be calculated using the Landauer-Buttiker formalism

$$i(\epsilon) = \frac{2e}{h}\mathbf{T}(\epsilon)\left[f_L(\epsilon) - f_R(\epsilon)\right] \tag{4.102}$$

Note that this formula, Eq.4.101, goes beyond the linear response theory. The expression for the current per energy, $i(\epsilon)$, given by Eq.4.102 takes into account finite temperature and bias voltage effects. The linear response theory can be applied to the case when the transmission probability, $\mathbf{T}(\epsilon)$, is approximately constant over the energy range where transport occurs and can be assumed to be unaffected by the bias. In the equilibrium, $\mu_L \approx \mu_R \approx \mu$, and at low temperatures, $T \rightarrow 0$, one can simplify Eq.4.102 by using a Taylor's series expansion

$$f_L(\epsilon) - f_R(\epsilon) \approx (\mu_L - \mu_R)\frac{\partial f}{\partial \mu} = -(\mu_L - \mu_R)\frac{\partial f}{\partial \epsilon} \tag{4.103}$$

At low temperatures

$$\frac{\partial f}{\partial \epsilon} \approx \delta(\epsilon - \mu) \tag{4.104}$$

And one obtains the linear response source-drain current

$$I_{SD} = \frac{\mu_L - \mu_R}{e} G_{SD} \tag{4.105}$$

where G_{SD} is the linear response Landauer conductance.

From the above derivation it seems that the response should be linear if the bias $(\mu_L - \mu_R)$ is much less than T, so that the Taylor's series expansion is accurate. We find it useful to note that this is a sufficient but not a necessary condition (otherwise there would be no linear response at $T = 0$). A general criterion for linear response can be obtained by rewriting the general expression for the current Eq.4.101-Eq.4.102 in the form

$$I = \frac{1}{e} \int_{\mu_R}^{\mu_L} \hat{G}(\epsilon')\, d\epsilon' \tag{4.106}$$

where the conductance function $\hat{G}(\epsilon)$ is defined as

$$\hat{G}(\epsilon') = \frac{2e^2}{h} \int_{-\infty}^{+\infty} d\epsilon\, T(\epsilon) \frac{d}{d\epsilon} f(\epsilon - \epsilon') \tag{4.107}$$

This expression shows that the current will respond linearly if the conductance function $\hat{G}(\epsilon)$ is independent of energy in the energy range $\mu_L > \epsilon > \mu_R$.

Here we will assume that the transmission amplitude through the reference arm t_{ref} does not depend on the energy of the electron as well as the Aharonov-Bohm phase $\theta = 2\pi\Phi/\Phi_0$. The expression Eq.4.102 is valid if there is no inelastic scattering off the dot so that $\mathbf{T}_{L\to R} = \mathbf{T}_{R\to L}$. This is not true at finite temperatures and voltages ($\sim T_K$): when the current has both coherent and incoherent components. In order to calculate the net current through the dot the corrections (for example due to interactions inside the scattering region) should be taken into account. The net current through the interacting quantum dot out of equilibrium can be written as [67]

$$I_{QD} = \frac{e}{h} \int_{-\infty}^{+\infty} [f_L(\epsilon) - f_R(\epsilon)]\, \mathsf{Tr}\left\{G^a \Gamma^R G^r \Gamma^L \Sigma_0^{-1} \Sigma\right\} \tag{4.108}$$

where $\Sigma = \Sigma^r - \Sigma^a$ and Σ_0, the self-energy for the non-interacting case, is equal to $-i(\Gamma^L + \Gamma^R)$. The coherent component of the current is due to the "non-interacting" scattering off the dot. The incoherent contribution to the net current does not contribute to the interference pattern, it changes only the mean value of the current through the ring and so has no interest for us. Taking into account only the Σ_0 term from $\Sigma = \Sigma_0 + \Sigma^i$ and inserting it into Eq.4.108 we get

$$I_{QD} = \frac{e}{h} \int_{-\infty}^{+\infty} [f_L(\epsilon) - f_R(\epsilon)]\, \mathsf{Tr}\left\{G^a \Gamma^R G^r \Gamma^L\right\} \tag{4.109}$$

The coherent part of the current has the usual Landauer form

$$I_{QD} = \frac{e}{h} \int_{-\infty}^{+\infty} [f_L(\epsilon) - f_R(\epsilon)]\, \mathsf{Tr}\left\{t^\dagger t\right\} \tag{4.110}$$

where $t = c\Gamma^L G^r$ is the transmission amplitude an the phase factor $|c|^2 = 1$ does not effect the current.

The energy-dependent ring transmission probability, $\mathbf{T}(\epsilon)$, can be written as

$$\mathbf{T}(\epsilon) = |t_{ref} e^{i\theta} + t_{QD}(\epsilon) e^{i\delta(\epsilon)}|^2 \tag{4.111}$$

The total (coherent) current then can be calculated using Eq.4.101

$$I_{SD} = \frac{2e}{h} \int |t_{ref} e^{i\theta} + t_{QD}(\epsilon) e^{i\delta(\epsilon)}|^2 \left[f_L(\epsilon) - f_R(\epsilon) \right] \, d\epsilon \tag{4.112}$$

Here we are interested only in the oscillating part of the drain current. The square of the magnitude of the coherent sum of the transmission amplitudes in the Eq.4.112 gives two field-independent contributions, which correspond to the transmission through each arm of the interferometer plus an interference term. The oscillating part of the drain current with the magnetic field is given by

$$\delta I_{SD}(\theta) = \frac{4e}{h} t_{ref} \int t_{QD}(\epsilon) \cos\big(\theta - \delta(\epsilon)\big) \left[f_L(\epsilon) - f_R(\epsilon) \right] \, d\epsilon \tag{4.113}$$

It is a 2π-periodic: $\delta I_{SD}(\theta + 2\pi) = \delta I_{SD}(\theta)$ as it should be in the case of A.B. effect. From here we will omit the coefficient in front of the expression of $\delta I_{SD}(\theta)$. By expanding $\cos\big(\theta - \delta(\epsilon)\big)$ we get

$$\begin{array}{rl} \delta I_{SD}(\theta) \propto & \cos\theta \int t_{QD}(\epsilon) \cos(\delta(\epsilon)) \left[f_L(\epsilon) - f_R(\epsilon) \right] d\epsilon + \\ + & \sin\theta \int t_{QD}(\epsilon) \sin(\delta(\epsilon)) \left[f_L(\epsilon) - f_R(\epsilon) \right] d\epsilon \end{array} \tag{4.114}$$

In this expression the dependence on the magnetic field, θ, is independent of the integration over the energy. One can notice that the integrals in the Eq.4.114 are nothing else that the currents at a given value of the magnetic field

$$\delta I_{SD}(\theta) \propto \cos\theta \; \delta I_{SD}(0) + \sin\theta \; \delta I_{SD}(\pi/2) \tag{4.115}$$

This expression can be written in a simpler form which defines the effective phase shift of the quantum dot out of equilibrium, Δ

$$\delta I_{SD}(\theta) \propto \cos(\theta - \Delta) \tag{4.116}$$

where

$$\tan\big(\Delta\big) = \delta I_{SD}(\pi/2) / \delta I_{SD}(0) \tag{4.117}$$

Eq.4.117 defines the transmission phase shift in the case of non-equilibrium transport at finite temperature. Note that this expression gives the correct result in the limit of linear response and zero temperature $\Delta = \delta(\mu)$. In order to obtain Δ we need to calculate the retarded Green function, $G^r_{d\sigma}$, at the impurity site. Then the magnitude of the transmission amplitude, t_{QD}, can be easily calculated while the phase, $\phi = \arg(c\Gamma G^r_{d\sigma})$, depends on the unknown phase factor c. At equilibrium the additional phase introduced

by this factor is found using Levinson's theorem but out of equilibrium its validity can be questioned. In general, one needs some type of non-equilibrium generalization of Levinson's theorem to determine the value of the unknown phase factor c. The phase of the retarded Green function can be found using Kramers-Kronig relations.

We have directly calculated Δ in the high-temperature limit ($T \sim 0.5\Gamma$) at equilibrium and found quite reasonable agreement between πn_0 and Δ as a function of the localized level energy, ϵ_0. The difference is due to the temperature smearing (many modes participates in the charge transfer) as well as the inaccuracy of the NCA method. We expect the phase Δ to tends towards the occupation πn_0 as the temperature is lowered. We know that in this limit (linear response in V_{SD} and at low temperatures $T \to 0$) the phase shift Δ satisfies Levinson's theorem and $\Delta = \pi n_0$ (in this limit $\Delta \equiv \delta$). But at low temperatures the NCA method becomes less accurate. The method is known to overestimate the Kondo peak amplitude somewhat for chemical potentials within a few Γ of the bare-level energies. This directly affects the calculations of Δ. The method recovers the correct result far from the bare-level energy $|\mu - \epsilon_0| \gg \Gamma$ where $\delta(\mu)$ asymptotically tends towards the occupation number, πn_0. So we suppose that $c = 1$ in our numerical calculations. We will come back to the temperature dependence of the transmission phase shift, Δ, later, when we will present the results of the calculations.

Assuming that, $\arg c = 0$, Eq.4.114 in the case of a symmetrically coupled quantum dot, $\Gamma_L = \Gamma_R$, can be written as

$$\begin{aligned} \delta I_{SD}(\theta) \propto & \quad \cos\theta \int \Gamma \, \mathtt{Re}\, G^r_{d\sigma} \left[f_L(\epsilon) - f_R(\epsilon) \right] d\epsilon + \\ & + \quad \sin\theta \int \Gamma \, \mathtt{Im}\, G^r_{d\sigma} \left[f_L(\epsilon) - f_R(\epsilon) \right] d\epsilon \end{aligned} \tag{4.118}$$

We can express the phase Δ defined by Eq.4.117 in terms of the localized electron retarded Green function.

$$\tan\Delta = \frac{\int \, \mathtt{Im}\left\{ G^r_{d\sigma}(\epsilon) \right\} \left[f_L(\epsilon) - f_R(\epsilon) \right] d\epsilon}{\int \, \mathtt{Re}\left\{ G^r_{d\sigma}(\epsilon) \right\} \left[f_L(\epsilon) - f_R(\epsilon) \right] d\epsilon} \tag{4.119}$$

where $\mathtt{Im}\left\{ G^r_{d\sigma}(\epsilon) \right\} = -\pi \rho_\sigma(\epsilon)$ and the real part of the retarded Green function can be obtained using the Kramers-Kronig relations

$$\mathtt{Re}\left\{ G^r_{d\sigma}(\epsilon) \right\} = \mathtt{P.v.} \int \rho_\sigma(\epsilon') \frac{1}{\epsilon - \epsilon'} d\,\epsilon' \tag{4.120}$$

We have already mentioned that the phase shift Δ given by Eq.4.117 gives the correct equilibrium zero-temperature limit. Thus Eq.4.119 also shows this property and in addition the finite-T limit coincides with the previously used definition of the finite-T phase shift [38]

$$\tan\Delta = \frac{\int \, \mathtt{Im}\left\{ G^r_{d\sigma}(\epsilon) \right\} \frac{\partial f(\epsilon)}{\partial \epsilon} \, d\epsilon}{\int \, \mathtt{Re}\left\{ G^r_{d\sigma}(\epsilon) \right\} \frac{\partial f(\epsilon)}{\partial \epsilon} \, d\epsilon} \tag{4.121}$$

The complete expression for the oscillating part of the source-drain current is given by

$$\delta I_{AB} = \frac{4e}{h} t_{ref} |\mathbf{t}_{QD}| \cos(\theta - \Delta) \tag{4.122}$$

where Δ is given by Eq.4.119 and the "total" transmission amplitude $\mathbf{t}_{QD}$ is the thermal average of the transmission amplitude at the energy ϵ: $t_{QD}(\epsilon) = \Gamma G^r_{d\sigma}(\epsilon)$.

$$\mathbf{t}_{QD} = \Gamma \int_{-\infty}^{+\infty} G^r_{d\sigma}(\epsilon) \left[f_L(\epsilon) - f_R(\epsilon) \right] d\epsilon \tag{4.123}$$

4.7.2 Modelling

We model the quantum dot with its leads by an Anderson Hamiltonian with two reservoirs

$$\begin{array}{rcl} H & = & \sum_{\sigma;\, k \in L,R} \epsilon_{k\sigma} c^\dagger_{k\sigma} c_{k\sigma} + \epsilon_0 \sum_\sigma d^\dagger_\sigma d_\sigma + U n_\uparrow n_\downarrow \\ & + & \sum_{\sigma;\, k \in L,R} \left(V_{k\,\sigma} c^\dagger_{k\sigma} d_\sigma + H.c. \right) \end{array} \tag{4.124}$$

where $c^\dagger_{k\sigma}$ ($c_{k\sigma}$) creates (annihilates) an electron with momentum k and spin σ in one of the two leads, and $d^\dagger_\sigma$ (d_σ) creates (annihilates) a spin-σ electron in the quantum dot. The third term describes the Coulomb interactions among electrons on the dot. We assume that $U \to \infty$, forbidding double occupancy. The forth term describes the hopping between the leads and the dot, and fixes the coupling strength via $\Gamma^{L(R)}_\sigma(\omega) = 2\pi \sum_{k \in L(R)} |V_{k\,\sigma}|^2 \delta(\omega - \epsilon_{k\sigma})$. We restrict ourself to the case of a symmetric quantum dots where $\Gamma_L = \Gamma_R$.

Our aim is to calculate the occupation number n_0 of the quantum dot and the phase shift Δ out of equilibrium. We have used three standard methods in our study:

(a) In order to apply perturbation expansion in the hopping strength Γ in the limit $U \to \infty$ we use the slave-boson representation of the hamiltonian Eq.4.124.

(b) Since we address the non-equilibrium properties we use the Keldysh formalism which allows to go beyond the linear response theory.

(c) In order to obtain a well-behaved density of states in the non-equilibrium perturbation theory we use the noncrossing approximation, which has been successfully used to treat the infinite-U Anderson model at equilibrium.

The NCA equations for the components of the Keldysh Green functions were solved self-consistently. At the end, the properties of physical electrons are derived from the results for the auxiliary bosons and fermions (from the slave-boson representation).

4.7.3 Results

In this section, we present the numerical results for the occupation number and the transmission phase shift for the Anderson model in and out of equilibrium. The phase

shift Δ can be calculated within the required accuracy in the limits described in Fig.4.15. First we will discuss the linear response case (Fig.4.15(a)) where the bias voltages are small compared to the bare level width, $|\mu_L - \mu_R| \ll \Gamma$. In this limit, the phase shift Δ can be calculated in the high-temperature limit. Then we will discuss the asymptotic limits (Fig.4.15(b)-(c)) when the Fermi levels are far from the energy of the localized state. Afterwards, the behavior of the phase shift Δ in the intermediate region for the bias voltages, $eV_{SD} \equiv \mu_L - \mu_R \sim \Gamma$, Fig.4.15(d), will be presented. We will finish this section by considering the interesting limit of a large bias voltage, Fig.4.15(e).

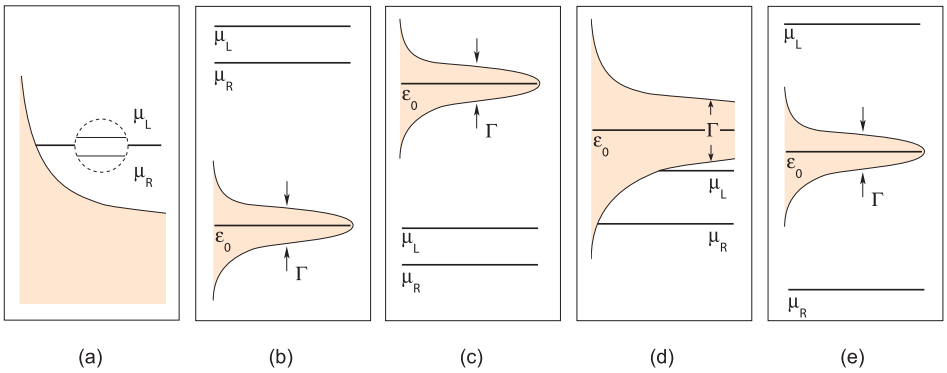

Figure 4.15: Limit cases: (a) equilibrium regime $\mu_L - \mu_R \ll \Gamma$ at relatively high temperatures; (b) and (c) asymptotic behavior: $\mu_L - \mu_R \sim \Gamma$ with $|\mu_{L,R}| \gg \Gamma$; (d) $\mu_L - \mu_R \sim \Gamma$ and $|\mu_{L,R}| \sim \Gamma$, (e) $\mu_L - \mu_R \gg \Gamma$

4.7.4 Results for the occupation number

The occupation number is calculated as a function of the localized level energy ϵ_0. The source-drain voltage V_{SD} and the temperature T are taken as parameters. In our calculations we count all the energies from the bare-level energy, ϵ_0, so that all the curves are plotted as a function of distance between ϵ_0 and the mean chemical potential, $\frac{1}{2}(\mu_L + \mu_R)$. All the energies are taken in units of the total coupling strength to the leads, Γ.

The occupation number, n_0, at different values of the bias voltages and at the lowest temperature $T = 0.005\Gamma$ is presented in Fig.4.16. In the limits $|\epsilon_0| \gg \mu_L$, μ_R the occupation number asymptotically tends towards the equilibrium curve at all values of V_{SD}. In the limit of large bias voltages $V_{SD}/e > 2\Gamma$, the occupation number exhibits a plateau-type structure at the vicinity of $\epsilon_0 - (\mu_L + \mu_R)/2 = 0$. For smaller bias voltages, $V_{SD}/e < 2\Gamma$, the deviation from the equilibrium curve consists in larger values of the occupation number in the regime between $\epsilon_0 - \mu_L \gg \Gamma$ and $\mu_R - \epsilon_0 \gg \Gamma$.

The occupation number at $\mu_L - \mu_R = 1.0\Gamma$ and $\mu_L - \mu_R = 5.0\Gamma$ at different temperatures are reported in the Fig.4.7.4 and Fig.4.18 respectively. The total occupation number is not sensitive to the behavior near the Fermi surface, and therefore the curves do not show significant temperature dependence up to $T \sim 1\Gamma$. In the case of large bias voltage, $eV_{SD} = 5.0\Gamma$, the occupation number, n_0, exhibits a plateau at the level

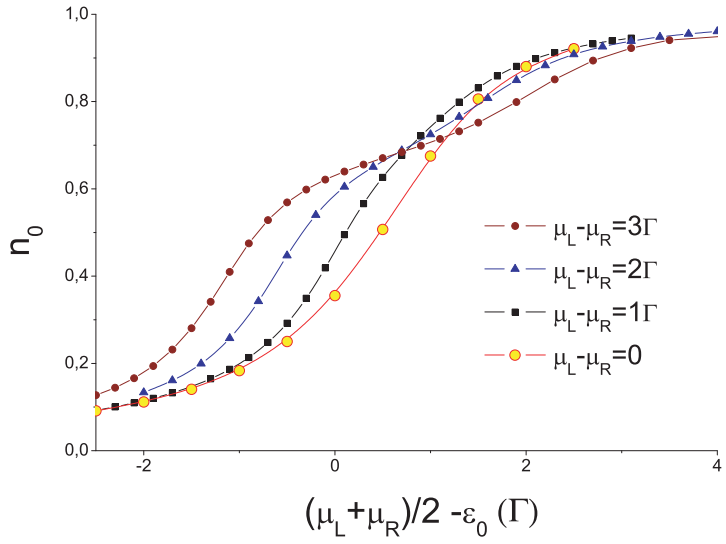

Figure 4.16: The occupation number as a function of the mean chemical potential in the leads $(\mu_L + \mu_R)/2$ measured from the position ϵ_0 of the localized level (in units of Γ) at $T = 0.005\Gamma$ and different voltage $eV_{SD} = \mu_L - \mu_R$ (including the equilibrium situation $\mu_L = \mu_R$).

$0.6 < n_0 < 0.7$. At high temperatures ($T \sim 0.5\Gamma$) the plateau is smeared and finally disappears as temperature is increased (at $T \sim 1.0\Gamma$).

4.7.5 Results for the transmission phase shift

The transmission phase shift, Δ, is calculated as a function of the localized level energy ϵ_0. The source-drain voltage V_{SD} and the temperature T are taken as parameters.

4.7.5.a Effect of the temperature at equilibrium

In the expression for the transmission phase shift Δ, Eq.4.119, the retarded Green function can be expanded into Taylor's series around $\epsilon = \mu$. For relatively low temperatures we can stop at the second order term

$$G^r_{d\sigma}(\epsilon) = G^r_{d\sigma}(\mu) + \frac{d}{d\epsilon} G^r_{d\sigma}(\epsilon)\Big|_\mu \cdot (\epsilon - \mu) + \frac{1}{2}\frac{d^2}{d\epsilon^2} G^r_{d\sigma}(\epsilon)\Big|_\mu \cdot (\epsilon - \mu)^2 + ... \qquad (4.125)$$

The difference between the Fermi distribution functions of the electrons in the different leads can be also replaced by derivative following Eq.4.103 since the bias voltage is a small quantity. One can note, that all the odd powers of $(\epsilon - \mu)$ are antisymmetric functions while the integration with symmetric one, $\partial f(\epsilon)/\partial\epsilon$, over infinite interval will give zero. We can write

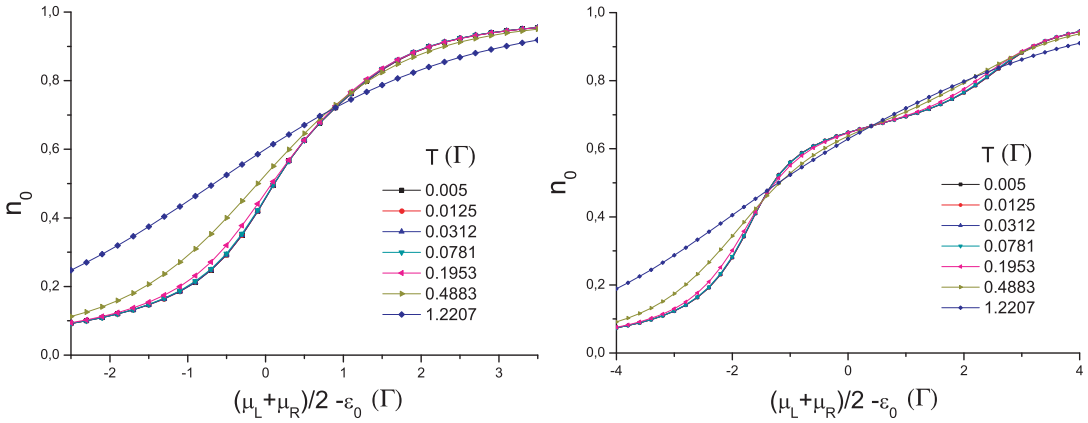

Figure 4.17: (Left) the occupation number as a function of the mean chemical potential in the leads $(\mu_L + \mu_R)/2$ measured from the position ϵ_0 of the localized level (in units of Γ) for $eV_{SD} = \Gamma$ at different temperatures. Note that the temperature affects the result in a significant way when $T > 0.5\Gamma$.

Figure 4.18: (Right) the occupation number as a function of the mean chemical potential in the leads $(\mu_L + \mu_R)/2$ measured from the position ϵ_0 of the localized level (in units of Γ) for $eV_{SD} = 5\Gamma$ at different temperatures. Note the onset of a plateau around $(\mu_L + \mu_R)/2 - \epsilon_0 = 0$. As before, the temperature affects the result in a significant way when $T > 0.5\Gamma$. The plateau disappears when $T > \Gamma$.

$$\tan\Delta = \frac{\int_{-\infty}^{+\infty}(\partial f(\epsilon)/\partial\epsilon)\left[\mathtt{Im}\,G^r_{d\sigma}(\mu) + \frac{1}{2}\frac{d^2}{d\epsilon^2}\,\mathtt{Im}\,G^r_{d\sigma}(\epsilon)\Big|_\mu \cdot (\epsilon-\mu)^2\right]d\epsilon}{\int_{-\infty}^{+\infty}(\partial f(\epsilon)/\partial\epsilon)\left[\mathtt{Re}\,G^r_{d\sigma}(\mu) + \frac{1}{2}\frac{d^2}{d\epsilon^2}\,\mathtt{Re}\,G^r_{d\sigma}(\epsilon)\Big|_\mu \cdot (\epsilon-\mu)^2\right]d\epsilon} \tag{4.126}$$

using

$$\int_{-\infty}^{+\infty}\frac{\partial f(\epsilon)}{\partial\epsilon}\,d\epsilon = 1 \tag{4.127}$$

Eq.4.126 can be rewritten as

$$\tan\Delta = \frac{\mathtt{Im}\,G^r_{d\sigma}(\mu) + \frac{1}{2}\frac{d^2}{d\epsilon^2}\,\mathtt{Im}\,G^r_{d\sigma}(\epsilon)\Big|_\mu \int_{-\infty}^{+\infty}(\epsilon-\mu)^2\,(\partial f(\epsilon)/\partial\epsilon)\,d\epsilon}{\mathtt{Re}\,G^r_{d\sigma}(\mu) + \frac{1}{2}\frac{d^2}{d\epsilon^2}\,\mathtt{Re}\,G^r_{d\sigma}(\epsilon)\Big|_\mu \int_{-\infty}^{+\infty}(\epsilon-\mu)^2\,(\partial f(\epsilon)/\partial\epsilon)\,d\epsilon} \tag{4.128}$$

The integral in the nominator and denominator does not depends on the retarded Green function and can be considered as a temperature dependent factor

$$\varepsilon_T \equiv \int_{-\infty}^{+\infty}\frac{\partial f(\epsilon)}{\partial\epsilon}\,(\epsilon-\mu)^2\,d\epsilon \propto T^2 \tag{4.129}$$

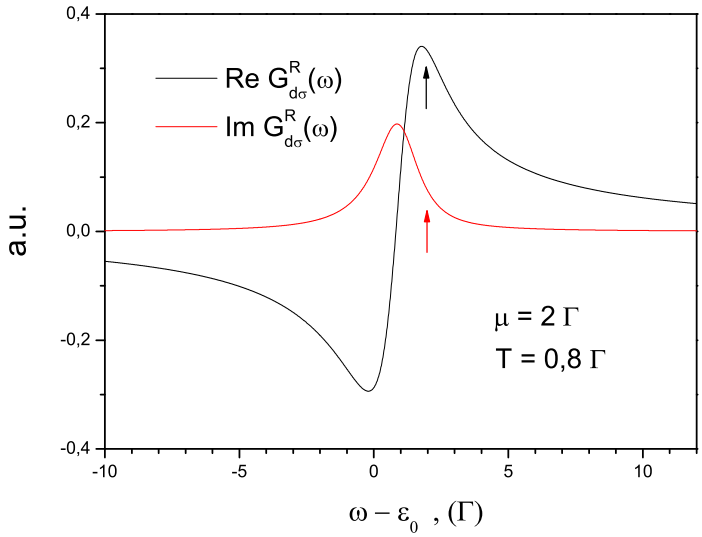

Figure 4.19: Real and imaginary parts of the retarded Green function as a function of $\omega - \epsilon_0$ for $\mu = 2\Gamma$ and $T = 0.8\Gamma$. The point $\omega - \epsilon_0 = \mu$ is indicated by an arrow.

so that in the $T \to 0$ limit additional contribution vanishes and the phase Δ reaches the correct equilibrium zero-temperature value. Within this notation Eq.4.119 takes the form

$$\tan \Delta = \frac{\mathtt{Im}\, G^r_{d\sigma}(\mu) + [\mathtt{Im}\, G^r_{d\sigma}(\epsilon)]''_\mu\, \varepsilon_T}{\mathtt{Re}\, G^r_{d\sigma}(\mu) + [\mathtt{Re}\, G^r_{d\sigma}(\epsilon)]''_\mu\, \varepsilon_T} \tag{4.130}$$

where $[\phi(x)]''_{x_0}$ denotes the second derivative of the function $\phi(x)$ calculated at $x = x_0$. Following Eq.4.130, the behavior of the phase shift Δ depends on the values and, more importantly, on the sign of the second derivative of the real and imaginary parts of the retarded Green function. The characteristic high-temperature behavior of the real and imaginary parts of retarded Green function, $T \sim 0.8\Gamma$, is given on the Fig.4.19.

Note that the energy dependence of the real part of the retarded Green function shows a special point, $\omega = \tilde{\epsilon_0}$, where $\mathtt{Re}\, G^r_{d\sigma}(\omega)$ and its second derivative are equal to zero. This point approximately corresponds to the renormalized bare level energy which is defined as the position of the maximum of the electron density of states. The imaginary part of the retarded Green function, $\mathtt{Im}\, G^r_{d\sigma}(\omega)$, at this point has a finite value as well as the thermally weighted integral in its vicinity. The phase shift Δ at this point does not see thermal smearing and, following Eq.4.119, equals $\pi/2$ (See Fig.4.20).

The second derivative of the electron density of states or, equivalently, of the imaginary part of the retarded Green function has a constant sign in the vicinity of the point $\omega = \tilde{\epsilon_0}$. On the contrary, the $\left[\mathtt{Re}\, G^r_{d\sigma}(\mu)\right]''$ changes sign. From this simple analysis we can conclude, that the behavior of the phase Δ is "asymmetric" around this point

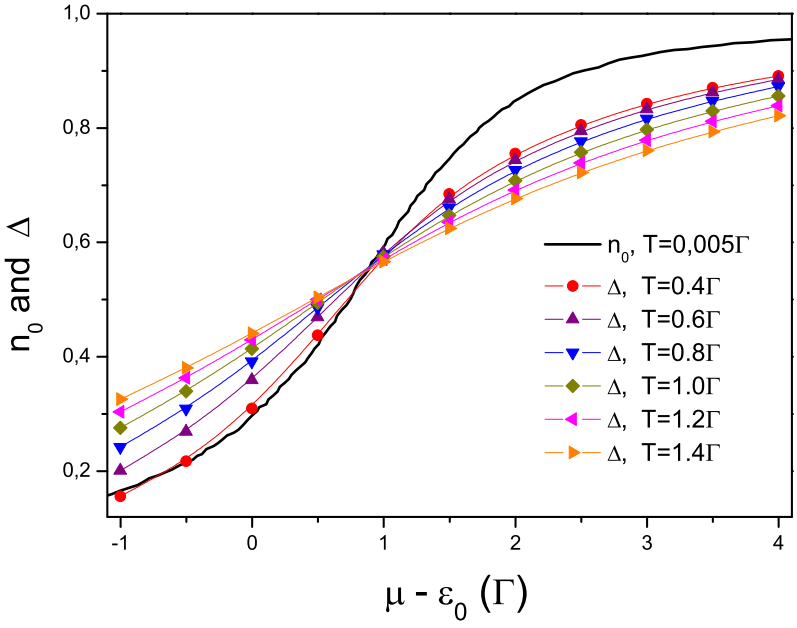

Figure 4.20: Phase shift Δ as a function of $\mu - \epsilon_0$ at different temperatures for $eV_{SD} = 10^{-5}\Gamma$ (equilibrium regime). For comparison πn_0 as a function of $\mu - \epsilon_0$ at $T = 0$ is also reported – black line (result obtained in Ref.[65]). Let us remaind that πn_0 coincide with Δ at $T = 0$.

by comparison with the equilibrium zero-temperature phase shift. The real situation is more complicated, however, since the Green function itself is a finite temperature Green function, its values can significantly deviate from the zero-temperature result. The curves drawn from numerical calculations are reported in Fig.4.20.

At high temperatures, when the Kondo peak in the local density of states, $\rho_\sigma(\omega)$, is suppressed, the transmission phase shift can be calculated in different regimes. The high temperature limit corresponds to $T \geq 0.4\Gamma$. At lower temperatures, $\rho_\sigma(\omega)$ exhibits the Kondo peak and our method becomes less accurate. Thus at equilibrium we are restricted to relatively high temperatures. Nevertheless, the zero-temperature limit is accessible through the occupation number, n_0. This quantity can be calculated in the NCA approach with high accuracy (up to within $0,5\%$ compared to the exact Bethe-Ansatz results).

4.7.5.b Asymptotic behavior

In this limit the phase of the retarded the Green function as well as Green function itself is nearly constant in the range of energies where transport takes place. In Eq.4.114 giving the expression of δI_{SD} as a function of θ, one can approximate the $\cos(\delta(\epsilon))$ and $\sin(\delta(\epsilon))$ factors by

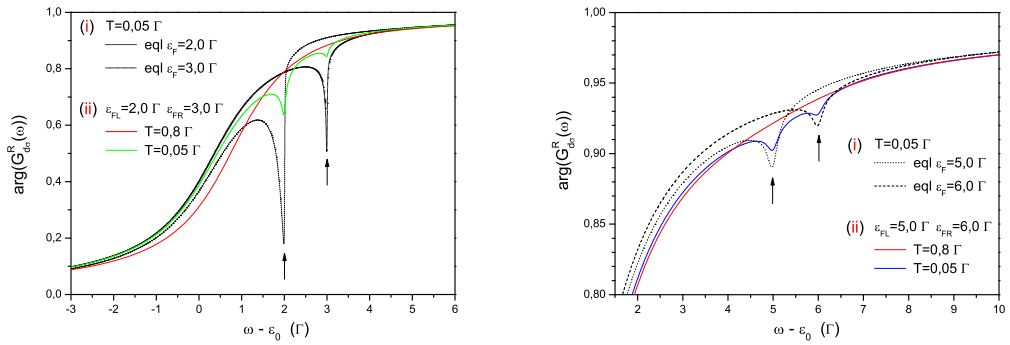

Figure 4.21: The phase $\arg G^r_{d\sigma}(\omega)$ of the retarded localized electron Green function as a function of $(\omega - \epsilon_0)$ both (i) at equilibrium at $\mu = \mu_1$ and $\mu = \mu_2$ for $T = 0.05\Gamma$, and (ii) out-of-equilibrium at $T = 0.8\Gamma$ and $T = 0.05\Gamma$ for $\mu_L = \mu_1$ and $\mu_R = \mu_2$. (Left) result for the values $\mu_1 = 2\Gamma$ and $\mu_2 = 3\Gamma$. (Right) results for the values $\mu_1 = 5\Gamma$ and $\mu_2 = 6\Gamma$. The position of $(\mu_1 - \epsilon_0)$ and $(\mu_2 - \epsilon_0)$ respectively is indicated by an arrow. Note that $\arg G^r_{d\sigma}(\omega)$ depends strongly with ω when $(\mu_1 - \epsilon_0)$, $(\mu_2 - \epsilon_0)$ is small (left) whereas its energy dependence is negligible when $(\mu_1 - \epsilon_0)$, $(\mu_2 - \epsilon_0)$ is large (right).

$$\cos(\delta(\epsilon)) = \cos(\bar{\delta} + \partial\delta(\epsilon)) \approx \cos\bar{\delta} + O(\partial\delta) \tag{4.131}$$

with analogous expansion for the sin-factor

$$\sin(\delta(\epsilon)) = \sin(\bar{\delta} + \partial\delta(\epsilon)) \approx \sin\bar{\delta} + O(\partial\delta) \tag{4.132}$$

where $\bar{\delta}$ is chosen the high-temperature phase (See Fig.4.21, red curves) and $\partial\delta$ is the maximum deviation $\max|\delta(\epsilon) - \bar{\delta}|$. The phase shift Δ then can be estimated to

$$\tan\Delta = \frac{(\sin\bar{\delta} + O(\partial\delta)) \int t_{QD}(\epsilon)\,[f_L(\epsilon) - f_R(\epsilon)]\,d\epsilon}{(\cos\bar{\delta} + O(\partial\delta)) \int t_{QD}(\epsilon)\,[f_L(\epsilon) - f_R(\epsilon)]\,d\epsilon} \tag{4.133}$$

Using the condition that $|\cos\bar{\delta}| \gg \partial\delta$ which is justified in the limit $|\epsilon - \tilde{\epsilon}_0| \gg \Gamma$ we can write

$$\tan\Delta = \tan\bar{\delta} + O(\partial\delta) \tag{4.134}$$

Even if we discuss the finite-T out-of-equilibrium case, the transport can be described in terms of linear response theory. The phase, thus, can be replaced by $\delta = \pi n_0$ as in the equilibrium situation. At the finite temperatures the phase is averaged in the sense of Eq.4.119 where, as we have already noticed, the retarded Green function is nearly constant. Thus the thermal averaging do not change the phase shift, $\Delta \approx \delta$. As for n_0, we know from the results for the occupation number discussed previously, that the non-equilibrium occupation number asymptotically tends towards the equilibrium occupation far from $\tilde{\epsilon_0}$, see Fig.4.16. The deviation from the true value can be estimated to within a few percents and becomes smaller as $|\mu - \epsilon_0|$ increases (see Fig.4.21).

On the contrary, when the left and right chemical potentials are close to the (renormalized) energy of the localized level, $\tilde{\epsilon}_0$, this type of approximation in no longer valid and the values of the phase shift Δ should be calculated numerically using Eq.4.119 (regime (d) of Fig.4.15).

To summarize, let us note that far away from the renormalized energy of the localized state, $\tilde{\epsilon}_0$, the phase shift Δ asymptotically tends towards the equilibrium transmission phase shift, δ, both at finite bias voltages and temperatures.

4.7.5.c Intermediate regime

The behavior of the phase Δ at finite bias voltages, far from the linear response regime (when $|\mu_L - \mu_R| \ll \Gamma$), is discussed in this subsection. The phase Δ as a function of the distance between the bare-level energy and the mean chemical potential, $\epsilon_0 - \frac{1}{2}(\mu_L + \mu_R)$, is calculated at three values of the bias voltage eV_{SD}: $1.0\,\Gamma$ (Fig.4.22); $2.0\,\Gamma$ (Fig.4.23) and $4.0\,\Gamma$ (Fig.4.24). In each case the phase Δ is calculated at different temperatures, generally in the range from low-temperature, $0.05\,\Gamma$, to the high temperature limit, $1.0\,\Gamma$. In any case Δ is almost temperature independent in the low temperature limit. Significant deviations from the low-temperature behavior are observed only at high temperatures, $T \sim 1\,\Gamma$, (see Figs.4.22-4.24).

The low-temperature behavior of the phase Δ as a function of ϵ_0 at different values of the bias voltage is shown in Fig.4.25. At low bias voltages Δ behaves as n_0. Like the occupation number, the phase Δ slightly "shifts" towards negative chemical potentials (where ϵ_0 lies the above mean chemical potential) when the bias voltage is increased. Starting approximately from $eV_{SD} = 4.0\,\Gamma$ the phase shift Δ exhibits a shoulder structure approximately around $\epsilon_0 - \frac{1}{2}(\mu_L - \mu_R) = 0$. At high temperatures this feature disappears.

Note that at a given bias voltage the curves obtained at various temperatures intersect in the vicinity of the point where $\Delta = \pi/2$. At equilibrium, see Fig.4.20, this property results from a symmetry property of the (real and imaginary parts of the) retarded Green function.

4.7.5.d Large bias voltage regime

As we have seen, when the bias voltage becomes large, the phase shift Δ exhibits a shoulder structure in the vicinity of the point $\epsilon_0 = \frac{1}{2}(\mu_L + \mu_R)$. Here we show the behavior of Δ in the limit $eV_{SD} \gg \Gamma$. In Fig.4.26 the phase Δ is plotted as a function of $\epsilon_0 - \frac{1}{2}(\mu_L - \mu_R)$ at the bias voltages $10.0\,\Gamma$ and $15.0\,\Gamma$ in the low-temperature limit ($T = 0.05\,\Gamma$). The shoulder structure in these cases is more pronounced compared to the previous case represented in Fig.4.24. If $\mu_L \ll \tilde{\epsilon}_0 \ll -\mu_R$ the numerator of the right-hand side of Eq.4.119 is almost independent of ϵ_0 while its denominator is ϵ_0-dependent. The interplay of these two effects gives rise to the formation of a shoulder in the behavior of the phase Δ. The phase shift asymptotically tends towards the equilibrium phase shift.

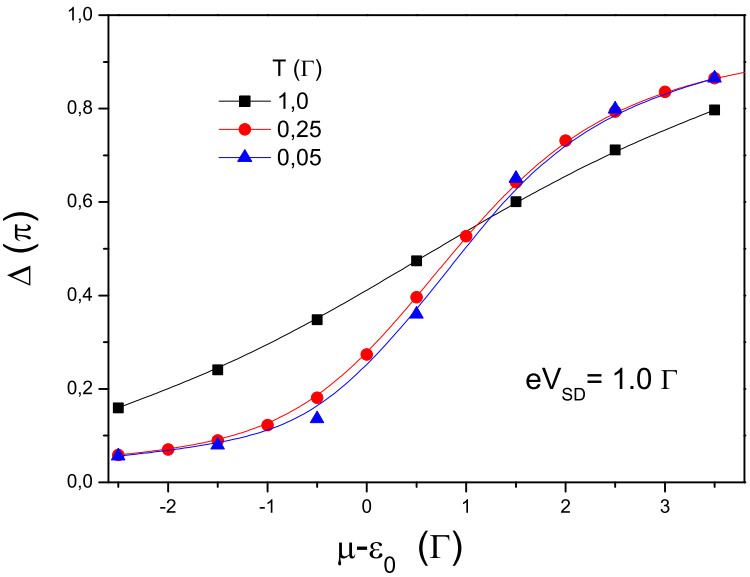

Figure 4.22: Phase shift Δ as a function of $\mu - \epsilon_0$ at different temperatures for $eV_{SD} = \Gamma$ (out of equilibrium).

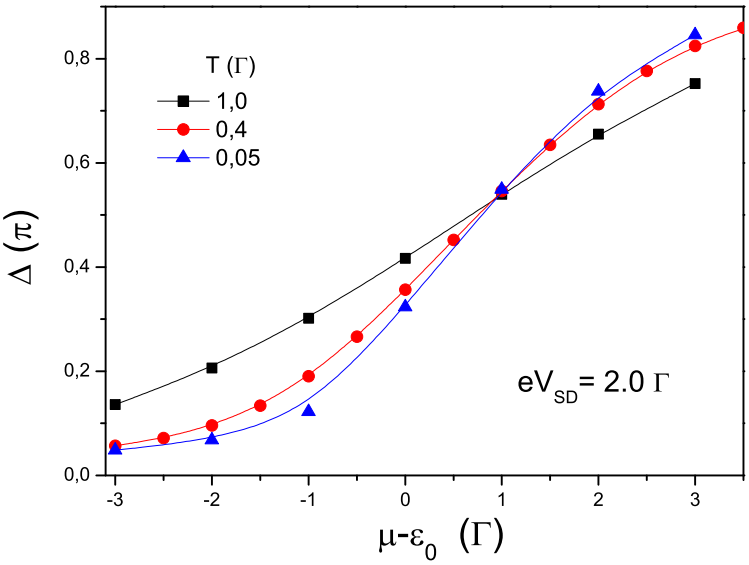

Figure 4.23: Phase shift Δ as a function of $\mu - \epsilon_0$ at different temperatures for $eV_{SD} = 2\Gamma$ (out of equilibrium).

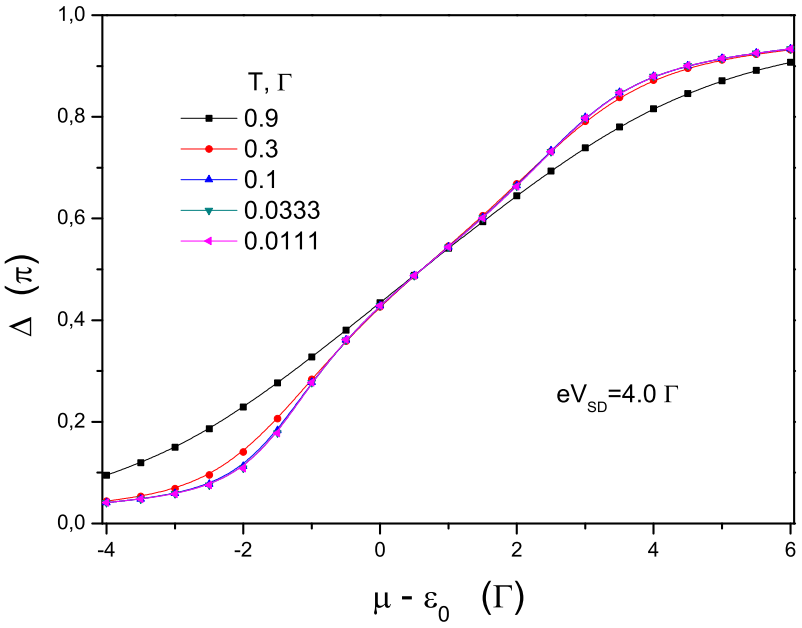

Figure 4.24: Phase shift Δ as a function of $\mu - \epsilon_0$ at different temperatures for $eV_{SD} = 4\Gamma$ (out of equilibrium). Note the presence of a shoulder structure in the evolution which disappears when $T > 0.9\Gamma$.

4.7.6 Comparison with experiments

Since a quantum dot weakly coupled to the leads can be described by an Anderson model, we can discuss the behavior of the experimental system in the light of the results obtained in the previous section. Unfortunately, since the calculations are performed for the infinite-U model we can not present any fit of the experimental data because the experimental setup corresponds to a large but finite Coulomb interaction energy U. Nevertheless we can examine the qualitative behavior of the phase shift Δ with the temperature and bias voltage. Theoretical curves are drawn at different values of both temperature T and chemical potentials difference $\mu_L - \mu_R$. As we have already mentioned, neither the occupation number nor the phase shift Δ depend on temperature at $T < 0.4\,\Gamma$. In this regime then we are left with a single parameter $\mu_L - \mu_R$.

The evolution of the transmission phase shift that we obtained from NCA calculations above reproduce the evolution observed experimentally: at low bias voltages the phase shift is larger than at equilibrium. To illustrate this effect the phase should be plotted as a function of the difference between the bare-level energy, ϵ_0, and the mean chemical potential, $(\mu_L + \mu_R)/2$. At high bias voltages, $eV_{SD} \geq 4.0\,\Gamma$, the phase shift exhibits a shoulder structure which is more pronounced at high voltages. Let us note that $V_{SD} = -100\,\mu V$ already corresponds to the "high bias" regime since the measured

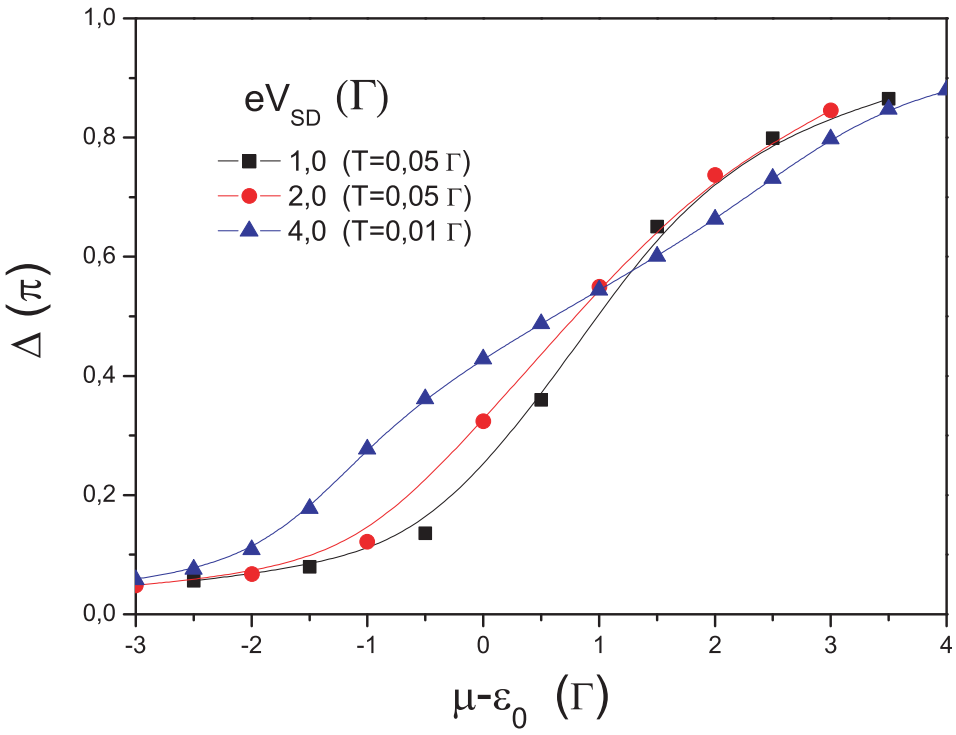

Figure 4.25: Phase shift Δ as a function of $\mu - \epsilon_0$ at different values of the bias voltage eV_{SD} (the temperature considered in each case varies but is always low). Note that the evolution exhibits a shoulder-structure when V_{SD} becomes large.

phase shift develops a shoulder-like structure [35].

The high temperature and bias voltage regimes in the real A.B. rings result in a strong dephasing processes. The coherent contribution to the current is thus reduced by processes which are not accounted for in our analysis.

4.7.7 Conclusions

4.7.7.a What is good?

We have analyzed the effects of finite bias voltage and finite temperature on a behavior of the transmission phase shift of a conduction electron scattered off the quantum dot embedded in one of the arms of the A.B. ring. Our analysis goes beyond the linear-response theory that enables us to investigate the behavior of the phase shift and the occupation number at high bias voltages and temperatures. We have proposed to define the transmission phase shift as the shift of the periodic Aharonov-Bohm ring current oscillations as the gate voltage V_G is changed, in analogy with the equilibrium phase shift. The phase shift defined in such a way corresponds to the experimentally measured quantity. We have derived the expression for the phase shift in terms of the retarded Green function of the impurity site (quantum dot in our case) for arbitrary temperatures and bias voltages. We have shown that the expression for the phase shift gives correct result in the limit of zero temperature at equilibrium and reproduces the expression

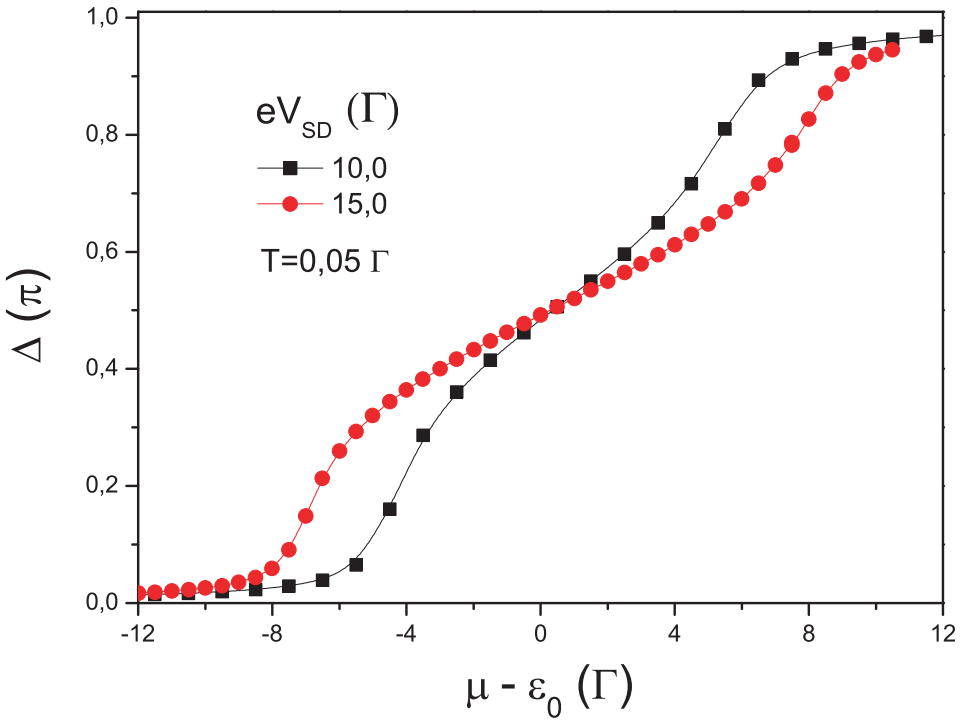

Figure 4.26: Phase sift Δ as a function of $\mu - \epsilon_0$ at different values of the bias voltage $\mu_L - \mu_R$ for $T = 0.05\Gamma$ (low temperature regime).

previously established in the linear-response regime.

In order to apply the theory to the case of quantum dots, we have solved the system of equations numerically in order to derive the retarded non-equilibrium temperature dependent Green function. The values of the retarded Green function have then been used to obtain the transmission phase shift. We have analyzed the behavior of the occupation number and transmission phase shift out of equilibrium and at finite temperatures.

4.7.7.b What is bad?

We have studied only the symmetric quantum dot with $\Gamma_L = \Gamma_R$. It would be interesting to also study asymmetric quantum dots. This asymmetry is known to lead to a reduction of the conductance by a factor $4\Gamma_L\Gamma_R/(\Gamma_L+\Gamma_R)^2$. As far as the phase shift is concerned, the effect could be completely different.

Our study can not be extended to the equilibrium situation at low T. To be able to distinguish the transition from the high temperature limit to the low-temperature (Fermi liquid) regime at the equilibrium one needs to apply more sophisticated methods able to describe with higher accuracy the behavior near the Fermi surface at low temperatures. One should also think whether or not Levinson's theorem can be extended to the out-of-equilibrium situation.

General conclusion

The first part of the thesis is devoted to the study of the effects of Kondo correlations on the transmission phase shift of a quantum dot (QD) coupled to two leads. Experimental determination of the phase shift made by embedding a quantum dot in one of the arms of a (an open) Aharonov-Bohm interferometer leads to a value of the phase which differs from the well-known theoretical predictions obtained both analytically and by numerical calculations. The present work is motivated by this discrepancy. We have proposed a theoretical interpretation of these results based on scattering theory combined with Bethe ansatz calculations in the framework of the single-impurity Anderson model. We have proved the existence of a factor of 2 of difference between the total phase of the S-matrix (responsible for the shift in the A-B oscillations), and the one appearing in the expression of the conductance $G \sim \sin^2(\delta/2)$ implying a partial phase shift-per spin-. The transmission phase shift, following the Friedel sum rule, is equal to the occupation of the impurity site in units of π. We have solved the equations of the Bethe ansatz numerically at $T = 0$. This allows us to determine the value of n_0 as a function of the parameters of the Anderson model. As it follows from general properties of the model, the occupation has a single fitting parameter. We have established a scheme to find out the appropriate value of the fitting parameter assuming a linear dependence of the applied gate voltage with the energy of localized level. Taking the particle-hole symmetry into account we have been able to fit the experimental results on the range of V_G corresponding to two successive resonances in different regimes. Quantitative agreement is obtained with experimental results both in the unitary limit and the weak Kondo coupling regimes. In the low-temperature limit, $T \ll T_K$, this prediction is in excellent agreement with experimental data. This result so far has been restricted to the unitary limit case. When the Kondo correlations are suppressed by temperature or external field, the system is far from the unitary limit and the experimental results strongly deviate from the predicted behavior.

The expression for the transmission amplitude of the quantum dot in the Kondo regime obtained in the first part of this work correctly describes the conductance of the quantum dot, the behavior of the transmission phase shift as a function of the energy of the localized level ϵ_0, and explains the unexpected abrupt change of the transmission phase shift - the phase lapses. The latter question is discussed in the second part of this work. For the quantum dot in the Kondo regime, the phase lapses are found to be incomplete. This result is in agreement with the experimental observations. Using the same arguments as for the case of the quantum dot in the Kondo regime, we show the presence of a complete phase lapse in the Coulomb blockade regime. The phase lapses result from the change of sign of the transmission amplitude of the quantum dot. The phase lapses in both regimes, the Kondo and the Coulomb blockade regimes, is not associated with any related energy scale. The dependence of the ring conductance with the transparency of the reference arm of an Aharonov-Bohm interferometer is also discussed.

In the third part, we have studied the transmission phase shift at finite bias voltages

and temperatures. This part is motivated by experimental measurements performed at finite temperatures and finite bias voltages. In order to apply perturbation expansion in the coupling strength Γ in the $U \to \infty$ limit we have used the slave-boson representation. Since we address the non-equilibrium properties we have used the Keldysh formalism. To obtain a well-behaved density of states from the non-equilibrium perturbation theory we have employed the noncrossing approximation, which has been successfully used by other authors to treat the infinite-U Anderson model in equilibrium. In order to apply the theory to the case of interest, the quantum dots, we have numerically solved the system of equations which define the non-equilibrium retarded temperature dependent Green function. The values of the retarded Green function have then been used to derive the transmission phase shift which we proposed to define as the deviation of the periodic Aharonov-Bohm ring current oscillations when the gate voltage varies, making an analogy with the equilibrium phase shift. The phase shift thus defined corresponds to the experimentally measured quantity. We have then analyzed the behavior of the occupation number and transmission phase sift out of equilibrium and at finite temperatures. Qualitative agreement has been obtained with experimental data.

List of Figures

1.1 Temperature dependence of the resistivity of pure metal (Cu) and dilute magnetic alloy [1]. 12

1.2 Temperature dependence of the resistivity for different concentrations of impurity atoms - comparison between experiment (circles) and theory (curves) [4]. 13

1.3 Formation of the spin singlet complex at low temperatures. Magnetic impurity virtually traps one conduction electron in order to compensate its magnetic moment. 16

1.4 Left: Scanning electron microscope image of a typical quantum dot (top view). The black regions indicate the 2DEG, gray regions indicate the metal gates [29]. Right: Schematic representation of quantum a dot structure. 20

1.5 (A) Conductance through the quantum dot as a function of gate voltage V_G, [30]. The quantum dot is either in a "locked" (B) or an "open" (C) regime. 21

1.6 Conductance as a function of V_G for different temperatures. T ranges from 15 mK (black trace) up to 800 mK (red trace) [32]. 22

1.7 Conductance as a function of temperature for different values of gate voltage V_G. Plotted as functions of T/T_K all the curves show a universal behavior [32]. 23

1.8 Electron micrograph of the Aharonov-Bohm interferometer used in the [21]. The black regions indicate the 2DEG, gray regions indicate the metal gates. Electrons flow between source and drain through the left or the right arm of the Aharonov–Bohm ring. The quantum dot is inserted in the left arm. The central metallic island is biased via an air bridge (B) [21]. 24

1.9 The ring current as a function of the plunger gate voltage. The large current of the reference (right) arm has been subtracted. The top left part shows the Aharonov–Bohm oscillations of the current as a function of magnetic field at fixed $V_P = V_m$. In the inset: oscillation contrast defined as the amplitude of the ring current oscillations vs. the average current through the dot [21]. 25

1.10 (a) A series of three Coulomb peaks and (b) the current oscillations measured at the marked points A, B, and C. All oscillations are seen to be in phase. The large current of the reference (right) arm has been subtracted [21]. 26

1.11 Evolution of the Aharonov–Bohm phase through a current peak. (a) Current as a function of gate voltage (or plunger voltage $V_P \equiv V_G$) at a current peak. (b) A series of interference patterns taken at the points specified in (a). Note the phase jump between patterns 2 and 3. (c) Phase measured at two peaks (circles and triangles). The broken line is guide to the eye. The expected behavior of the quantum dot transmission phase in a 1D resonant tunneling model is shown by the solid line [21]. . 27

1.12 A top-view scanning electron micrograph of the double–slit device used in the Schuster–experiment [22]. The grey areas are metallic gates on the top of the heterostructure. The quantum dot is inserted in the right slit [22]. 29

1.13 Schematic description of the device structure of the double-slit-like experiment. An Aharonov–Bohm ring is coupled to an emitter (E), a collector (C) and a base region (B). Reflector gates reflect diverging electrons towards the collector. The quantum dot is designed by the central electrode and the three electrodes on the right hand side of the structure [22]. . . . 29

1.14 Conductance and phase evolution along a Coulomb peak. (a) Resonance peaks as a function of the plunger gate voltage. (b) A series of interference patterns taken at the points specified in (a). (c) Squared magnitude and phase of the Aharonov–Bohm oscillations (dots). The solid and dashed line are fits for the phase and the squared magnitude obtained with a Breit–Wigner model [22]. 31

1.15 (a) A series of Coulomb peaks; (b) Magnitude of the Aharonov–Bohm oscillations; (c) Phase of the Aharonov–Bohm oscillations as a function of plunger gate voltage. The solid lines are guides to the eye [22]. 32

1.16 A top-view scanning electron micrograph of the double–slit device used in the Yang–experiment [35]. The black zones represent 2DEG and the grey areas are metallic gates on the top of the heterostructure. The quantum dot is inserted in the left slit. The barrier gate is added in order to shut off the reference arm and test the bare quantum dot [35]. 33

1.17 The complex transmission amplitude (phase and amplitude) of the quantum dot as a function of energy (plunger gate voltage) for different coupling strengths of the quantum dot to the leads. The coupling gets weaker from (a), the unitary limit, to (d), Coulomb blockade regime [35]. 34

2.1 A schematic representation of the one-dimentional Anderson model (left). The $i = 0$ site represents the localized state of energy ε_0. The model can be sketched in another way (right) which indicates the inner structure of the impurity. 40

2.2 Scattering of plane waves. A right-moving arrow corresponds to the plane wave e^{ikx}, a left-moving arrow corresponds to the plane wave e^{-ikx}. . . . 41

2.3 Dependence of the charge density (vertical axis) as a function of distance (schematically). Dashed line corresponds to the unperturbed charge density. 45

2.4 Bound and free wave functions for the $1s$ and $2s$ states. 47

2.5 The conductance through the scattering region is proportional to the probability for the electron to be transmitted. 48

2.6 Schematic representation of an Aharonov-Bohm interferometer. Electrons injected at the source (S) are collected at the drain (D). The ring of the interferometer consists of two arms: the reference arm and the one in which the quantum dot is imbedded. The closed interferometer (left) is not equivalent to the double slit experiment since it includes multiple traversals of the ring and therefore does not provide access to δ_{QD}. To overcome this difficulty base regions (B) are introduced (right) which collect the back-scattered electrons to ensure that only two forward-propagating paths reach the drain. 49

2.7 Experimental conductance $G_{exp}(V_G)$ (red squares) and phase shift $\Phi(V_G)$ (blue triangles) as a function of the gate voltage V_G (values taken from Ref.[35] incorporating a shift in the V_G-scale for $G_{exp}(V_G)$ evaluated to $\Delta V_G = 15mV$, and a shift in the δ-scale equal to $\Delta\delta = 0.29\pi$). The comparison of the curve $G(V_G) = \sin^2(\Phi(V_G)/2)$ (black squares) with $G_{exp}(V_G)$ (red squares) provides a check to the prediction made in Eq. 2.37. 51

2.8 V_G-dependence of both the conductance, G, of the quantum dot measured in an "one-arm" experiment and the visibility measured in a "two-arm" experiment [35]. The comparison of these 2 curves let a shift appear δV_G of the order of 15 mV. 52

2.9 Different regimes of the Anderson model in the "weak" coupling regime $\Gamma \ll U$. The dashed line corresponds to the occupation number (schematic). The symmetric limit correspond to values of ε_0 such that $(U + 2\varepsilon_0) \ll \sqrt{U\Gamma}$. Detailed calculations show that in this limit $n_0 = 1$ and the deviation at $\varepsilon_0 + U/2 \sim \sqrt{U\Gamma}$ is estimated to $1 - n_0 \sim (\Gamma/U)^{3/2}$. The asymmetric limit corresponds to $(U + 2\varepsilon_0) \gg \sqrt{U\Gamma}$. In the weak coupling regime, $\Gamma \ll U$, and in the intermediate valence regime $|\varepsilon_0| \ll U$ (represented by two white vertical lines), n_0 exhibits a universal behavior as a function of ε_0^* (Eq.2.42). At $\varepsilon_0^* = 0$ the occupation number takes the universal value $n_0 = 2 - \sqrt{2}$. The empty orbital regime is obtained when $n_0 \to 0$. 54

2.10 (a) Occupation number n_0 as a function of the normalized energy $(-\varepsilon_0/U+1/2)$ of the localized state for the Anderson model at different values of Γ/U where $\Gamma = \pi V^2 \rho_0(E_F)$. Note that $n_0 = 1$ at the symmetric limit $\varepsilon_0 = -U/2$. Let us also remark the presence of a plateau in the vicinity of the symmetric limit in the weak coupling regime $\Gamma/U \leq 0.25$ resulting from the formation of the Kondo resonance at the Fermi level; (b) The same quantity as a function of renormalized energy $-\varepsilon_0^*/\Gamma = -\varepsilon_0/\Gamma - 1/\pi \ln(\alpha U/\Gamma)$ (with $\alpha = \pi e/4$) at different values of Γ/U. Note the existence of a universal behavior in the asymmetric regime when $\Gamma/U \leq 0.25$. 55

2.11 Fit of the experimental data on the gate voltage dependence of the phase shift with the theoretical results on $\delta = \pi n_0$ as a function of $-\varepsilon_0^*/\Gamma$. Making use of the electron-hole symmetry, the experimental results obtained above the symmetric limit are reported in the same scale as those obtained below it. They are represented by triangles pointing down and up respectively in the unitary limit, and by squares and circles respectively in the weak-coupling regime. The values are extracted from ref.[35] adding a shift in the δ-scale equal to 0.29π and 0.01π in the unitary limit and weak-coupling regimes respectively. The best fit is obtained for $\Gamma/U = 0.5$ in the unitary limit both below and above the symmetric limit, and for $\Gamma/U = 0.07$ or 0.05 in the weak-coupling regime depending whether the experimental results below or above the symmetric limit respectively are considered. 56

2.12 Phase shift as a function of the gate voltage V_G. (a) unitary limit. Theoretical results from Bethe ansatz calculations at $\Gamma/U = 0.5$ (blue line) compared to the experimental data for $\Phi/\pi = \delta_{exp}/\pi + 0.29$ represented by triangles pointing up and down successively; (b) weak-coupling regime. Theoretical results from Bethe ansatz calculations at $\Gamma/U = 0.07$ and 0.04 (red and green lines respectively) compared to the experimental data for $\Phi/\pi = \delta_{exp}/\pi + 0.01$ represented by circles and squares successively. . . . 57

3.1 Phase diagram of the Anderson model as a function of $\pi\Gamma/U$ and $\epsilon_F - \epsilon_0/U$ in the Hartree-Fock approximation (Ref.[6]). 66

3.2 The $2D$ plot of the ring current (transparency) as a function of the magnetic field θ and the gate voltage V_G when the quantum dot is in the unitary limit regime. 68

3.3 The $2D$ plot of the ring current (transparency) as a function of the magnetic field θ and the gate voltage V_G when the quantum dot is in the Kondo correlation regime. 69

3.4 The $2D$ plot of the ring transparency as a function of $\theta = 2\pi\Phi/\Phi_0$ and $\delta = \pi n_0(V_G)$ at different values of t_{ref}: 1.0, 0.7 and 0.3. The points where $T_{AB} = 0.2$ are indicated by a dashed line. 70

3.5 Phase diagram of the Anderson model for $U = 1.5$ meV and $\Gamma/U = 0.05$. 72

3.6 Experimentally measured conductance of the quantum dot at $T = 150$ mK (orange squares, [62]) compared to the low-temperature Fermi-liquid prediction (blue triangles) as a function of V_G. 73

3.7 Experimentally measured conductance of the quantum dot [62] compared to the high-temperature results given by Eq.3.8, as a function of V_G at $T = 750$ mK (above) and $T = 1000$ mK (below). The experimental data are represented by red circles (at 750 mK) and green triangles (at 1000 mK). In both cfigures the theoretical points are represented by blue triangles. 74

3.8 The $2D$ plot of the ring current (transparency) as a function of the magnetic field θ and the gate voltage V_G when the quantum dot is in the Coulomb blockade regime. 76

4.1 The two-reservoir Anderson model. The localized doubly degenerated discrete interacting level is coupled via tunnel barriers to two reservoirs of free electrons (Fermi seas). In general, the reservoirs can have different chemical potentials, $\mu_L - \mu_R = eV_{SD}$, that corresponds to the source-drain (bias) voltage. In the case then $V_{SD} = 0$ this model is equivalent to the standard equilibrium one-reservoir Anderson model. 82

4.2 All the diagrams of order $|V|^6$ contributing to the $R_0(\omega)$. Solid, dashed and wavy lines represent conduction electron propagator, zero-order $R_{1,m}(\omega)$ and $R_0(\omega)$ correspondingly. 87

4.3 The leading order diagrams for $R_{1,m}(\omega)$ in a $1/N$ expansion. The double wavy line represents the "dressed" $R_0(\omega)$ propagator. 88

4.4 A schematic representation of the complete sum of diagrams for $\Sigma_{1,m}(\omega)$ self-energy, where $\Lambda_{k,m}$ take into account all the vertices. 89

4.5 Diagrammatic expansion for (a) the slave-boson and (b) the fermion propagators. Wavy, dashed and solid lines correspond to the boson, fermion and lead electrons propagators respectively. The coupling between site and leads is treated as perturbation, so each vertex corresponds to a tunneling event. 91

4.6 Keldysh contour C where $t < t'' < t'$ but $t_c < t'_c < t''_c$. 93

4.7 The four Green functions depending whether the time variables t and t' are on the positive or negative branches of the contour C 94

4.8 Diagrammatic representation of the coupled integral equations for summing diagrams with noncrossing lines (NCA integral equations). Double lines represent dressed propagators. These integral equations include all contributions $O(1)$ and $O(1/N)$ in the large-N expansion. 100

4.9 (a) A diagrammatic representation of the physical two-particle correlation function within the NCA. (b) The neglected vertex corrections are of order $O\big[(1/N)^2\big]$. 101

4.10 Energy dependence of the density of states, $\rho_\sigma(\omega)$ at equilibrium. Draw at $T = 0.005\,\Gamma$, $\mu_L = \mu_R = 2\,\Gamma$, $W = 100\,\Gamma$, the number of points used is $N = 2^{22}$. The total occupation number is found to be close to the exact value. 110

4.11 Temperature dependence of the equilibrium density of states. To calculate these curves we used: $W = 60\,\Gamma$, $\mu_L = \mu_R = 2\,\Gamma$, $N = 2^{20}$. 111

4.12 Temperature dependence of the non-equilibrium density of states at $eV_{SD} = 0.4\,\Gamma$ (for $W = 60\,\Gamma$, $\mu_L = 2.0\,\Gamma$, $\mu_R = 2.2\,\Gamma$ and $N = 2^{20}$). 112

4.13 Temperature dependence of the non-equilibrium density of states at $eV_{SD} = 1\,\Gamma$ (for $W = 60\,\Gamma$, $\mu_L = 2\,\Gamma$, $\mu_R = 3\,\Gamma$ and $N = 2^{20}$). 112

4.14 Sketch of an Aharonov-Bohm interferometer ring. The electron from the source (μ_L) can reach the drain (μ_R) through either the upper (reference) or lower arm which the quantum dot is embedded in. 114

4.15 Limit cases: (a) equilibrium regime $\mu_L - \mu_R \ll \Gamma$ at relatively high temperatures; (b) and (c) asymptotic behavior: $\mu_L - \mu_R \sim \Gamma$ with $|\mu_{L,R}| \gg \Gamma$; (d) $\mu_L - \mu_R \sim \Gamma$ and $|\mu_{L,R}| \sim \Gamma$, (e) $\mu_L - \mu_R \gg \Gamma$ 119

4.16 The occupation number as a function of the mean chemical potential in the leads $(\mu_L + \mu_R)/2$ measured from the position ϵ_0 of the localized level (in units of Γ) at $T = 0.005\Gamma$ and different voltage $eV_{SD} = \mu_L - \mu_R$ (including the equilibrium situation $\mu_L = \mu_R$). 120

4.17 (Left) the occupation number as a function of the mean chemical potential in the leads $(\mu_L + \mu_R)/2$ measured from the position ϵ_0 of the localized level (in units of Γ) for $eV_{SD} = \Gamma$ at different temperatures. Note that the temperature affects the result in a significant way when $T > 0.5\Gamma$. . . 121

4.18 (Right) the occupation number as a function of the mean chemical potential in the leads $(\mu_L + \mu_R)/2$ measured from the position ϵ_0 of the localized level (in units of Γ) for $eV_{SD} = 5\Gamma$ at different temperatures. Note the onset of a plateau around $(\mu_L + \mu_R)/2 - \epsilon_0 = 0$. As before, the temperature affects the result in a significant way when $T > 0.5\Gamma$. The plateau disappears when $T > \Gamma$. 121

4.19 Real and imaginary parts of the retarded Green function as a function of $\omega - \epsilon_0$ for $\mu = 2\Gamma$ and $T = 0.8\Gamma$. The point $\omega - \epsilon_0 = \mu$ is indicated by an arrow. 122

4.20 Phase shift Δ as a function of $\mu - \epsilon_0$ at different temperatures for $eV_{SD} = 10^{-5}\Gamma$ (equilibrium regime). For comparison πn_0 as a function of $\mu - \epsilon_0$ at $T = 0$ is also reported – black line (result obtained in Ref.[65]). Let us remaind that πn_0 coincide with Δ at $T = 0$. 123

4.21 The phase $\arg G^r_{d\sigma}(\omega)$ of the retarded localized electron Green function as a function of $(\omega - \epsilon_0)$ both (i) at equilibrium at $\mu = \mu_1$ and $\mu = \mu_2$ for $T = 0.05\Gamma$, and (ii) out-of-equilibrium at $T = 0.8\Gamma$ and $T = 0.05\Gamma$ for $\mu_L = \mu_1$ and $\mu_R = \mu_2$. (Left) result for the values $\mu_1 = 2\Gamma$ and $\mu_2 = 3\Gamma$. (Right) results for the values $\mu_1 = 5\Gamma$ and $\mu_2 = 6\Gamma$. The position of $(\mu_1 - \epsilon_0)$ and $(\mu_2 - \epsilon_0)$ respectively is indicated by an arrow. Note that $\arg G^r_{d\sigma}(\omega)$ depends strongly with ω when $(\mu_1 - \epsilon_0)$, $(\mu_2 - \epsilon_0)$ is small (left) whereas its energy dependence is negligible when $(\mu_1 - \epsilon_0)$, $(\mu_2 - \epsilon_0)$ is large (right). 124
4.22 Phase shift Δ as a function of $\mu - \epsilon_0$ at different temperatures for $eV_{SD} = \Gamma$ (out of equilibrium). 126
4.23 Phase shift Δ as a function of $\mu - \epsilon_0$ at different temperatures for $eV_{SD} = 2\Gamma$ (out of equilibrium). 126
4.24 Phase shift Δ as a function of $\mu - \epsilon_0$ at different temperatures for $eV_{SD} = 4\Gamma$ (out of equilibrium). Note the presence of a shoulder structure in the evolution which disappears when $T > 0.9\Gamma$. 127
4.25 Phase shift Δ as a function of $\mu - \epsilon_0$ at different values of the bias voltage eV_{SD} (the temperature considered in each case varies but is always low). Note that the evolution exhibits a shoulder-structure when V_{SD} becomes large. 128
4.26 Phase sift Δ as a function of $\mu - \epsilon_0$ at different values of the bias voltage $\mu_L - \mu_R$ for $T = 0.05\Gamma$ (low temperature regime). 129

Bibliography

[1] W. B. Pearson. *Phil. Mag.*, 46:911, 1955.

[2] T. Kasuya. *Prog. Theor. Phys.*, 16:58, 1956.

[3] K. Yosida. *Phys. Rev.*, 107:396, 1957.

[4] J. Kondo. *Prog. Theor. Phys.*, 32:37, 1964.

[5] A.C. Hewson. *The Kondo problem to Heavy Fermions*. Cambridge University Press, Cambridge, England, 1993.

[6] P. W. Anderson. *Phys. Rev.*, 124:41, 1961.

[7] A.A. Abrikosov. *Physics*, 2:5, 1965.

[8] A.A. Abrikosov. *Fundamentals of the theory of metals*. Elsevier Science Publishers, 1988.

[9] P. W. Anderson. *Phys. Rev.*, 164:352, 1967.

[10] P. W. Anderson. *J. Phys. C*, 3:2439, 1970.

[11] K. G. Wilson. Collective properties of physical systems. *Nobel Symposia 1973*, page 68, 1974.

[12] K. G. Wilson. *Rev. Mod. Phys.*, 47:773, 1975.

[13] P. Nozières. *J. Low Temp. Phys.*, 17:31, 1974.

[14] N. Andrei. *Phys. Rev. Lett*, 45, 1980.

[15] N. Andrei et al. *Rev. Mod. Phys.*, 55:331, 1983.

[16] A. M. Tsvelick. *Sov. Phys. JETP Lett.*, 31:392, 1980.

[17] A.M. Tsvelick and P.B. Wiegmann. *Advances in Physics*, 32:453, 1983.

[18] R. Landauer. *IBM J. Res. Dev.*, 1:223, 1957.

[19] R. Landauer. *IBM J. Res. Dev.*, 32:306, 1988.

[20] R. Landauer. *Physica Scripta*, T42:110, 1992.

[21] A. Yacoby et al. *Phys. Rev. Lett.*, 74:4047, 1995.

[22] R. Schuster et al. *Nature*, 385:417, 1997.

[23] M.A. Kastner. *Phys. Today*, 46(1):24, 1993.

[24] Ashori R. C. *Nature*, 379:413, 1996.

[25] L. Kouwenhoven and L. Glazman. *Phys. World*, 14:33, 2001.

[26] Harmas C. J. P. M. *Phys. World*, 5:50, 1992.

[27] L.P. Kouwenhoven et al. *Reports on Progress in Physics*, 64:701, 2001.

[28] Kouwenhoven L.P. and Marcus C. M. *Phys. World*, 11, 1998.

[29] D. Goldhaber-Gordon et al. *Phys. Rev. Lett.*, 81:5225, 1998.

[30] U. Meirav. Phd thesis, M.I.T, 1990.

[31] M. Pustilnik and L.I. Glazman. *J. Phys.: Condens. Matter*, 16:R513, 2004.

[32] W.G. Van der Wiel et al. *Science*, 289:2105, 2000.

[33] M. Büttiker. *Phys. Rev. Lett.*, 57:1761, 1986.

[34] G. Breit and E. Wigner. *Phys. Rev.*, 49:519, 1936.

[35] Y. Ji et al. *Phys. Rev. Lett.*, 88:076601, 2002.

[36] Y. Ji et al. *Science*, 290:779, 2000.

[37] D.C. Langreth. *Phys. Rev.*, 150:516, 1966.

[38] U. Gerland et al. *Phys. Rev. Lett.*, 84:3710, 2000.

[39] A.L. Yeyati and M. Büttiker. *Phys. Rev. B*, 52:R14360, 1995.

[40] H.-W. Lee. *Phys. Rev. Lett*, 82:2358, 1999.

[41] T. Taniguchi and M. Büttiker. *Phys. Rev. B*, 60:13814, 1999.

[42] G. Hackenbroich and H.A. Weidenmüller. *Europhys. Lett.*, 38:129, 1997.

[43] H.Q. Xu and W. Sheng. *Phys. Rev. B*, 57:11903, 1998.

[44] P.S. Deo. *Physica E*, 1:301, 1997.

[45] C.-M. Ryu and S. Cho. *Phys. Rev. B*, 58:3572, 1998.

[46] Q. Sun and T. Lin. *Eur. Phys. J. B*, 5:913, 1998.

[47] S.M. Cronenwett et al. *Science*, 281:540, 1998.

[48] P. Nozières. *J. Low Temp. Phys.*, 17:31, 1974.

[49] L.I. Glazman and M.É. Raĭkh. *JETP Lett.*, 47:452, 1988.

[50] T.K. Ng and P.A. Lee. *Phys. Rev. Lett.*, 61:1768, 1988.

[51] N. Levinson. *Kgl. Danske Videnskab. Selskab, Mat-Fys. Medd.*, 25:9, 1949.

[52] L.I. Schiff. *Quantum Mechanics, McGraw-Hill, New York*, 1968.

[53] P. Swan. *Proc. R. Soc. London Ser. A*, 28:10, 1955.

[54] L. Rosenberg and L. Spruch. *Phys. Rev. A*, 54:4978, 1996.

[55] L. Rosenberg and L. Spruch. *Phys. Rev. A*, 54:4985, 1996.

[56] J. Konig at al. *Phys. Rev. Lett.*, 87:156803, 2001.

[57] N. Kawakami and A. Okiji. *J. Phys. Soc. Jpn.*, 51:2043, 1982.

[58] N. Kawakami and A. Okiji. *J. Phys. Soc. Jpn.*, 51:1145, 1982.

[59] F.D.M. Haldane. *Phys. Rev. Lett.*, 40:416, 1978.

[60] G. Hackenbroich. *Phys. Reports*, 343:463, 2001.

[61] T.A. Costi et al. *J. Phys.: Condens. Matter*, 6:2519, 1994.

[62] M. Heiblum. *talk at conference ITP*, 10/03/01.

[63] D.R. Hamann. *Phys. Rev.*, 158:570, 1967.

[64] Y. Meir et al. *Phys. Rev. Lett.*, 70:2601, 1993.

[65] Y. Meir N.S. Wingreen. *Phys. Rev. B*, 49:11040, 1994.

[66] R. Konik et al. *Phys. Rev. B*, 66:125304, 2002.

[67] N.S. Wingreen Y. Meir. *Phys. Rev. Lett.*, 68:2512, 1992.

[68] A.-P. Jaudo et al. *Phys. Rev. B*, 50:5528, 1994.

[69] S. Datta. *Electronic Transport in Mesoscopic Systems*. Oxford Univercity Press, Oxford, 1995.

[70] L.V. Keldysh. *Soviet Phys. JETP*, 20:1018, 1965.

[71] C. Caroli et al. *J. Phys. C*, 4:916, 1971.

[72] N.E. Bickers. *Rev. Mod. Phys.*, 59:845, 1987.

[73] N.E. Bickers et al. *Rev. Rev. B*, 36:2036, 1987.

[74] A. E. Ruckenstein D. L. Cox. *Phys. Rev. Lett.*, 71:1613, 1993.

[75] T.A. Costi et al. *Phys. Rev. B*, 53:1850, 1996.

[76] D.L. Cox. *Phys. Rev. B*, 35:4561, 1987.

[77] S. Barnes. *J. Phys. F*, 29:3035, 1984.

[78] S. Barnes. *J. Phys. F*, 35:5072, 1987.

[79] Piers Coleman. *Phys. Rev. B*, 29:3035, 1984.

[80] G.D. Mahan. *Many-particle Physics*. Kluwer Academic/Plenum Publishers, New York, 2000.